LARGE-EDDY SIMULATION STUDY OF TURBULENT FLOW OVER DUNE FIELD

by

Chao Wang

APPROVED BY SUPERVISORY COMMITTEE:

____

William Anderson, Chair

____

Stefano Leonardi

____

Xianming Dai

____

Zhenpeng Qin

This dissertation

is dedicated to my wife Dandan

and my parents.

LARGE-EDDY SIMULATION STUDY OF TURBULENT FLOW OVER DUNE FIELD

by

CHAO WANG, BS, MS

DISSERTATION

Presented to the Faculty of

The University of Texas at Dallas

in Partial Fulfillment

of the Requirements

for the Degree of

DOCTOR OF PHILOSOPHY IN

MECHANICAL ENGINEERING

THE UNIVERSITY OF TEXAS AT DALLAS

December 2019

ACKNOWLEDGMENTS

In the very beginning, I would like to express my gratitude to my supervisor, Dr. William Anderson, for his guidance and support on my doctoral research work. I am also very thankful to Dr. Stefano Leonardi for being such a wonderful teacher who inspired me through his classes to make me go further in turbulent flow research. I am deeply grateful to Dr. Xianming (Simon) Dai who provided me insightful suggestions for my doctoral project and future career development. And I also thank Dr. Zhenpeng Qin who gives me comprehensive advice and comments leading to a much-improved doctoral dissertation. Their meaningful and valuable suggestions helped me to finish my doctoral project smoothly.

Here, I also want to express my gratitude to Dr. G. Valerio Iungo who inspired me with experimental and statistical research on boundary layer meteorology and Dr. Robert Stern in the Department of Geosciences who invited me to join their AGU supported field trip to Monahans Sandhills State Park for dune study. I also would like to convey my thanks to my doctoral project collaborators: Dr. Kenneth Christensen, Dr. Gianluca Blois and Dr. Nathaniel Bristow in the University of Notre Dame. They have generously shared valuable experimental results with us. I also acknowledge the present and previous research members of the Aeolus Research Group for the generous help.

I want to give my most heartfelt thanks to my family and friends, for their continuous and unquestioning support and love during my study at UT Dallas. God created the universe. May all the discoveries and inventions be filled with the glory of him.

October 2019

LARGE-EDDY SIMULATION STUDY OF TURBULENT FLOW OVER DUNE FIELD

Chao Wang, PhD
The University of Texas at Dallas, 2019

Supervising Professor: William Anderson, Chair

The interactive feedback between turbulent flow and dune morphology is significant to understand the formation of dune field and turbulent flow physical attributes. Different kinds of deductions and formulas are proposed via sorts of field measurements and experimental observations, some of which indeed could provide highly precise predictions to sediment transportation and dune morphodynamics. However, it becomes harder to forecast them when the sediment particles suspended by critically high Reynolds number wind regime, given the unsteady turbulent mixing process and wide range of turbulent length scales. In terms of that, the aero/hydro-dynamical effect on dune morphodynamics has been widely studied by analyzing aeolian process, where turbulent coherent structures induced local wind shear enhancement gets revealed by experimental observations and numerical simulations. Several significant characteristics of turbulent flow over dune field such as the dominance of large length scale of turbulent eddies and inertial effect make Large-Eddy Simulation (LES) become a very promising study methodology. In this work, the solid-fluid mutual effects in dune field has been comprehensively demonstrated via LES method associated with Particle Image Velocimetry (PIV) data validation. To approach the universality and veracity, idealized and realistic dune field have been both studied in this work. The idealized barchan dune field consists of four different stages with decreasing streamwise offset but same spanwise offset, aimed to reveal aeolian effects in dune field morphological complexity – offset merger

interaction. White Sands National Monument (WSNM) is located at the Tularosa Basin in southern New Mexico, which has been adopted as the ideally realistic case. The simulations in different mesh density are displayed at the end to show the grid insensitivity of this work.

The high credibility of LES results has been verified by the PIV results in Appendix A. Through LES, the interactive motion induced downwind dune asymmetric erosion gets well elaborated associated with a coherent structure – interdune roller, where differential helicity calculation reveals its positive streamwise rotation, scouring the sediment on the interdune surface of downwind dune. The decreasing interdune spacing effectively enhances the local momentum flux – flow channeling, which impinges on the stoss face of downwind dune and elevates the surface shear magnitude. The wake centerline misalignment – wake veering – has been observed in LES and PIV results. Isosurfaces of conditionally-averaged and instantaneous Q criterion complementarily reveal the hairpin vortex shedding from the dune brinkline and the streamwise distance of vortex core, which is revealed to be proportional to dune crest height, associated with the constant shedding frequency $St = 0.25$ after the practice of wavelet analysis. The Reynolds-averaged streamwise vorticity transport equation explain the interdune roller is a consequence of vortex stretching and flow channeling. Meanwhile, through the Reynolds-averaged data initiated simulation, the genesis of turbulent coherent structure has been fully understood, that is generated from streamwise vortex roller (interdune roller) in interdune region and spanwise vortex roller surrounding the brinkline. With wide range of turbulent spectrum involved, the spanwise vortex roller breaks down into aggregations of small rollers which get stretched and tilted into successive hairpin vortices shedding off from dune brinklines along wake centerlines. While, the streamwise vortex roller also support the hairpin evolving processes in small dune leeward within interdune region. The WSNM results favorably testify this turbulence structural model in DFSL as well. Finally, the integral length scale is calculated on different elevations in all

cases. The integral length profiles of ideal and realistic case indicate self-similar heterogeneity attribute of turbulent eddies in dune-field boundary layer. The scaling practice of spatial integral length concludes the mixing-layer analogy of the dune-field obstructed shear flow in roughness sublayer and the effectivity of attached-eddy hypothesis at higher located turbulent structures overlaying roughness sublayer.

TABLE OF CONTENTS

LIST OF FIGURES

LIST OF TABLES

CHAPTER 1

INTRODUCTION

1.1 Dune-Field Morphodynamics

Dune field is a ubiquitous landform in deserts on different planets such as Mars, Venus, Titan and Earth (Bagnold, 1956; Shao, 2008; Kok et al., 2012; Parteli et al., 2006; Pelletier, 2009; Herrmann et al., 2005; Best et al., 2001; Palmer et al., 2012b; Melton, 1940; Parteli et al., 2009; Zhang et al., 2012). Figure 1.1 displays a series of realistic dune fields on Titan (a), Earth (b), and Venus (c), respectively, in different dune configurations. Panel (a) shows linear dune field on Titan, wherein elongated dune ridges (white dashed line) get stretched by upcoming bidirectional wind (red quivers) and these dense packages of ridges migrate along the composite wind directions like "fingerprints" of local meteorological monsoon; Panel (b), transversal dunes with barchanoid ridges compose the displayed dune field on Earth. Like Panel (a), wind direction is denoted in red quiver, but in unidirectional fashion (white dashed line highlights ridges-crossing and coalition, seems more flexuous than linear dune ridges); Panel (c) shows Martian barchan dune field. Wind loading redistributes sediment resources into multiple groups of successive barchan dunes in aligned lines (white dotted line). Evident stretched morphologies and proximal collision can be captured in picture, which will be discussed in the following chapter. Accordingly, the ubiquitous existence and multiformity of dune field are well exhibited here. Moreover, behind such complex bedform patterns, the mutual influences between sediment erosion and aerodynamic forcing complicate, profoundly, the understandings of morphodynamics and turbulent boundary layer over dune fields.

The dune formation is an interactive process between the aloft atmospheric flow, sediment and dune morphology (Shao, 2008). The nonlinear relation between these major factors could arouse different dune types or complex intercrossing in same type of dune. Usually, dune can be classified based on the body shape and the number of the slip faces (Shao, 2008; Bagnold, 1956). Basically, sand dune can be classified as barchan dunes, transverse (transversal) dunes, star dunes, reversing dunes, longitudinal dunes and so forth. These dune types cannot merely indicate forcing flow direction, but also reflect local sediment availability and stability. For example, star dune is named by its special landform feature which is composed by multiple elongated horns with more than two slip faces and looks like a star, formed by large amount of sediments under multiple directional upcoming wind (Kocurek and Ewing, 2005; Kocurek et al., 2007). Linear dunes, seem like multiple elongated sand waves, are generated by bi-directional winds (Bagnold, 1956; Tsoar, 1983; Livingstone et al., 2006; Lancaster, 1989a). Barchan dune consists of two faces (see Figure 1.2). Two elongated limbs are called "horns", which is stretched by the unidirectional upcoming wind. Even under the same atmospheric condition and with sediment availability, vegetation density and soil moisture can form sediments into parabolic dunes via low sediment movability under highly stable conditions. In this work, we adopted a series of barchan dune groups in various sets of configurations as the idealized cases, given its unidirectional turbulent flow regime and highly universality in nature. Figure 1.2 is a sketch of an idealized "building block" barchan, showing the crest height, h, and spatial extent in the streamwise, λ, and spanwise, w, directions. The spatial extents – λ and w – change for different conditions although, in general, $w/\lambda \approx 1$ (Palmer et al., 2012a). Figure 1.2 also includes a symmetric plane transect (orange), showing the characteristically gentle streamwise height gradient on the windward (stoss) face, $\theta \approx 15°$, followed by a steeply-declining profile on the leeward side, $\theta \approx 33°$ (Livingstone et al., 2006); it is further emphasized that the windward side barchan profile exhibits a concave-convex-concave form, which is not captured in Figure 1.2 (Livingstone et al., 2006). Isolated natural barchans resembling the Figure 1.2 sketch require limited sediment and minimally varying flow direction (Hersen et al., 2004). In nature, the former and latter conditions are common and uncommon, respectively, especially in aeolian systems where seasonal climate variability changes directions of sediment mobilization.

Figure 1.1. Realistic dune fields on Titan (a), Earth (b) and Venus (c) have been shown here in different dune types (picture resource is from NASA). Panel (a) is linear dune field on Titan, wherein the wind directions are noted as red quivers and its corresponding dune features have been marked out in white dashed line. Panel (b) is transverse (transversal) dune field on Earth. The transversal dune field is formed by a unidirectional wind, which noted via red quiver. Its corresponded dune feature is captured by white dashed lines. Panel (c) shows barchan dune on Mars, which is a very ubiquitous dune type on planets. The unidirectional upcoming wind (red quiver) forms several linear groups (white dotted line) of successive barchan dunes from the upflow sediment resources.

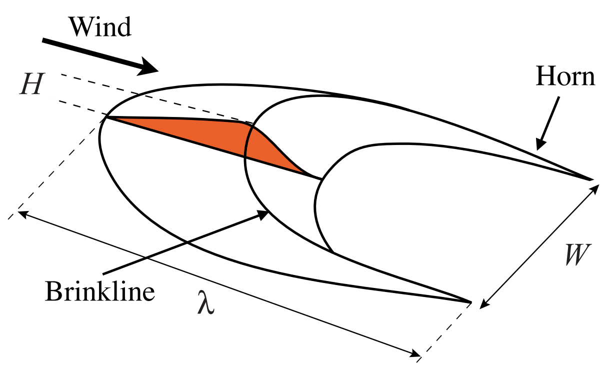

Figure 1.2. The idealized barchan dune which is in a symmetric crescentic feature. The dune crest height is denoted by H. Dune streamwise extent is denoted by λ, while spanwise extent is denoted by W. The windward face is called "stoss" side, while the backward face is called "lee" side.

With global warming becoming more serious during these years, desertification is propagating world-widely, devouring thousands of

As aforementioned paragraph indicates, aeolian process, sediment availability and amount could comprehensively impact dune morphodynamics. However, sediment availability and amount are comparatively stable during a very long period, which makes aeolian process become a crucial factor in dune morphodynamics. Since aeolian process is a significant trigger in dune formation, the occurrence and shape of dunes can be potential indicators of the local wind regimes and also can provide the indirect sediment information (Bagnold, 1956; Shao, 2008; Kok et al., 2012; Parteli et al., 2006). Under the effect of fully developed turbulent flow, dune morphodynamics become transient and hard to predict, considering the agitated turbulent fluctuation close to the ground and nonlinear characteristics between sediment saltation and surface stress (Bagnold, 1956; Parteli et al., 2006; Bristow et al., 2017; Wang et al., 2017, 2016; Wang and Anderson, 2018b, 2019a). Moreover, the interactive collision between solitary dunes will generate more complexity for dune morphodynamics. To demonstrate the regularity of interactive collision in realistic dune fields, Figure 1.3 is presented here. Figures 1.3(a) and 1.3(b) display the terrestrial aeolian dune fields, while Figure 1.3(c) is an aeolian dune field within Gale crater, Mars. In Figures 1.3(a) and 1.3(b), the crescentic barchan dunes are asymmetric, where the brinklines are intermingled through interaction processes (Kocurek and Ewing, 2005; Kocurek et al., 2007). Figure 1.3(a) is from the Namib Desert, Namibia (Lancaster, 1982, 1989b), while Figure 1.3(b) is from the White Sands National Monument (WSNM), New Mexico USA (Ewing and Kocurek, 2010a,b; Jerolmack and Mohrig, 2005; Anderson and Chamecki, 2014; Wang and Anderson, 2019a) (image recorded via kite-mounted camera by Ralph Lorenz). The White Sands dunes are composed of gypsum crystals and are subjected to three prominent winds, which induce the spatial complexity evident in the image (see Figure 2.2). In this work, we have adopted WSNM as the realistic case and will covered details of the dune characteristics in Chapter 2. Finally,

Figure 1.3(c) is from the Bagnold Dune Field, Gale crater, Mars. The Bagnold dunes are composed of hematite grains, giving them their dark complexion (Grotzinger et al., 2014). Dunes within this field change in response to underlying topographic variability within the crater (Hayward et al., 2007). In addition to Earth and Mars, complex aeolian dune fields are also found on Venus and Titan (Bourke et al., 2010). For discussion, different color annotations are used in Figure 1.3 for a few interactions at initial (blue) and advanced (red) stages, to highlight the spatial complexity of interacting dune fields. In this work, numerical simulation datasets at realistic inertial conditions are used to demonstrate an underlying similarity in the mechanism responsible for the emergence of dune interactions and understand the dune-field roughness sublayer in boundary layer meteorology through studying flow patterns and spatial distributions of shear velocity on the dunes, all of which indicate how aerodynamic sheltering and minimal spatial gradients of height across interactions serve to minimize sediment mass flux at interactions. Here, we must note the buoyancy effects due to wall-normal heat gradient and the sediments propagation in wind flux will also impact the morphodynamic, but for the interests of results comparison and deduction, we consider neutral atmospheric conditions and no sediments particle mixture in simulation.

To understand and predict dune morphodynamics, lots of studies and observations have been done through numerical methods (Parteli et al., 2006; Pelletier, 2009; Parteli et al., 2009; Zhang et al., 2012, 2010; Narteau et al., 2009; Khosronejad and Sotiropoulos, 2017; Wang et al., 2016, 2017; Wang and Anderson, 2018a,b, 2017, 2019a,b) and experimental methods (Bagnold, 1956; Shao, 2008; Herrmann et al., 2005; Endo et al., 2004; Best et al., 2001; Palmer et al., 2012b; Melton, 1940; Bristow et al., 2018; Müller and Gyr, 1986; Alvarez and Franklin, 2019; Bristow et al., 2018). Figure 1.4 demonstrates a series of stages contributing to an offset interactive collision, which is the results from the mobile-bed flume experiments in Hersen and Douady (2005). From Panels (a) to (e), the small upflow dune approaches the large downflow dune from a slightly spanwise-staggered position. And although both dunes

Figure 1.3. (Color) Images of complex aeolian dune fields on Earth and Mars: (a) Skeleton Coast, Namib Desert, Namibia (photograph: Michael Poliza ©, National Geographic Creative); (b) White Sands National Monument, New Mexico, USA (photograph: Ralph Lorenz, Johns Hopkins University Applied Physics Lab); and (c) Bagnold Dune field within Gale crater, Mars (Image source: Bourke et al., 2010 (Bourke et al., 2010), and generated via High Resolution Imaging Science Experiment (HiRISE) image reconstruction to three-dimensional digital elevation map; (Bourke et al., 2010; Zimbelman, 2010)). On images, red and blue lines denote interactions at advanced and initial stages, respectively.

are migrating, the small dune migrates faster owing to its comparatively smaller size (the migration speed is inversely proportional to the height (Kocurek and Ewing, 2005)). Though smaller, it is apparent that its morphology is largely preserved during the interaction. The downflow dune, on the other hand, undergoes significant morphodynamic transformation. In the wake of the small dune, the horn of the large dune (recall Figure 1.2 and accompanying text) exhibits great streamwise elongation. This pattern becomes more pronounced as the small dune approaches, inducing geometric asymmetry in the large dune. And although not shown here, completion of the cycle results in simultaneous downflow ejection of a small dune (illustrated by red arrow on Figure 1.4). Recently, Alvarez and Franklin (2018); Andreotti et al. (2002) executed experimental investigation on the sand pile movement to reveal the barchan dune formation. Particularly Alvarez and Franklin (2018) adopted colored beads as sediment for the record of sediment movements, demonstrating the horn formation under water flow that is the relatively high sediment erosion at margin of sand pile. However, the asymmetric migration pattern of downwind dune is still not discussed. Give the limitations such as small length scale morphology and low Reynolds number flow regime in the aquicolocus dune morphodynamic experiments, which could dilute the deductions for terrestrial dune formation, lots of numerical morphodynamic prediction schemes have been proposed recently (Narteau et al., 2009; Khosronejad and Sotiropoulos, 2017; Sauermann et al., 2003; Parteli et al., 2014; Durán et al., 2010). Narteau et al. (2009) simulated dune field morphodynamics through cellular automaton, where different types of sediment are defined based on the local aerodynamical condition (local friction velocity $u_*(\boldsymbol{x}, t)$). But given the deficiency of surrounding turbulent flow simulation, dune field interactive collision has not been fully discussed. Durán et al. (2010) has executed very promising solitary barchan dune formation and migration pattern based on well-known dune continuous model (Nishimori and Ouchi, 1993). However, the turbulent effects are overlooked and the interactive dune morphodynamics cannot capture the realistic dune field characteristics which is asymmetric erosion of downwind dune at interdune region. The work of Khosronejad and Sotiropoulos (2017) indeed broadened the view of dune morphodynamics and improved the numerical dune morphology prediction with turbulence. They have not merely considered the atmospheric turbulence effect on dune formation by using Large-Eddy Simulation (LES), but taken extremely dense terrain-followed mesh system through the Finite Element Method (FEM) to generate a series of realistic simulation results. But the turbulent coherent structures with in dune-field roughness sublayer has not been discussed. These studies have contributed to provide reliable morphodynamics prediction model for complex dune field. But in order to approach that point, the asymmetric erosion pattern and the crucial influence implemented by aloft turbulent boundary layer coherent structures should be elaborated.

1.2 Dune-Field Turbulent Coherence

Interactive effects between dune morphology and turbulent flow make predicting dune morphodynamics much tougher, considering the uncertainty and complexity of turbulent flow in dune field roughness sublayer (Anderson and Chamecki, 2014; Wang and Anderson, 2019a,b).

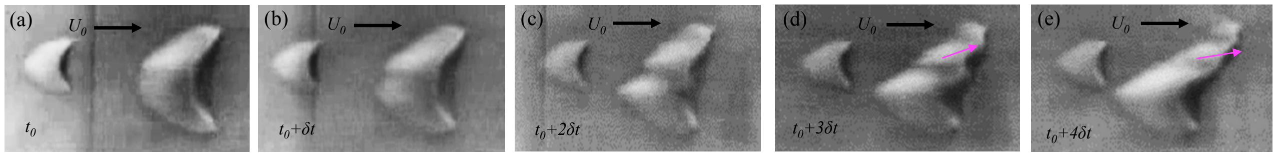

Figure 1.4. Photographs of offset merger interaction stages (Kocurek and Ewing, 2005), observed in mobile-bed flume experiments (images retrieved from Hersen and Douady (2005)). Annotations of prevailing mean flow direction and representative times added for illustration; red arrows illustrate downflow trajectory of ejected dune.

But how upcoming turbulent flow is able to control dune morphodynamics? In fact, turbulent flow can leverage aeolian erosion through various ways such as dune morphology triggered secondary flow and different length scale turbulent coherence. Various studies have been done to understand the relation between turbulent coherence and morphodynamics, some of which are focusing on sediment saltation based on local dune morphological conversion under turbulent aerodynamic loading (Khosronejad and Sotiropoulos, 2017; Pähtz et al., 2012; Kok et al., 2012; Ortiz and Smolarkiewicz, 2009; Bagnold, 1956; Shao, 2008). While turbulent coherence study associated with different dune-field arrangements have also been dictated (Palmer et al., 2012b; Omidyeganeh and Piomelli, 2011a, 2013a,b; Omidyeganeh et al., 2013; Wang and Anderson, 2018b; Bristow et al., 2017, 2019; Anderson and Chamecki, 2014; Wang et al., 2016, 2017; Wang and Anderson, 2018a,b, 2017, 2019a,b). These works ideographically provide plenty of numerical and experimental datasets for dune field analysis and indeed have helped us to achieve the full understanding of dune field. The current work will numerically simulate the flow within dune field roughness sublayer (DFSL) and, meanwhile, provide the evidences of geophysical turbulent flow in dune morphodynamics and spatial attributes within DFSL dynamics.

Sediment erosion can be classified into different types based on sediment particle diameter. Figure 1.5 shows the schematic picture of sediment erosion classification, which is from Shao (2008). Sediment erosion pattern can be classified based on sediment spatial extents

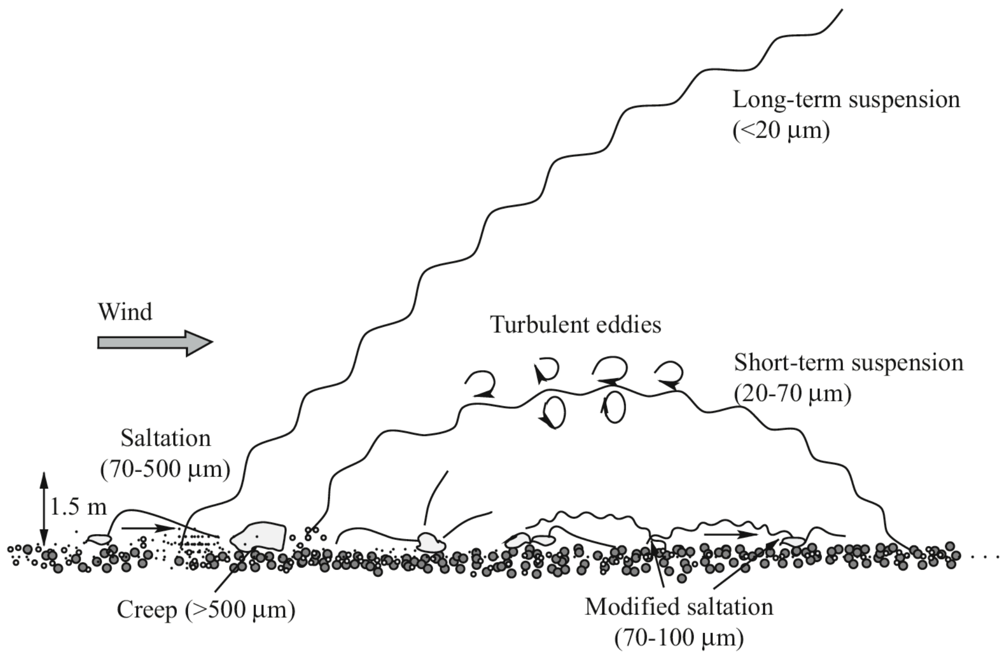

Figure 1.5. The diagrammatic drawing from Shao (2008) for sediment creep, saltation and suspension of soil particles during the erosion event. Saltation is further classified into pure and modified saltation and suspension is further classified to short-term and long-term suspension.

such as diameter, since higher wind loading will be required to lift sediment particle in large size. Thus, smallest sediments ($< 20\mu m$) will easily suspend in air for long distances, which is so-called long-term suspension (Shao, 2008). For $20-70\mu m$, less distance will be transported for suspended sediments. For sediment size ranging from $70 - 500\mu m$, sediment saltation is dominant near ground. For most sediment in quartz, diameter will be $0.0625 - 2mm$ or $62.5-2000\mu m$, thus most of sand can migrate in sediment saltation. For sediments $> 500\mu m$, upcoming wind could hardly provide force to against its gravity, instead forcing sediment grains to creep on the ground. During dune-field morphodynamics, most sediments sizes are in moderate range, $20 - 500\mu m$, which means aloft turbulent flow can easily leverage sediment saltation trajectories to control the resultant dune features (Bagnold, 1956; Shao, 2008; Kok et al., 2012). In sediment saltation progress, it is widely founded that turbulent flow plays a very extraordinarily crucial role, modifying sediment trajectories and enhancing local sediment mass transportation via different length scales turbulence structures (Jacob and Anderson, 2016; Wang and Anderson, 2018b,a, 2019b; Wang et al., 2016). Hence, it is very worthwhile efforts to dig into the dune-field aloft turbulent structures for the precise sediment morphodynamics predictions.

The turbulent flow effects on sediment saltation have already been observed more than fifty years ago from wind tunnel datasets done by Bagnold (1956). It has indicated the sediment saltation is triggered by the aerodynamic surface drag $\tau^w(\boldsymbol{x}, t)$, which is also called surface shear. Groundbreakingly, the Bagnold Scheme proposed by Bagnold (1956) (Equation 3.5) is based on experimental datasets to represent sediment particle movability under specific aeolian environment by surface threshold fiction velocity $u_{*,t}$, which makes dune morphology prediction possible. And the non-Gaussian turbulence statistics in the aloft fluid (inherent to dynamics of the roughness sublayer) ensures that the resultant hererogeneity across the dunes, *vis.* $u_* = u_*(\boldsymbol{x}, t) = (\tau^w(\boldsymbol{x}, t)/\rho)^{1/2}$ which is the surface friction velocity on the dune surfaces, where ρ is fluid density, and $u_{*,t}$ can be used as the magnitude threshold for sediment movement, that means when $u_* > u_{*,t}$ is achieved, the sediment will get shifted by aerodynamic loading (see Chapter 3 for detailed explanation). Moreover, since the sediment mass flux, $q(\boldsymbol{x}, t) \sim (\tau^w(\boldsymbol{x}, t))^n \sim (u_*(\boldsymbol{x}, t))^{2n}$, where $n \geqslant 1.5$ is commonly cited (Bagnold, 1956; Kok et al., 2012; Meyer-Peter and Müller, 1948; Shao, 2008; Fernandez-Luque and van Beek, 1976), small deviations in aloft turbulent flow from its Reynolds-averaged value can greatly impact dune field morphodynamics. Meanwhile, Kok et al. (2012) simulated saltation trajectory variations for particles with different diameters and concluded various strengths of turbulence can impact the sediment saltation at different levels. Thus, the vigorous turbulent mixing in roughness sublayer is extremely worth to be deliberated within morphodynamics.

Furthermore, turbulent coherent structures can be impacted by dune morphologic variations too. The shear layer shed from dune stoss face reinforces large momentum and sediment mass transportation associated with turbulent coherent structures in different length scales (Omidyeganeh and Piomelli, 2011a, 2013a,b; Omidyeganeh et al., 2013; Wang and Anderson, 2018b; Bristow et al., 2017; Palmer et al., 2012b). Palmer et al. (2012b) has illustrated "sheltering effect" in two interacting barchan dunes, that is the flow on the stoss side of the downstream dune is under influence of the upstream dune shear layer where turbulent structures shed from the upstream dune brinkline. Recently Wang and Anderson (2018b) recovered such turbulent coherent structures shed from upstream dune which is a train of hairpin vortices shed at normalized frequency $St = 0.25$ (see the wavelet analysis post-processing in Section **??** in Chapter 3). Also in both Palmer et al. (2012b) and Wang and Anderson (2019a), extremely high magnitude of turbulent kinetic energy is captured in the shear layer by using proper orthogonal decomposition (POD) and Reynolds-averaged datasets. Wang and Anderson (2019a) has recovered the turbulent coherent structure genesis within dune-field roughness sublayer featured as a dune-field brinkline aroused Kelvin–Helmholtz instability (more details will be discussed in Chapter 4). It is important to note the critically huge computational requirements to recover the fully developed turbulent flow associated with continuously morphodynamic dune topographies. Fortunately, the mobile-bed flume experiment result in Kocurek and Ewing (2005) indicates the "noneffective" range of two-dune streamwise distance, which can make this work in a series of discrete morphodynamic arrangements.

From Section 1.1, the barchan dune morphodynamics forms by inertial loading dominated unidirectional upcoming flow, which make Large-Eddy Simulation (LES) become a extraordinarily promising research method (see Section 2.1 in Chapter 2 for more details of LES method). The great fidelity of LES in dune field research has been validated in numerous works. Previously Omidyeganeh and Piomelli (2011a, 2013a,b); Omidyeganeh et al.

(2013) recovered coherent structures of various types in the separated shear layer due to the Kelvin–Helmholtz instability. The relation between the coherent structures and sediment saltation has been well explained through three-dimensional visualization using LES on 2D and 3D dune. Omidyeganeh and Piomelli (2011a) has recovered the turbulent ejection events in the 2D dune lee side, which is between the two counter-rotating vortex legs where upwelling and downwelling events on the ground are known as "Boils", stimulating large momentum and mass transportation near dune surface, which has also been captured in this work at Chapter 4. Omidyeganeh and Piomelli (2013b) has displayed the rollers over the lobe extending to the saddle plane associated with $Q4$, sweep, domination everywhere, which is the event responsible for the sediment transportation (Nelson et al., 1993). Omidyeganeh et al. (2013) shows the instantaneous flow distributions surrounding a solitary barchan dune in experimental spatial extent, where the 3D barchan dune geometry is from Palmer et al. (2012b), and same with the barchan model in this work. However, the fluid structures and momentum redistribution during dune interactions have not been fully discussed to understand the asymmetric erosion pattern in morphodynamics. Moreover, the concern of the realistic dune field flow properties may not obey the results deducted from idealized dune topographies. Thus, it is necessary to study the flow property coupled with realistic dune-field topographies. In this work, White Sands National Monument has been adopted as the realistic case to verify the conclusions drawn from idealistic cases. (The details of LES and cases will be discussed in Chapter 2).

1.3 Dune-Field Roughness Sublayer

Given the special dune-field roughness element characteristics, turbulent coherent structure type has been found different with other types of canopies such as buildings, trees and so forth (Leonardi et al., 2003; Finnigan et al., 2009; Bailey and Stoll, 2016; Anderson and Chamecki, 2014; Wang and Anderson, 2019a,b; Wang et al., 2016). But just like the other types of roughness elements, dune-field boundary layer should also been separated in different sublayers based on the local turbulent mixing strength and coherent structures. Anderson and Chamecki (2014) has revealed the existence of mixing-layer analogy within dune-field roughness sublayer and shown the dune-field sublayer (DFSL) laying over dune field and ranging approximately two to three times the height of dunes, where turbulence is critically under the influence of surface drag. Inertial layer overlays on the DFSL where wall-bounded shear should be captured such Attached-Eddy Hypothesis and logarithmic velocity profile like atmospheric surface layer (Townsend, 1976), which has been deliberately studied in these years. However, for the characteristics of dune-field roughness sublayer, it is still mysterious due to the complex dune interactions and limited field experimental datasets.

Considering the huge costs of realistic dune-field experiment or simulation, lots of researchers start from isolated topographies (Omidyeganeh and Piomelli, 2013b; Omidyeganeh et al., 2013; Bristow et al., 2018; Palmer et al., 2012b; Bristow et al., 2017). Although without realistic datasets supports, a common feature of the turbulent coherency within DFSL is that the large coherent vortex structures, perturbing sediment saltations on dune surfaces, keeps getting updated in shear layer when geological patterns are affected by local fluid loading, which could also impact the aloft boundary layer turbulent structure in a profound way. The similar flow properties have been widely founded in Finnigan et al. (2009); Bailey and Stoll (2016); Finnigan (2000) in vegetation roughness sublayer. Bailey and Stoll (2016) has proposed the genesis of coherent structures in vegetative roughness sublayer using LES, which is a evolving progress from spanwise Kelvin–Helmholtz vortex rollers to couples of head-up and head-down hairpin vortices. Indeed, these hairpin vortices are stimulated due to mixing layer eddies and local turbulent ejection and sweep events beyond canopies. To recover the entire turbulence developing progress over canopy, Reynolds-averaged flow field, retrieved from a precursor simulation, is used to initiate simulation. In this work, a precursor simulation is used to achieve Reynolds-averaged datasets in dune field and to be the initial condition in idealized and realistic cases. The results exhibit similar and different flow characteristics in DFSL comparing with vegetative canopy, where streamwise and spanwise rollers are the original vorticity for hairpin vortex shedding in large dune and small dune wake, respectively. In fact, the special morphology of dune such as crescentic features and sparse roughness distributions in dune-field are the crucial reason to induce such difference DFSL (Anderson and Chamecki, 2014).

Turbulence with in the roughness sublayer is charaterized by coherent structures with a geometric macroscale on the order of the individual roughness element height, h (Castro, 2007). The roughness length scale z_{RSL}, scales linearly with h, and a consensus range is generally $2 \lesssim z_{RSL} \lesssim 5$ (Grass, 1971; Raupach et al., 1991; Flack and Schultz, 2010). In the inertial sublayer above the roughness sublayer, wall-normal mechanical shear is responsible for the production of a spectrum of motions, from attached-eddy motions predicted upon distance from the wall (Townsend, 1976), to superimposed large-scale motions meandering throughout the domain (Hutchins and Marusic, 2007). Mixing-layer is generated due to Kelvin–Helmholtz instability, which could emerge when there is shear in a single continuous fluid, or there is a velocity difference across the interface (Funada and Joseph, 2001). Finnigan et al. (2009); Bailey and Stoll (2016) have revealed mixing-layer analogy of vegetation canopy shear layer, where the dominance of turbulent sweeps can transport high momentum flux and turbulent mixing to higher elevations. Chauhan et al. (2014) have experimentally displayed vorticity thickness, l_ω can represent coherent eddy spatial extents in mixing layer. Pan and Chamecki (2016) recently has revealed turbulent dissipation length, $l_\epsilon = u_*^3/\epsilon$, is an extraordinarily metric length unit for turbulent coherence length scale at certain range of elevations beyond vegetation canopies. To explore the mixing-layer analogy in dune-field roughness sublayer and channel-flow turbulent attributes within inertial layer, three relative flow length scales have been used to normalize integral lengths. The results displayed in Chapter 5 are showing integral length scale in DFSL contains a self-similarity to streamwise interdune space and evident mixing-layer characteristics, while wall-turbulence attribute is also verified within inertial sublayer overlaying DFSL.

1.4 This Work

This work is focusing on three aspects of dune-field flow: *(i)* dune-field flow statistics and coherency (Chapter 3); *(ii)* dune-field coherent structure genesis (Chapter 4); *(iii)* dune-field boundary layer analysis (Chapter 5). At the very beginning, Chapter 2 deliberately introduces Large-Eddy Simulation method and all numerical cases used in this work. In Chapter 3, the turbulent statistics and turbulent coherent structures will be displayed. Section 3.1 is focusing on two-dimensional(2D) flow statistics, where "flow channeling" and "wake veering" are meandering due to the downwind dune obstruction. Section 3.2 and 3.3 show hairpin vortices shedding off from dune brinklines are in certain pattern according to wavelet analysis results, which is under a constant normalized frequency, $St = 0.25$, where St is Strouhal number, and associated with a local dune crest height correlated streamwise shedding distance, $\lambda \sim h(\boldsymbol{x})$. A persistent pseudo-streamwise vortex roller has been found is scouring sediments at interdune region. Instantaneous Q criterion isosurfaces precisely capture the growing processes in Section 3.4 which is found to be sustained by vorticity stretching via the analysis of streamwise vorticity budget from Reynolds-averaged streamwise vorticity transport equation in Section 3.5. To verify the sediment erosion enhancement triggered by flow channeling and sediment scour, the asymmetric distribution of surface friction velocity (obtained from Immersed Boundary Method) in interdune region has been captured by leveraging Bagnold Relation to retrieve threshold friction velocity. Chapter 4 studies the turbulence evolving and coherent structure genesis by using Reynolds-averaged flow datasets as initial conditions. Streamwise and spanwise rollers are the original instability due to the flow channeling and Kelvin–Helmholtz phenomenon, respectively. Chapter 5 reveal two sublayers composing dune-field boundary layers which are dune-field roughness sublayer (DFSL) and inertial sublayer. Dune-field roughness sublayer has found to range two to three dune crest height, where strong turbulent mixing enhances the propagations of momentum flux to higher elevations. Mixing-layer properties have been validated within DFSL via vorticity thickness correlated turbulent coherent length scales. While, inertial sublayer is found overlaying on DFSL and keeps wall-turbulence structures. In both Chapter 4 and 5, realistic case results are displayed to verify the credibility of preceding conclusions drawn from idealized cases. At the end of this work, experimental validation and grid insensitivity highlight the fidelity of LES datasets in Appendix A and B. A variable list is summarized at the end of this work for reading convenience. Note that, in this work, the terminology – hairpin vortex, indicates the turbulent coherent structure triggered by obstructing effects of dune features, which is not same as the near-wall vortical structures in Zhou et al. (1996).

CHAPTER 2

LARGE-EDDY SIMULATION & CASES

Recently, Computational Fluid Dynamics (CFD) method benefits a wide range of researches such as biomedicine, environment, geoscience and so forth, wherein different length scales of fluid are involved in these CFD simulations, especially in turbulent flow which consisted of a broad range of spectrum. To recover the geophysical fluid field, Direct Numerical Simulation (DNS) could be a promising methodology, resolving turbulence from Kolmogorov scale to the maximum of numerical length scale (Pope, 2000). However, DNS is too "expensive" for most geophysical fluid simulations due to the critical computational resource need in high Reynolds number flow regime. In contrast, LES can approach highly credible results with an acceptable numerical requirement (Metias, 1964). In this chapter, Large-Eddy Simulation method will be detailed discussed. Meanwhile, in Section 2.2, all numerical cases spatial and numerical information will be provided.

2.1 Large-Eddy Simulation

In Large-Eddy Simulation (LES) method, the filtered three-dimensional transport equation, incompressible momentum,

$$D_t\tilde{\boldsymbol{u}}(\boldsymbol{x},t) = \rho^{-1}\boldsymbol{F}(\boldsymbol{x},t), \tag{2.1}$$

is solved, where ρ is density, $\tilde{\cdot}$ denotes a grid-filtered quantity, $\boldsymbol{u}(\boldsymbol{x},t)$ is velocity (in this work, u, v, w are corresponded to velocity in streamwise, spanwise and wall-normal direction, respectively) and $\boldsymbol{F}(\boldsymbol{x},t)$ is the collection of forces (pressure correction, pressure gradient, stress heterogeneity and obstacle forces). The grid-filtering operation is attained here via convolution with the spatial filtering kernel, $\tilde{\boldsymbol{u}}(\boldsymbol{x},t) = G_\Delta \star \boldsymbol{u}(\boldsymbol{x},t)$, or in the following form

$$\tilde{\boldsymbol{u}}(\boldsymbol{x},t) = \oint G_\Delta(\boldsymbol{x}-\boldsymbol{x}',t)\boldsymbol{u}(\boldsymbol{x}',t)\mathrm{d}\boldsymbol{x}', \tag{2.2}$$

where Δ is the filter scale (Meneveau and Katz, 2000). A right-hand side forcing term, $-\nabla\cdot\mathsf{T}$, will be generated after the filtering operation to momentum equation, where $\mathsf{T} = \langle \boldsymbol{u}' \otimes \boldsymbol{u}' \rangle_t$ is the subgrid-scale stress tensor and $\langle . \rangle_a$ denotes averaging over dimension, a (in this article, rank-1 and -2 tensors are denoted with bold-italic and bold-sans relief, respectively).

For the present study, $D_t\tilde{\boldsymbol{u}}(\boldsymbol{x},t) = \rho^{-1}\boldsymbol{F}(\boldsymbol{x},t)$ is solved for a channel-flow arrangement (Albertson and Parlange, 1999; Anderson and Chamecki, 2014), with the flow forced by a pressure gradient in streamwise direction, $\boldsymbol{\Pi} = \{\Pi, 0, 0\}$, where

$$\Pi = [\mathrm{d}P_0/\mathrm{d}x]\,\frac{H}{\rho} = \tau^w/\rho = u_*^2 = 1, \tag{2.3}$$

which sets the shear velocity, u_*, upon which all velocities are non-dimensionalized. In simulation, all length scales are normalized by H, which is the surface layer depth, and velocity are normalized by surface shear velocity. $D_t\tilde{\boldsymbol{u}}(\boldsymbol{x},t) = \rho^{-1}\boldsymbol{F}(\boldsymbol{x},t)$ is solved for high-Reynolds number, fully-rough conditions (Jimenez, 2004), and thus viscous effects can be neglected in simulation, $\nu\nabla^2\tilde{\boldsymbol{u}}(\boldsymbol{x},t) = 0$. Under the presumption of $\rho(\boldsymbol{x},t) \to \rho$, the velocity vector is solenoidal, $\nabla\cdot\tilde{\boldsymbol{u}}(\boldsymbol{x},t) = 0$. During LES, the (dynamic) pressure needed to preserve $\nabla\cdot\tilde{\boldsymbol{u}}(\boldsymbol{x},t) = 0$ is dynamically computed by computation of $\nabla\cdot[D_t\tilde{\boldsymbol{u}}(\boldsymbol{x},t) = \rho^{-1}\boldsymbol{F}(\boldsymbol{x},t)]$ and imposing $\nabla\cdot\tilde{\boldsymbol{u}}(\boldsymbol{x},t) = 0$, which yields a resultant pressure Poisson equation. Figure 2.1 shows the LES schematic diagram associated with boundary conditions in simulation.

The channel-flow configuration is created by the aforementioned pressure-gradient forcing, and the following boundary condition prescription: at the domain top, the zero-stress Neumann boundary condition is imposed on streamwise and spanwise velocity, $\partial\tilde{u}/\partial z|_{z/H=1} = \partial\tilde{v}/\partial z|_{z/H=1} = 0$. The zero vertical velocity condition is imposed at the domain top and bottom, $\tilde{w}(x,y,z/H=0) = \tilde{w}(x,y,z/H=1) = 0$. Spectral discretization is used in the horizontal directions, thus imposing periodic boundary conditions on the vertical "faces" of the domain, *vis.*

$$\phi(x + mL_x, y + nL_y, z) = \phi(x,y,z), \tag{2.4}$$

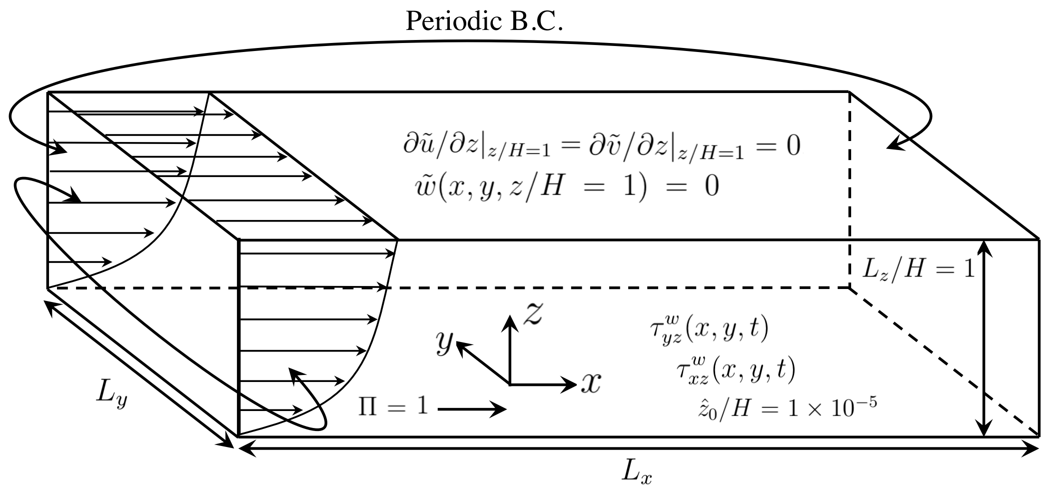

Figure 2.1. The schematic diagram of LES domain including boundary condition informations. Spatial extents are noted as L_x, L_y and L_z in streamwise, spanwise and wall-normal direction, respectively. Periodic boundary condition is adopted for four vertical walls (marked by black solid curved quivers). The coordinate system is denoted in the domain. Logarithmic profile for streamwise velocity against wall-normal elevation can be achieved in LES as the velocity profiles plots at entrance in diagram. The flow is forced by a pressure gradient $\Pi = 1$ in streamwise direction, x, which sets the shear velocity, u_*. Meanwhile, on ground, surface shear is executed as τ^w_{xz} and τ^w_{yz} as Equation 2.5 and 2.6. $\hat{z}_0/H$ is set on the ground for a prescibed roughness length (Anderson, 2012; Anderson and Meneveau, 2010, 2011).

and imposing spatial homogeneity in the horizontal dimensions. The code uses a staggered-grid formulation (Albertson and Parlange, 1999), where the first grid points for $\tilde{u}(\boldsymbol{x}, t)$ and $\tilde{v}(\boldsymbol{x}, t)$ are located at $\delta z/2$, where $\delta z = H/N_z$ is the resolution of the computational mesh in the vertical (N_z is the number of vertical grid points). Grid resolution in the streamwise and spanwise direction is $\delta x = L_x/N_x$ and $\delta y = L_y/N_y$, respectively, where L and N denote horizontal domain extent and corresponding number of grid points (subscript x or y denotes streamwise or spanwise direction, respectively). Table 2.1 provides a summary of the domain attributes for the different cases, where the domain height has been set to the depth of the surface layer, $L_z/H = 1$.

At the lower boundary, surface momentum fluxes are prescribed with a hybrid scheme leveraging an immersed-boundary method (IBM)(Anderson and Meneveau, 2010; Anderson,

2012) and the equilibrium logarithmic model (Piomelli and Balaras, 2002) , depending on the digital elevation map, $h(x, y)$. When $h(x, y) < \delta z/2$, the topography vertically unresolved, and the logarithmic law is used:

$$\tau^{w}_{xz}(x, y, t) = -\left[\frac{\kappa U(x, y, t)}{\log(\frac{1}{2}\delta z/\hat{z}_0)}\right]^2 \frac{\bar{\tilde{u}}(x, y, \frac{1}{2}\delta z, t)}{U(x, y, t)} \tag{2.5}$$

and

$$\tau^{w}_{yz}(x, y, t) = -\left[\frac{\kappa U(x, y, t)}{\log(\frac{1}{2}\delta z/\hat{z}_0)}\right]^2 \frac{\bar{\tilde{v}}(x, y, \frac{1}{2}\delta z, t)}{U(x, y, t)} \tag{2.6}$$

where $\hat{z}_0/H = 1 \times 10^{-5}$ is a prescribed roughness length, $\bar{\tilde{\cdot}}$ denotes test-filtering (Germano, 1992; Germano et al., 1991) (used here to attenuate un-physical local surface stress fluctuations associated with localized application of Equation 2.5 and 2.6 (Bou-Zeid et al., 2005)), and $U(x, y, \frac{1}{2}\delta z, t) = (\bar{\tilde{u}}(x, y, \frac{1}{2}\delta z, t)^2 + \bar{\tilde{v}}(x, y, \frac{1}{2}\delta z, t)^2)^{1/2}$ is magnitude of the test-filtered velocity vector. Where $h(x, y) > \frac{1}{2}\delta z$, a continuous forcing Iboldsymbol is used (Anderson, 2012; Mittal and Iaccarino, 2005), which has been successfully used in similar studies of turbulent obstructed shear flows (Anderson and Chamecki, 2014; Anderson et al., 2015; Anderson, 2016). The immersed boundary method computes a body force, which imposes circumferential momentum fluxes at computational "cut" cells based on spatial gradients of $h(x, y)$:

$$\boldsymbol{f}(\boldsymbol{x}, t) = -\frac{\tilde{\boldsymbol{u}}(\boldsymbol{x}, t)}{\delta z} R(\tilde{\boldsymbol{u}}(\boldsymbol{x}, t) \cdot \nabla h), \tag{2.7}$$

where R is called Ramp Function (Anderson, 2012)

$$R(x) = \begin{cases} x & \text{for } x > 0, \\ 0 & \text{for } x \leqslant 0. \end{cases} \tag{2.8}$$

Equations 2.5 and 2.6 are needed to ensure surface stress is imposed when $h(x, y) < \frac{1}{2}\delta z$. Subgrid-scale stresses are modeled with an eddy-viscosity model,

$$\boldsymbol{\tau}^d = -2\nu_t \mathbf{S}, \tag{2.9}$$

where

$$\mathbf{S} = \frac{1}{2}(\nabla \tilde{\boldsymbol{u}} + \nabla \tilde{\boldsymbol{u}}^{\mathrm{T}}) \tag{2.10}$$

is the resolved strain-rate tensor. The eddy viscosity is

$$\nu_t = (C_s \Delta)^2 |\mathbf{S}|, \tag{2.11}$$

where $|\mathbf{S}| = (2\mathbf{S} : \mathbf{S})^{1/2}$, C_s is the Smagorinsky coefficient, and Δ is the grid resolution. For the present simulations, the Lagrangian scale-dependent dynamic model is used (Bou-Zeid et al., 2005). The simulations have been run for $N_t \delta_t U_0 u_{*,d} H^{-1} \approx 10^3$ large-eddy turnovers, where $U_0 = \langle \tilde{u}(x, y, (L_z - \delta z/2)/H = 1, t) \rangle_t$ is a "free stream" or centerline velocity. This duration is sufficient for computation of Reynolds-averaged quantities.

2.2 Cases

Previous section summarized the LES method used to model turbulent flow over the realistic terrestrial dune field and idealized barchan dunes, which are shown and summarized in Table 2.1 and Figure 2.2 in this current section. Since in Chapter 1 the necessity of realistic and idealized dune comparison has been emphasized, this work executed high resolution LES to a portion of White Sands National Monument (WSNM) Digital Elevation Map (DEM). The idealized cases are consisted of two crescentic barchan, aimed to recover the collision progress in Figure 1.4. The spatial details such streamwise, spanwise offset and asymmetric length of downwind dune in idealized cases are summarized in Table 2.1. Besides, Table 2.1 also summarizes the attributes of the numerical simulations for LES modeling of flow over the dune fields. In Table 2.1, Cases WSNMi corresponds with the realistic dune simulation, where $i = 1, 2, 3$ indicates different computational mesh resolutions (lowest to highest). While, Cases Si, Si_l and Si' all corresponds with idealized cases. However, Si_l indicates the low-resolution cases. And Si' corresponds with the comparative cases for Si, where asymmetric erosion is ignored in Si'. The number $i = 1, 2, 3, 4$ here denotes different stages of

Table 2.1. Summary of simulation attributes ($H = 100$ m, $\chi = \mathcal{V}_s/\mathcal{V}_l$, where $\mathcal{V}_s$ and $\mathcal{V}_l$ is volume of small and large dune, respectively) and dune field configurations considered for present article.

Case	N_x	N_y	N_z	L_x/H	L_y/H	L_z/H	$max(h)/H$	s_x/h	s_y/h	χ	$\Delta x/h$
WSNM1	128	128	128	7.68	7.68	1	0.119	/	/	/	/
WSNM2	256	256	256	7.68	7.68	1	0.119	/	/	/	/
WSNM3	384	384	128	7.68	7.68	1	0.119	/	/	/	/
$S1_l$	128	128	128	8	8	1	0.125	/	/	/	0.0
$S2_l$	128	128	128	8	8	1	0.125	20.0	5.2	0.125	0.0
$S3_l$	128	128	128	8	8	1	0.125	16.0	5.2	0.125	4.0
$S4_l$	128	128	128	8	8	1	0.125	10.5	5.2	0.125	8.0
$S3_l'$	128	128	128	8	8	1	0.125	16.0	5.2	0.125	0.0
$S4_l'$	128	128	128	8	8	1	0.125	10.5	5.2	0.125	0.0
$S1$	256	256	256	8	8	1	0.125	/	/	/	0.0
$S2$	256	256	256	8	8	1	0.125	20.0	5.2	0.125	0.0
$S3$	256	256	256	8	8	1	0.125	16.0	5.2	0.125	4.0
$S4$	256	256	256	8	8	1	0.125	10.5	5.2	0.125	8.0
$S3'$	256	256	256	8	8	1	0.125	16.0	5.2	0.125	0.0
$S4'$	256	256	256	8	8	1	0.125	10.5	5.2	0.125	0.0
$S5$	128	128	128	8	8	1	0.125	20.0	3.38	0.125	0.0

idealized cases in Table 2.1 and Figure 2.2. Through the manuscript, most portions of results are achieved from highest mesh resolution cases. The comparison between different grid resolution cases are displayed in Appendix B to demonstrate the numerical grid insensitivity. Moreover, the PIV results and comparison with LES are displayed in Appendix A. In Table 2.1, h denotes the small dune crest height in idealized cases; while h_w denotes the maximum of WSNM height.

2.2.1 Idealized Case

The idealized cases shown in Figure 2.2 Panel (a) capture the instantaneous realizations of a so-called offset interaction (Hersen and Douady, 2005; Hersen et al., 2004; Kocurek et al., 2007) in Figure 1.4. The interactive collision are triggered by the different migration speeds, since the solitary dune migration speed is inversely proportional to the dune crest

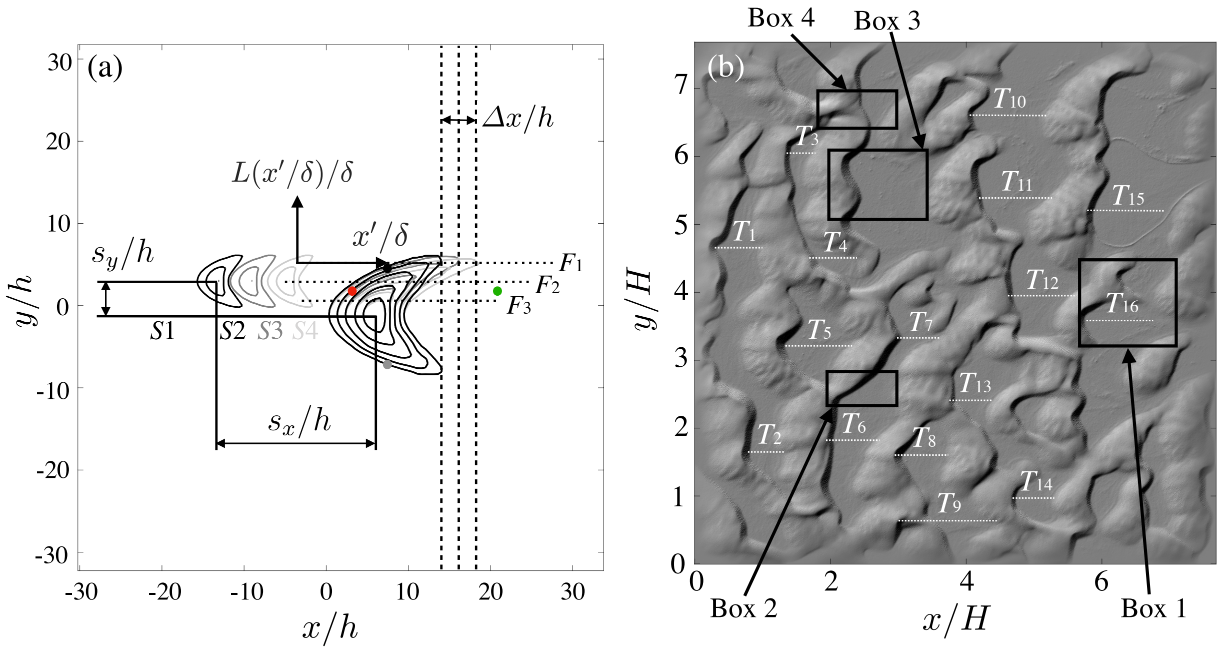

Figure 2.2. The idealized and realistic topographies in this work: (a) Reduced order of interacting barchan dunes in different stages. Case $S1$ is a solitary big barchan dune. While, Case $S2$ to $S4$ correspond with instantaneous realization of an offset interaction which is inspired by (Hersen and Douady, 2005). s_x/h denotes streamwise offset, s_y/h denotes spanwise offset, and Δx denotes the large dune asymmetry. The sampling points are selected to record turbulence transient signal: red point – x_L; green point – x_C; black point – x_F; and gray point – x_E. The horizontal dashed lines denoted by F_1, F_2 and F_3 denote the spanwise locations at which integral length profiles will shown Chapter 5. Panel (a) also shows the origin for a local axis, x', which will be used in the Chapter 5. (b) The White Sands National Monument DEM (The DEM is generously provided by Prof. Gary Kocurek and David Dame in University of Texas at Austin.). The white dotted lines denote locations at which turbulence statistics are provided in Chapter 5. The “Box 1”, “Box 2”, “Box 3” and “Box 4” annotations highlight subregions where development of vortical flow structure is studied in Figure 4.7. The Transects T_1 to T_{16} are the chosen locations for the integral length study in Chapter 5.

height (Kocurek and Ewing, 2005). Thus, the upwind small dune will move faster than the downwind big dune in Figure 2.2, where s_x/h is two dune streamwise distance (the streamwise distance between dune crests). But two dunes can keep a constant spanwise offset s_y/h during collision (the spanwise distance between dune crests). As interaction advances the large dune is known to exhibit a prominent asymmetry in the leeward side of the smaller dune (refer Figure 1.4 to see the mobile-bed flume experiment results), which is accounted as Δx for the quantification of the asymmetry in Table 2.1. Case $S1$ is a solitary large barchan dune. In Case $S2$ to $S4$, a small dune placed in the upstream of that with a constant $s_y/h = 5.2$ but decreasing $s_x/h = 20.0, 16.0, 10.5$ in $S2$, $S3$ and $S4$ respectively. The small dune is geometrically similar to the large dune, but its streamwise, spanwise, and vertical extent is decreased by 50%. Thus the volumetric ratio of two dunes is $\chi = \mathcal{V}_s/\mathcal{V}_l = 0.125$, where $\mathcal{V}_s$ and $\mathcal{V}_l$ are small and large dune volume respectively. The large-dune asymmetry Δx is considered to capture the large dune asymmetric erosion in Figure 1.4, which increases as small dune interacts the downflow dune. $S3'$ and $S4'$ keep the same spatial attributes with $S3$ and $S4$, but without large-dune asymmetry. The idealized dune simulation results have been verified through PIV flow field visualization in Appendix A (Results have been reproduced with permission from (Wang et al., 2016)). Mover, $S5$ keeps same spatial properties with experimental case, for a effective comparison with PIV data in Appendix A.

2.2.2 Realistic Case: White Sands National Monument

The White Sands National Monument (WSNM) dune field is located in the Tularosa Basin of the Rio Grande Rift, between the San Andres and Sacramento Mountain Ranges, in souther New Mexico. The WSNM dune field consists of a core of barchan dunes, which abruptly transition to parabolic dunes (Ewing and Kocurek, 2010a,b; Jerolmack and Mohrig, 2005). Recently, the increasing trend of aerodynamic roughness of dune field in the upcoming wind direction has been imputed to the developing of the internal momentum boundary layer (Jerolmack and Mohrig, 2005). The WSNM DEM is taken from an existing LiDAR survey. (Anderson and Chamecki, 2014) has chosen a series windows of WSNM DEM and analyzed DFSL which depicts profound turbulence enveloped beneath shear layers for elevation less than two to three times the dune crest height. For a comprehensive understanding of the turbulence coherence in DFSL, a portion of WSNM DEM has been chosen for this study. Figure 2.2 (b) displays the subset area of WSNM used as a lower boundary during LES. In terms of geometric complexity, the DEM serves as an 'upper limit' with its multiscale distribution of dune sizes and shapes. Importantly, the feature of WSNM reveal the most common and typical dune field which includes overlapping and collision with adjacent dunes, which confounds efforts to isolate universal flow pattern.

Two *a priori* modifications are imposed on the chosen DEM: *(i)* the lowest elevation is subtracted from the DEM, which imposes the minimum elevation of DEM is 0, $min(h(\boldsymbol{x})) = 0$; *(ii)* a two-dimensioanl windowing function $\mathcal{W}(x, y) = a(x)a(y)$ to the resulting topography in order to impose periodicity on the underlying topography $h(x, y)$. Hence, the modified topography is the Hadamard product $h(x, y) \Rightarrow h(x, y)\mathcal{W}(x, y)$. Periodicity is needed due to the use of spectral decomposition of flow quantities in LES. The Gibbs phenomena will contaminate the results if $h(x, y)$ is not periodic (Tseng et al., 2006). The windowing function is in the following format:

$$a(x) = \begin{cases} 1.0 & \text{for } 0 \leqslant \|x - x_c\| < \gamma L, \\ cos\left[\frac{(x-x_c)/H-\gamma(L/H)}{2(1-\gamma)}\right] & \text{for } \gamma L \leqslant \|x - x_c\| < L, \end{cases} \tag{2.12}$$

where L is the length of simulation domain ($L = 768m$ in this work), H is the simulation characteristic length scale to normalize all lengths ($H = 100m$ in this work, which is sufficient to recover dune roughness sublayer and inertial sublayer). The parameter γ imposes the circumjacent width over which the topography around the edges of the focus area is forced toward $h(x, y) = 0$, and x_c is the coordinate of the center of the domain. In the present study, we select $\gamma = 0.85$, which imposes that the outermost 15% of $h(x, y)$ gradually tends toward zero (see Figure 2.2 (b)).

CHAPTER 3

DUNE-FIELD FLOW STATISTICS AND COHERENCY

The simulation results are displayed in the current Chapter to illustrate the turbulence structure in idealized and realistic dune field. In Section 3.1, the two-dimensional visualization of turbulent statistics display a homogeneous pattern in barchan dune wake, where wake centerline in different cases displays a monotonic heterogeneity which could be nonlinearly correlated to the streamwise offset s_x/h. Section 3.2 resoundingly demonstrates the hairpin vortex shedding, the deep observation of which is processed in Section 3.2. Section 3.3 reveals the hairpin vortex shedding emerges at an normalized frequency value, $St = 0.25$. Meanwhile, the interdune roller, one of the great findings in the work, is comprehensively discussed in Section 3.4 and 3.5. All the LES data in Section 3.1 and 3.2 is collected from fully developed turbulent flow field. [1] .

3.1 2D Flow Visualization

Figure 3.1 (a-f) shows the Reynolds-averaged wall-normal vorticity in the streamwise-spanwise plane at big dune crest height elevation, where $\langle\tilde{\omega}_z\rangle_t(x, y, z/h = 1.0) = \partial_x\langle\tilde{v}\rangle_t - \partial_y\langle\tilde{u}\rangle_t \approx -\partial_y\langle\tilde{u}\rangle_t$, since the magnitude of spanwise heterogeneities critically exceed the magnitude of streamwise heterogeneities because of the virtue of shear layer in wake flow (Wang et al., 2016). Thus the contour of $\langle\tilde{\omega}_z\rangle_t$ could reveal the wake shear intensity. Meanwhile, with the application of the right-hand rule, $\langle\tilde{\omega}_z\rangle_t < 0$ and $\langle\tilde{\omega}_z\rangle_t > 0$ show the rotating direction of the flow shed from the "up" and "bottom" horn. For the completeness, Figure 3.1 (g,h) displays the wake centerline which gets located via the points on $\langle\tilde{\omega}_z\rangle_t(\boldsymbol{x}) = 0$. In Figure 3.1 (g,h),

[1] This chapter is based on the journal papers: (i)Wang C, Tang Z, Bristow N, et al. Numerical and experimental study of flow over stages of an offset merger dune interaction[J]. *Computers & Fluids*, 2017, 158: 72-83. (ii) Wang C, Anderson W. Large-eddy simulation of turbulent flow over spanwise-offset barchan dunes: Interdune vortex stretching drives asymmetric erosion[J]. *Physical Review E*, 2018, 98(3): 033112.

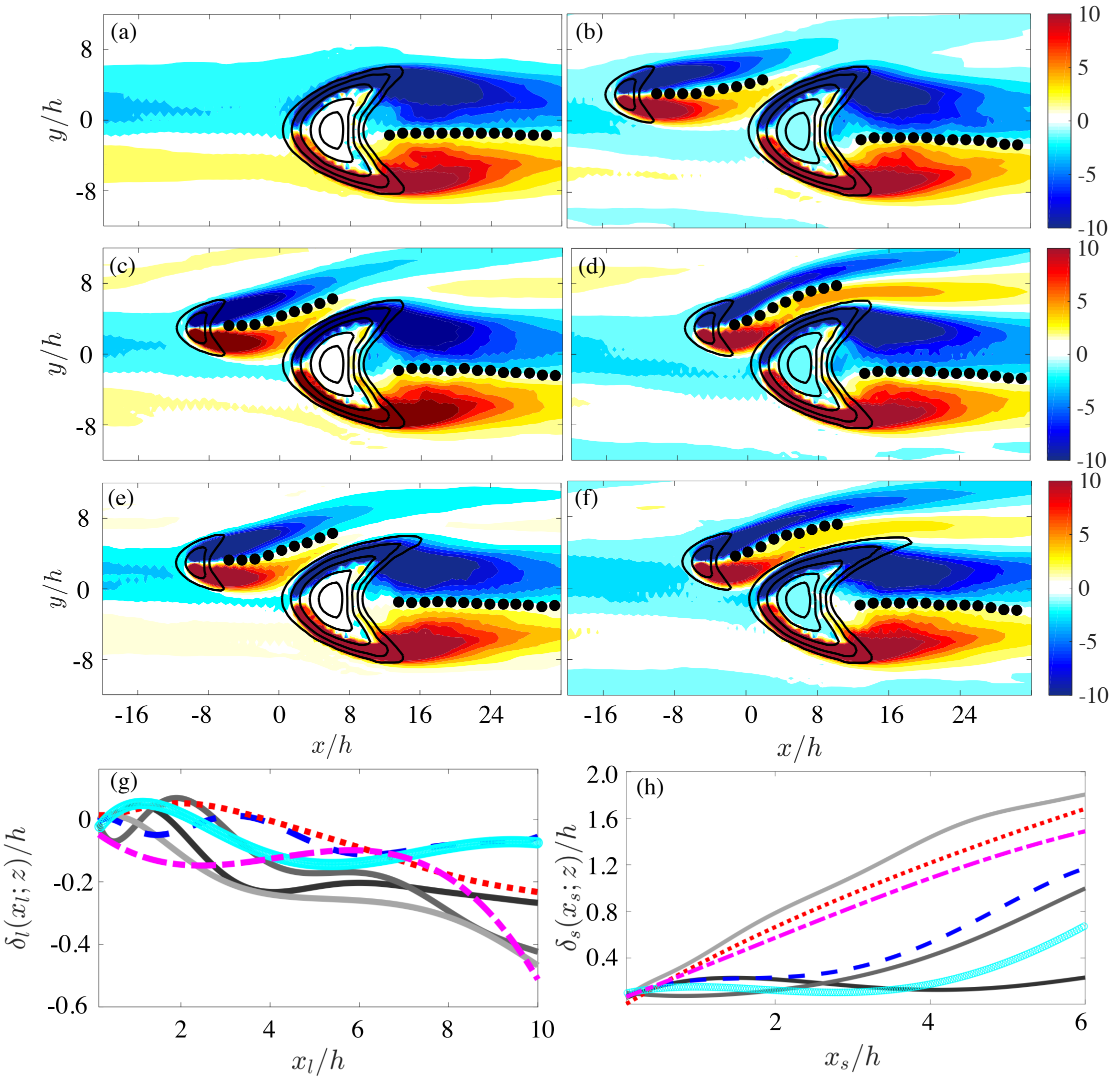

Figure 3.1. Color flood contour of Reynolds-averaged vertical vorticity, $\langle\tilde{\omega}_z\rangle_t(x, y, z/h = 1.0)$, at wall-normal elevation, $z/h = 1.0$, for Case $S1_l$ (a); $S2_l$ (b); $S3'_l$ (c); $S4'_l$ (d); $S3_l$ (e); $S4_l$ (f) (see Table 2.1 for topography details). The low-pass filtered datapoints for the wake are included on the color contour, emanating from the small and large dunes, $\delta_s(x_s; z/h = 1.0)$ and $delta_l(x_l; z/h = 0.5)$ respectively. Low-pass filtered wake profiles emanating from large and small dunes, $\delta_l(x_l; z/h = 1.0)$ in Panel (g) and $\delta_s(x_s; z/h = 1.0)$ Panel (h), respectively, where local coordinate originates at respective dune crest. Black, gray and light gray solid lines correspond with Case $S2_l$, $S3'_l$, $S4'_l$. Dashed blue and dotted red lines correspond with $S3_l$ and $S4_l$. While, cyan circles and dash-dot magenta line correspond with $S3'$ and $S4'$ respectively (Table 2.1 provides comprehensive simulation details).

the small and large dune wake centerline spanwise offset is denoted by $\delta_s(x_s; z)$ and $\delta_l(x_l; z)$, respectively, where x_s and x_l are the origins of local coordinate systems.

In Figure 3.1, it is easily to capture the symmetrical distribution of the negative and positive rotating shear flow in the wake of Case $S1_l$. The symmetric crescentic feature without interactive collision makes the wake flow into such pattern. However, the upcoming small dune entirely disrupts such flow pattern because of the spanwise-staggered offset s_y/h. In Case $S2_l$, the small dune wake veers into the interdune region, where the velocity magnitude gets elevated because of the downflow dune frontal face obstruction, which is so-called "flow channeling" (Wang et al., 2016). Considering the mass conservation of incompressible flow $\bigtriangledown \cdot \boldsymbol{u} = 0$, the shear flow behind small dune is laterally displaced because of the downstream object and thus its momentum must increase in the channel region. The enhanced turbulence is founded in Figure 3.2 Panel (a) PDF plots, which reminds us the strong sediment saltation events will happen in flow channeling region frequently based on $q(\boldsymbol{x}, t) \sim (u_*(\boldsymbol{x}, t))^3$ (refer Figure 3.6 which shows higher sediment saltation magnitude in flow channeling region). The result is also consistent with the experimental observation in Figure A.1, where strong turbulent mixing process is found in interdune regions. While, not like $S1_l$, the distribution of $\langle \tilde{\omega}_z \rangle_t$ in the vicinity of large dune is asymmetric. The maximum of $\langle \tilde{\omega}_z \rangle_t$ magnitude for negative and positive rotation gets rotated, where the negative (blue) and positive (red) areas have migrated upflow and downflow respectively. For the consistency, equivalent colorbar limits have been adopted in Figure 3.1 (a-f), but, in fact, we found the negative limitation of the colorbar is approximately three times the positive limit.

With the interdune space shrinking in Case $S3_l'$ and $S4_l'$, Figure 3.1 (c,d), the asymmetric trend of the wake flow becomes severer according to the $\langle \tilde{\omega}_z \rangle_t$ distribution. The elevated magnitude of $\langle \tilde{\omega}_z \rangle_t$ across the large dune stoss face can be viewed as a proxy of surface stress which could be the trigger of the asymmetric erosion of the large dune "top" horn. The meandering of the $\langle \tilde{\omega}_z \rangle_t$ along the flow channeling in small dune wake also gets enhanced decreasing s_x/h, just like the streamwise velocity $\langle u(\boldsymbol{x}, t)\rangle_t$. In Figure 3.1 (g,h), the heterogeneity of wake centerline veering is far more obvious in $S3_l'$ (gray line) and $S4_l'$ (light gray line). However, the small dune wake veering is more sensitive to s_x/h at $z/h = 1.0$.

Figure 3.1 (e,f) reveals the difference between $S3_l$ and $S3_l'$ (dashed blue and gray), $S4_l$ and $S4_l'$ (dotted red and light gray) in $\delta_l x_l; z/h$. Since the upflow dune elevates the momentum flux in the interdune region, the asymmetric dune is able to provide a larger frontal area, absorbing the interdune momentum fluxes, which can help to attenuate flow asymmetry.

After recording the wake profiles of Figure 3.1 (a-f) and compiling them into two coordinates, $\delta_s(x_s; z/h = 1.0)/h$ and $\delta_l(x_l; z/h = 1.0)/h$, respectively in Panel (g) and (h). As per the caption, the black, gray and light gray profiles correspond with Case $S2_l$, $S3_l'$, $S4_l'$, respectively. It is obvious that "wake veering" gets intensified monotonically as s_x/h decreases. The cyan circles and dash-dot magenta line correspond with $S3'$ and $S4'$, which are used to shows the grid insensitivity of simulation here and displays a close agreement between $S3_l'$ and $S3'$, $S4_l'$ and $S4'$.

According to this section, the notion of "wake veering" has been developed and resulted in the interactive collision with spanwise-staggered offset. Flow channeling effect has also been discussed here for the future explanation of the coherent structure evolving. In the following section, the coherent structures beneath dune crest will be displayed in three-dimension through instantaneous and conditionally-averaged datasets. Through wavelet decomposition, the corresponded coherence will be studied in terms of the energy spectrum.

3.2 3D Flow Visualization

In the current section, turbulent coherence will be discussed through multiple methodologies, the results of which show two types of large turbulence structure in DFSL – hairpin vortex and streamwise rotating interdune roller. Section 3.2 demonstrates the hairpin vortices shedding triggered by the dune crescentic brinkline associated with a constant frequency value through the energy spectrum analysis of instantaneous and conditionally-averaged datasets. The PDF profiles designate the significance of flow channeling in turbulent mixing processes. While, Section 3.4 provide us the understanding of turbulence coherence from the view of dune field morphodynamics (remind Figure 1.3 and 1.4 for the natural and experimental dune interaction), with differential helicity calculation and predicting the sediment saltation by using Bagnold scheme, both of which show a great consistency. Reynolds-averaged streamwise vorticity transport equation has been studied in Section 3.5, through that vortex stretching $\langle S_x(\boldsymbol{x}) \rangle_t$ has been deemed as the maintaining factor for interdune vortex roller. Figure 3.7 is used as a schematic model for the completeness.

In this section, two complementary aspects of idealized dune flow will be covered: *(i)* visualization of turbulent coherent structure via a vortex identifier derived from both conditionally-averaged and instantaneous flow data; *(ii)* wavelet decomposition given the significance of hairpin vortex shedding. Because the sediment saltation flux is severely affected by intermittent fluctuations of surface stress, it is necessary to consider the extreme condition of the flow attributes here (Hutchins et al., 2011; Wang and Anderson, 2018b). While, the instantaneous data will provide the most realistic flow structures in a larger range of turbulence length scales. Both of the datasets confirm the existence of hairpin vortices being shed from the dune brinkline. Through wavelet decomposition, the results also demonstrate the vortices surrounding the brinkline get produced at a dominant frequency.

After PDFs computation and threshold selection, we then run the LES for an additional period of time and sample the flow based on:

$$\frac{\widehat{\tilde{\boldsymbol{u}}}(\boldsymbol{x})}{u_*} = \left\langle \frac{\tilde{\boldsymbol{u}}(\boldsymbol{x}, t)}{u_*} \middle| \frac{\tilde{u}'(\boldsymbol{x}_L, t)}{u_*} > 2.5 \right\rangle_{N_s}, \tag{3.1}$$

where $\widehat{\cdots}$ denotes a conditionally-averaged quantity, and N_s is the number of times $\tilde{u}'(\boldsymbol{x}_L, t)/u_* > 2.5$. Having conditionally sampled the flow with Equation 3.1, we compute the Q criterion vortex identifier, which is derived from the velocity gradient tensor, $\mathbf{D} = \nabla \tilde{\boldsymbol{u}}$ (Jackson and

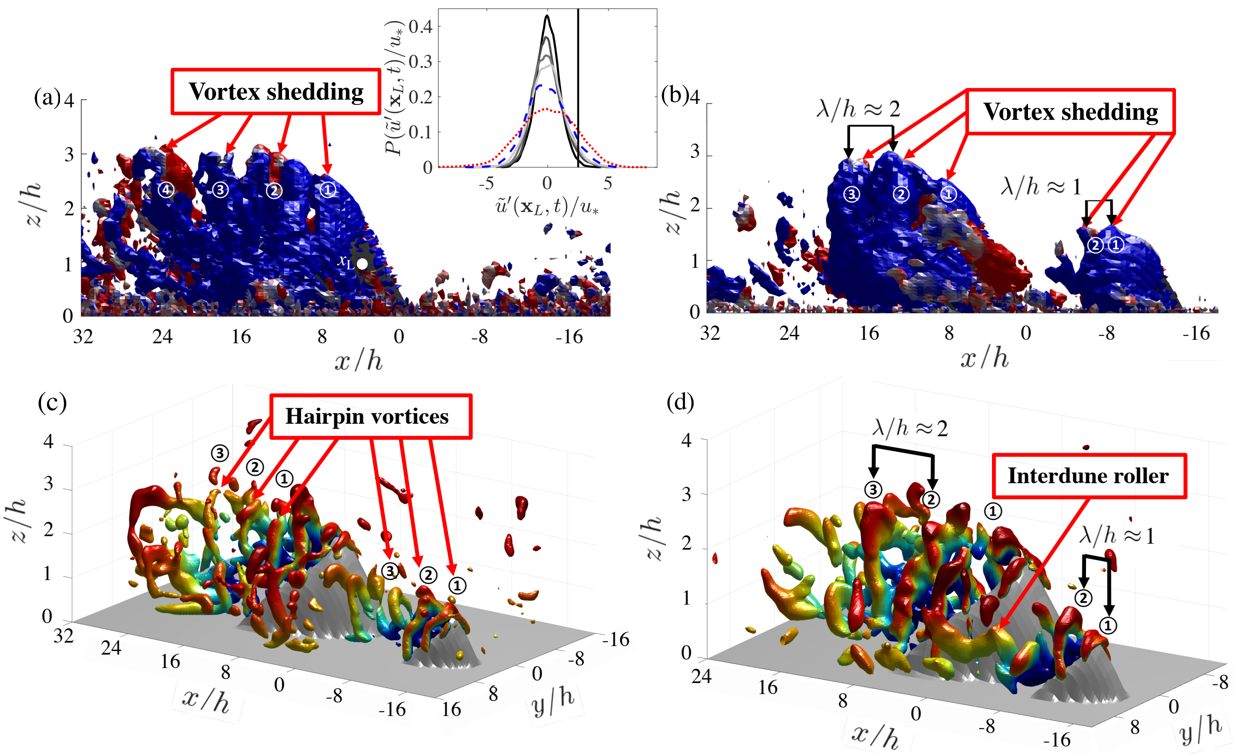

Figure 3.2. Streamwise–wall-normal visualization of conditionally-averaged Q criterion for $\widehat{Q} = 11$ signed by conditionally-averaged wall-normal rotating direction: Panel (a) and (b) corresponds with $S1_l$ and $S2_l$, respectively. Probability Density Function (PDF) of normalized streamwise velocity function at sampling position $\boldsymbol{x}_L$ is showed in Panel (a). Black, dark gray and light gray lines correspond with Cases $S1_l$, $S2_l$, $S3'_l$, $S4'_l$, respectively, while dashed blue and dotted red datapoints correspond with $S3_l$ and $S4_l$. Black vertical line denotes the conditional sampling threshold used here, which is $\tilde{u}'(\boldsymbol{x}_L, t)/u_* > 2.5$. Three-dimensional visualization of instantaneous Q criterion for $Q = 100$ signed by Reynolds-averaged streamwise velocity: Panel (c) and (d) show Case $S3'$ and $S4'$, respectively. Note numbered annotation of successive vortex cores emanating from dune brinkline, and vortex core spacing, λ/h, deduced from high-Reynolds number Strouhal number and advective velocity in vicinity of brinkline.

Hunt, 1975; Jeong and Hussain, 1995; Christensen and Adrian, 2001). $\mathbf{D}$ can be decomposed into its symmetric and anti-symmetric components, $\mathbf{D} = \mathbf{S} + \mathbf{\Omega}$, where $\mathbf{\Omega} = \frac{1}{2}\left(\nabla\tilde{\boldsymbol{u}} - \nabla\tilde{\boldsymbol{u}}^{\mathrm{T}}\right)$ and $\mathbf{S} = \frac{1}{2}\left(\nabla\tilde{\boldsymbol{u}} + \nabla\tilde{\boldsymbol{u}}^{\mathrm{T}}\right)$, allowing computation of the Q criterion with:

$$Q = \frac{1}{2}\left(\mathbf{S} : \mathbf{S} - \mathbf{\Omega} : \mathbf{\Omega}\right). \tag{3.2}$$

Figure 3.2 (a,b) display the isosurfaces of conditionally-averaged Q criterion for Case $S1_l$ and $S2_l$ (see Figure 2.2 inset for the conditional sampling threshold). The 3D isosurfaces reveal the existence of a train of vortex cores, advecting downstream from the dune brinklines (the vortex cores annotations have been added in (a) and (b) respectively). Figure 3.2 (c,d) show instantaneous Q criterion in Case $S3'$ and $S4'$, which are high-resolution cases (see Table 2.1 for simulation details). The instantaneous results capture the instant turbulence coherence structures, which consistently exhibit a discernible train of hairpin vortices shed from the dune brinkline, while one of which has captured the interdune roller (Figure 3.2 (d)). The interdune roller, we will show, is foremost in setting the asymmetric topology of the larger dune. The structure of successive hairpin heads resembles observations from canonical wall turbulence.

3.3 Wavelet Analysis

To explain the downstream proximal distances between successive vortex cores annotated in Figure 3.2, we have adopted global wavelet power spectrum via convolution of an input time series with a spectrum of wavelet functions to detect energetic peaks associated with vortex shedding downflow of large dune. Wavelet decomposition is a convenient tool for explaining the spectral density of input time series in joint time-frequency space (Cohen, 1989; Farge, 1992). For the current analysis, I have considered two signals, $\tilde{u}(\boldsymbol{x}_L, t)$ and $\tilde{u}(\boldsymbol{x}_C, t)$, discrete locations roughly downflow of the small and large dune, respectively (see Figure 2.2 (a), where $\boldsymbol{x}_L$ is red point, $\boldsymbol{x}_C$ is green point). The analysis is predicated based on the convolution of

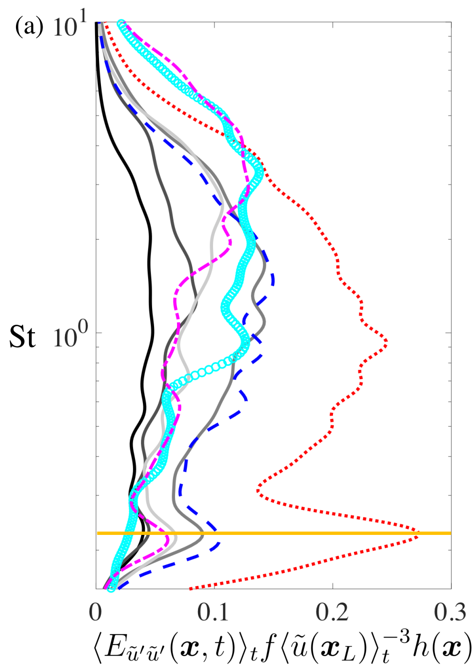

Figure 3.3. Global wavelet power spectrum of streamwise velocity fluctuation, for input time series from discrete locations $\boldsymbol{x}_L$ (a) and $\boldsymbol{x}_C$ (b). Black, dark gray, gray and light gray lines correspond with Case $S1_l$, $S2_l$, $S3'_l$ and $S4'_l$, respectively, dashed blue and dotted red lines correspond with $S3_l$ and $S4_l$, while cyan circles and dash-dotted magenta line correspond with $S3'$ and $S4'$, respectively. Horizontal orange line denotes $fh(\boldsymbol{x}_L)\langle\tilde{u}(\boldsymbol{x}_L)\rangle_t^{-1} = fh(\boldsymbol{x}_C)\langle\tilde{u}(\boldsymbol{x}_C)\rangle_t^{-1} = St = 0.25$, the high-Reynolds number asymptote.

$\tilde{u}'(\boldsymbol{x},t)$ with a wavelet (basis) function, $\psi(f)$, yielding an array of coefficients in joint time-frequency space. The square of the absolute value of the wavelet coefficients, divided by each frequency, yields spectral density defined in time-frequency space, $E_{\tilde{u}'\tilde{u}'}(\boldsymbol{x},t) f \langle \tilde{u}(\boldsymbol{x}_L)\rangle_t^{-3} h(\boldsymbol{x})$ and $E_{\tilde{u}'\tilde{u}'}(\boldsymbol{x},t) f \langle \tilde{u}(\boldsymbol{x}_C)\rangle_t^{-3} h(\boldsymbol{x})$, otherwise known as wavelet power spectrum contours. In this work, I have adopted Morlet wavelets, $\psi(t/t_s) = \exp(i\omega_\psi t/t_s)\exp\left(|t/t_s|^2 \frac{1}{2}\right)$, where a relatively common non-dimensional frequency has been chosen here, $|\omega_\psi| = 6$, t_s is the wavelet timescale, t is physical time, and i is the imaginary unit.

Figure 3.3 displays the global wavelet power spectrum profiles for the input time series denoted in the figure caption, $\langle E_{\tilde{u}'\tilde{u}'}(\boldsymbol{x},t)\rangle_t f \langle \tilde{u}(\boldsymbol{x})\rangle_t^{-3} h(\boldsymbol{x})$, where $h(\boldsymbol{x})$ is the local dune crest height. Frequency has been shear-normalized for the present purposes, where the ordinate label is equivalent to Strouhal number, $St = fh(\boldsymbol{x})\langle\tilde{u}(\boldsymbol{x})\rangle_t^{-1}$. For high-Reynolds number flows, such as the present, Strouhal number tends toward an asymptotic value, $St \approx 0.25$, which has been denoted by the superposition of a horizontal yellow line on Figure 3.3. For Case $S1_l$ at location $\boldsymbol{x}_L$, there is no distinct peak in any component of velocity. Instead, energy is distributed across constituent frequencies, due to the presence of channel-like turbulence upflow of the large dune (centered around a peak at $fh(\boldsymbol{x})\langle\tilde{u}(\boldsymbol{x})\rangle_t^{-1}$, a characteristic large-eddy timescale). However, the addition of the smaller upflow dune changes the spectral densities significantly. Since $S3'$ and $S4'$ are high-resolution cases, more energy is reasonably contained in higher frequency flow. Moreover, the coincides between $S3'_l$ (dark gray line) and $S3'$ (cyan line), $S4'_l$ (light gray line) and $S4'$ (magenta line) also validates the credibility of LES data.

At $\boldsymbol{x}_L$ (red point in Figure 2.2 (a)), the spectral densities of streamwise velocity fluctuation, indeed, reveal the emergence of a second peak at $fh(\boldsymbol{x})\langle\tilde{u}(\boldsymbol{x})\rangle_t^{-1} \approx 0.25$, which is the signature of vortex shedding from small dune. With the streamwise distance s_x/h decreasing, the energy associated with vortex shedding increases, which is valid in all cases. In contrast, at $\boldsymbol{x}_C$ (green point in Figure 2.2 (a)), all input time series are under the effects of vortex shedding (including Case $S1_l$, because of the periodic boundary condition). Figures 3.3(b) reveals the vortex shedding peak is the dominant energy-containing frequency, although visual inspection of Figure 2.2 shows this to be a logical result given the proximity of $\boldsymbol{x}_C$ to the brinkline of downwind dune.

Figure 3.3 has revealed a distinct energetic peak associated with vortex shedding at $St = fh(\boldsymbol{x})\langle\tilde{u}(\boldsymbol{x})\rangle_t^{-1} = 0.25$, hence, we can return now to Figure 3.2 and the streamwise distances between successive vortex cores. For the purposes of an estimation, we presume that the advective velocity of each vortex core is around $\langle\tilde{u}(\boldsymbol{x})\rangle_t$, which can be related to the distance between successive hairpin vortices via $\langle\tilde{u}(\boldsymbol{x})\rangle_t = \lambda f$. With this, $\langle\tilde{u}(\boldsymbol{x})\rangle_t = \lambda St\langle\tilde{u}(\boldsymbol{x})\rangle_t/h(\boldsymbol{x})$, which can be rearranged to $\lambda = St \cdot h(\boldsymbol{x})$. Put differently, we can normalize by the dune height, yielding $\lambda/h \approx 2$ and $\lambda/h \approx 1$ for the large and small dune, respectively, where h is small dune crest height. Annotations for this spacing have been added to Figure 3.2, conditionally-averaged results and instantaneous results showing reasonable agreement with the vortex core and hairpin vortices observations.

3.4 Sediment Scour

In the last section, hairpin vortex shedding has been studied via instantaneous and conditionally-averaged Q criterion and wavelet decomposition. An interdune vortex roller has been captured through instantaneous 3D vortex visualization (refer Figure 3.2 (d)). In this section, a new fluid statistical analysis is involved for illustration of interdune roller rotation. Meanwhile, surface friction velocity distribution in different cases demonstrates that interdune roller will enhance the asymmetric erosion on large dune. Two complementary parts reveal, consistently and profoundly, the sediment scour of interdune vortex roller and the induced asymmetric erosion. With this, a structural model is presented to summarize the vortex structures, which is how hairpin vortices shed from the upflow dune introduce streamwise vorticity, and how this streamwise vorticity drives asymmetric erosion across the large dune.

Reynolds-averaged helicity is computed as the inner product of velocity and vorticity:

$$H_l = \int_{\mathcal{V}} \langle \tilde{\boldsymbol{\omega}}(\boldsymbol{x}, t) \cdot \tilde{\boldsymbol{u}}(\boldsymbol{x}, t) \rangle_t \mathrm{d}^3\boldsymbol{x}, \tag{3.3}$$

where $\mathrm{d}^3\boldsymbol{x}$, is a control volume over which H_l is to be computed. For the present purposes, it is more convenient to consider differential helicity,

$$h_l(\boldsymbol{x}) = \frac{\mathrm{d}H_l}{\mathrm{d}^3\boldsymbol{x},} = \langle \tilde{\boldsymbol{\omega}}(\boldsymbol{x}, t) \cdot \tilde{\boldsymbol{u}}(\boldsymbol{x}, t) \rangle_t. \tag{3.4}$$

In the absence of coalignment between the velocity and vorticity vectors, helicity vanishes. In the context of the interdune roller, differential helicity (as per Equation 3.4) is interesting

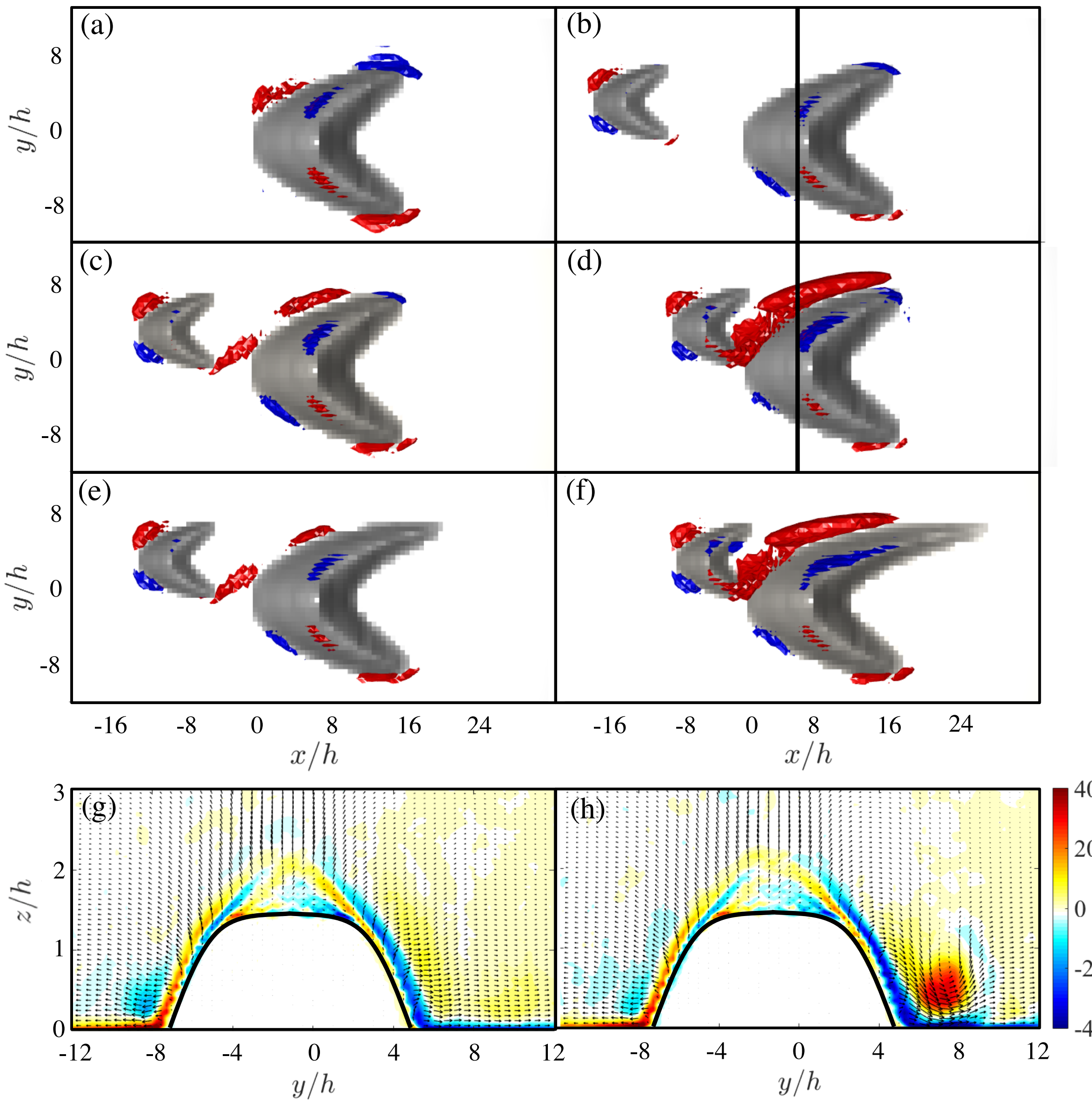

Figure 3.4. Isosurface of Reynolds-averaged, shear-normalized differential helicity, $h(\boldsymbol{x})Hu_*^{-2} = 120$ (red) and $h(\boldsymbol{x})Hu_*^{-2} = -120$ (blue). Panel (a-f) correspond with Case $S1_l$, $S2_l$, $S3_l^{prime}$, $S4_l'$, $S3_l$ and $S4_l$, respectively. Panel (g) and (h) are Reynolds-averaged flow over $S3'$ (g) and $S4'$ (h) in spanwise–wall-normal plane at $x/h = 6.8$, which are showed here as black lines in Panel (b,d). In Panel (g) and (h), contour and vectors are Reynolds-average streamwise vorticity, $\langle\tilde{\omega}_x(\boldsymbol{x})\rangle_t$ and components of in-plane $\{\langle\tilde{v}(\boldsymbol{x},t)\rangle_t, \langle\tilde{w}(\boldsymbol{x},t)\rangle_t\}$.

since it reveals the presence of any accompanying advection. This is relevant to dune morphodynamics, since it implies that the interdune roller scours sediment from the large dune while simultaneously inducing net downflow transport. Figure 3.4 (a-f) exhibit isosurfaces of $h_l(\boldsymbol{x})$ (as per Equation 3.4).

Figure 3.4 shows, apparently, the $h_l(\boldsymbol{x})$ distribution is roughly symmetric for Case $S1_l$. While, as small dune comes, the symmetric pattern is diluted in Case $S2_l$, where s_x/h is maximum. With small dune catching up large dune (Case $S3_l'$, $S4_l'$), the spatial extent of the advecting interdune roller is revealed here by isosurfaces of $h_l(\boldsymbol{x})$. Comparing $S3_l'$ with $S3_l$, $S4_l'$ with $S4_l$, the spatial extents of $h_l(\boldsymbol{x})$ is smaller in $S3_l$ and $S4_l$, which is consistent with preceeding wake veering attenuation (see Figure 3.1). We note, here, that the asymmetry attenuation in wake veering and interdune roller embody the attributes of natural morphodynamics, that is dune morphologic modifications are always trying to weaken the wind loading morphodynamic influence. Since the streamwise extent of differential helicity is actually the product of streamwise vorticity and streamwise velocity, as per $h_l(\boldsymbol{x}) \approx \tilde{\omega}_x(\boldsymbol{x})\tilde{u}(\boldsymbol{x})$, streamwise stretched vortex roller is, actually, the signature for a streamwise vortex roller undergoing the persistent strong advection in the interdune region. Figure 3.4 (g,h) shows spanwise–wall-normal colormap of Reynolds-averaged streamwise vorticity for $S3'$ and $S4'$, respectively (Note that the streamwise transecting locations have been denoted in Panel (b,d)). The consistency between streamwise vorticity and velocity vectors, once again, captures the interdune roller advection in interdune region. However, Figure 3.4 (h) shows the interdune positive streamwise rotating inducing "sediment scour" on inner side face of large dune, associated with flow channeling transporting the sediment downstream, which profoundly advances the proximal dune interaction and enforces the morphodynamic asymmetry.

For completeness, Figure 3.5 has been displayed to reveal three different components of differential helicity at the sampling point within interdune region. The vertical profiles of

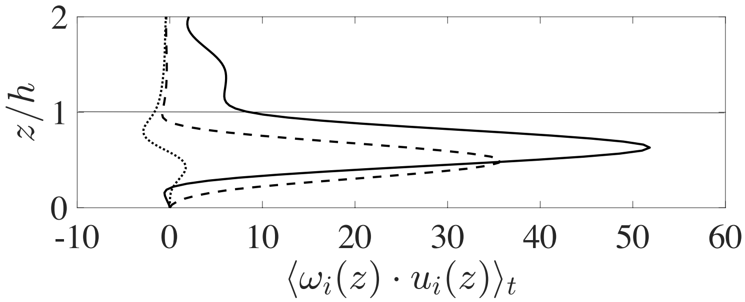

Figure 3.5. The vertical profiles of three terms composing differential helicity in sampling point within interdune region, $\langle \omega_x(z) \cdot u(z) \rangle_t$ (solid line), $\langle \omega_y(z) \cdot v(z) \rangle_t$ (dashed line), $\langle \omega_z(z) \cdot w(z) \rangle_t$ (dotted line), respectively. Horizontal line denotes the wall-normal elevation at small dune height.

three components show strong magnitude heterogeneity beneath small dune height, where $\langle \omega_x(z) \cdot u(z) \rangle_t$ and $\langle \omega_y(z) \cdot v(z) \rangle_t$ show higher magnitudes than $\langle \omega_z(z) \cdot w(z) \rangle_t$. The maximum values of $\langle \omega_x(z) \cdot u(z) \rangle_t$ and $\langle \omega_y(z) \cdot v(z) \rangle_t$ emerges at $z/h = 0.5$, where the interdune roller locates according to Figure 3.4. The dominancy of streamwise component verifies previous relation, $h_l(\boldsymbol{x}) \approx \tilde{\omega}_x(\boldsymbol{x})\tilde{u}(\boldsymbol{x})$. Note that the spanwise component reveals the vorticity roller is tilted by the downwind dune surface, but Section 3.5 indicates vorticity stretching is the crucial sustaining component.

It is of interest to directly verify the aforementioned "scour-and-channeling" saltation mechanism by statistically predicting aerodynamic loading. Recall Section 1.2, the minimum stress required to initiate sediment saltation is defined by threshold friction velocity, $u_{*,t}$, which correlates with various parameters such as sediment spatial size, vegetation density, or soil moisture (Bagnold, 1956; Shao, 2008; Kok et al., 2012). The Bagnold scheme is commonly used to predict $u_{*,t}$:

$$u_{*,t} = A_B \left(\frac{\rho_p}{\rho_a} g D_p \right)^{1/2}, \tag{3.5}$$

where $A_B = A_B(Re_{*,t}) \sim \mathcal{O}(10^{-1})$ is a non-dimensional coefficient related to the particle shear threshold velocity, $Re_{*,t} = u_{*,t} D_p/\nu$, and ρ_p is sediment grain density. If only if

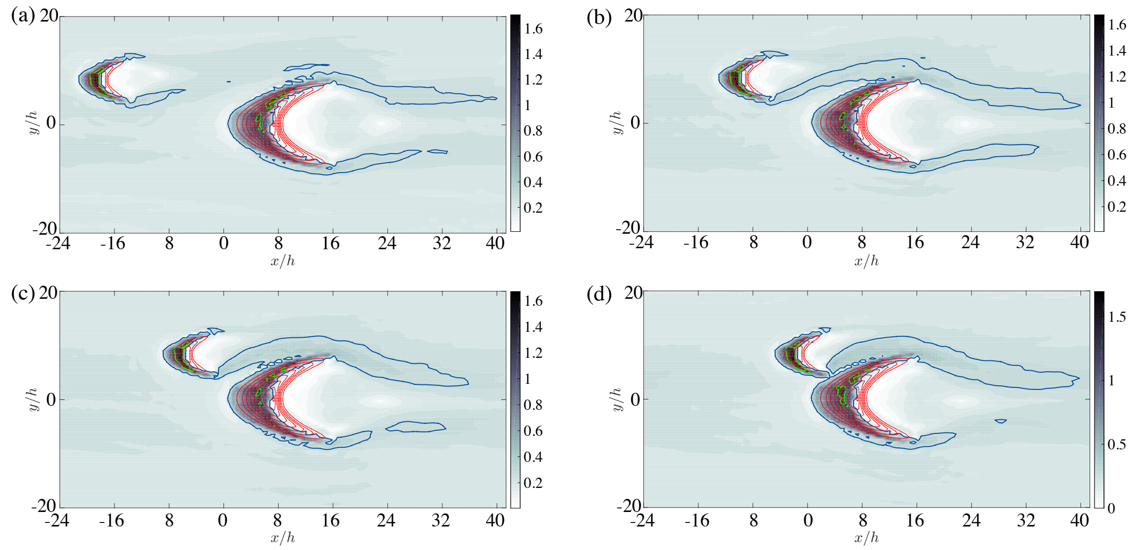

Figure 3.6. Color flood contours of Reynolds-averaged normalized surface stress, $\langle u_*(\boldsymbol{x},t)\rangle_t$, for Case $S1_l$ (a); $S2_l$ (b); $S3'_l$ (c); $S4'_l$ (d), respectively. Included on the color floods are solid blue contours illustrating normalized threshold stress for $D = 180\mu m$ grains as computed with the Bagnold scheme (Equation 3.5). In addition, the solid green contour value, $\langle u_*(\boldsymbol{x},t)\rangle_t = 1.3$, was arbitrarily selected to highlight surface stress asymmetry on the up- and down-flow dune.

the aerodynamic loading satisfy the $u_*(\boldsymbol{x},t)/u_{*,t} > 1$, the corresponded sediments could migrate. Recently, (Kok et al., 2012) has revealed the turbulence effects on the sediment saltation trajectories of mobilized particles. In this work, $u_*(\boldsymbol{x},t)$ is calculated via $u_*(\boldsymbol{x},t) = (\delta_z|\boldsymbol{f}(\boldsymbol{x},t)|)^{1/2}$, where $\boldsymbol{f}(\boldsymbol{x},t)$ is directly retrieved through immersed boundary method (Anderson, 2012).

Figure 3.6 shows Reynolds-averaged surface friction velocity distribution $\langle u_*(\boldsymbol{x},t)\rangle_t$ in Case $S1_l$, $S2_l$, $S3'_l$ and $S4'_l$, respectively. Moreover, the figure includes profiles of threshold surface friction velocity $u_{*,t}$ (solid blue) to estimate the sediment saltating areas (The non-dimensional threshold stress has been marked out for $D = 180\mu m$ sediment grains via Equation 3.5). $\langle u_*(\boldsymbol{x},t)\rangle_t$ contours illustrate elevated surface shear in the interdune channelling zone which is in conformity with the aforementioned asymmetric erosion. Meanwhile, solid green contour lines on the dune surface denote $\langle u_*(\boldsymbol{x},t)\rangle_t = 1.3$, which indicates the

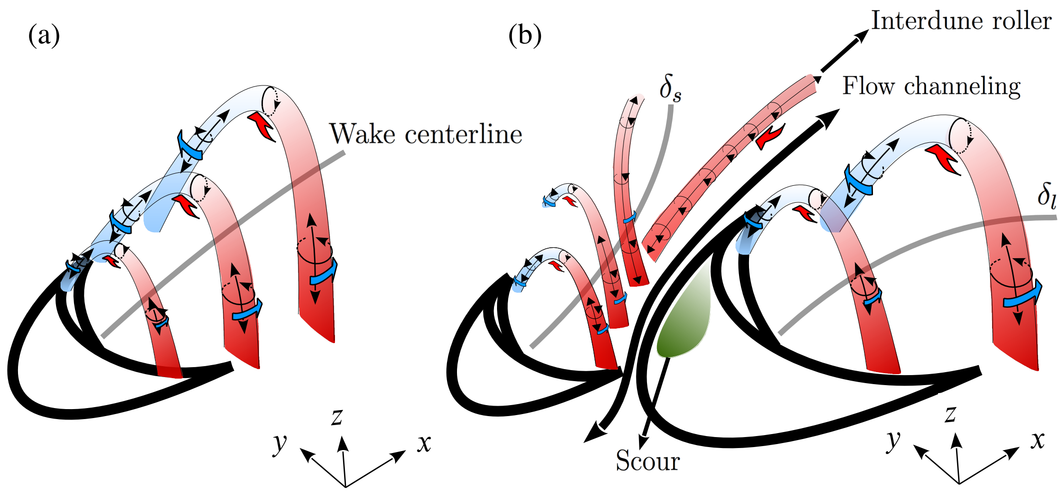

Figure 3.7. Structural model for flow processes associated with dune morphodynamic asymmetry. Panel (a): idealized hairpin vortices shed from dune brinkline; Panel (b): idealized hairpin vortices being simultaneously shed from both dunes, where streamwise vorticity embodied within inner leg of upflow hairpin is stretched by flow channeling (double-headed roller), sustaining the interdune roller and inducing sediment scour on the large dune (green). Red and blue colors denote positive and negative streamwise vorticity directions, respectively. On both panels, gray lines denote dune wake centerline (see Figure 3.1).

largest aerodynamic loading exists on the flow channeling side dune surface. Thus, the surface shear prediction results profoundly validate the preceding "scour-and-channeling" saltation rule.

For the completeness and summary of the current section, Figure 3.7 displays the structural model of "scour-and-channeling" mechanism. Figure 3.7 Panel (a) shows the turbulence structure over a solitary idealized dune, while Panel (b) demonstrates the flow structure in dune collision associated with the sediment erosion pattern. Figure 3.7 (a) shows the hairpin vortex train shed from brinkline, from the preceding results, which happens at $St = 0.25$ (refer Figure 3.3). The hairpin shedding pattern is symmetric and advected along the wake centerline (solid gray line), where the proximal vortex core space is proportional to the corresponding dune crest height, $\lambda \sim max(h(\boldsymbol{x}))$ (refer Figure 3.2). However, the wake centerlines for both dunes are veered surrounding flow channelling region (refer Figure 3.1) in two dune proximal interaction model in Figure 3.7 (b), where the monotonic heterogeneity of wake veering is correlated to s_x/h. The hairpin shedding still gets triggered by both dunes, however, small dune hairpin vortices will evolve to interdune roller under the enhanced advection by flow channeling, where continuous positive streamwise rotation has been denoted by red vector (refer Figure 3.4). Sediment scour is initiated by the interdune roller (green zone in Panel (b)). High speed mass and momentum flux in flow channeling provides strong sediment saltation advection, advancing further asymmetric erosion on downwind dune (refer Figure 3.6).

So far, the highlighting "scour-and-channeling" effect has been elaborately expatiated via efficient numerical simulation results with structural model, wherein the arguments – interdune roller can trigger sediment scour on large dune, and that this is foremost in setting the dune morphology as interaction advances – has been comprehensively testified in this section. For the closure of this argument, the following section will present results of streamwise vorticity budget in the interior and outside of the flow channeling region. Indeed, the results indicate the stretching of ambient streamwise vorticity will surely provide the largest gain to interdune streamwise vorticity.

3.5 Turbulent Vorticity Dynamics

To understand interdune vorticity, the Reynolds-averaged velocity and total stresses are adopted here for the elucidation of mechanisms responsible for sustaining the interdune roller. Firstly, the Reynolds-averaged incompressible momentum transport equation has been considered:

$$\frac{1}{2}\nabla\left(\langle\tilde{\boldsymbol{u}}\rangle_t\cdot\langle\tilde{\boldsymbol{u}}\rangle_t\right)-\langle\tilde{\boldsymbol{u}}\rangle_t\times\langle\tilde{\boldsymbol{\omega}}\rangle_t=-\frac{1}{\rho}\nabla\tilde{p}-\nabla\cdot\langle\mathsf{T}\rangle_t+\boldsymbol{\Pi}+\frac{1}{\rho}\boldsymbol{f},\tag{3.6}$$

where $\mathsf{T}=\langle\boldsymbol{u}'\otimes\boldsymbol{u}'\rangle_t=\langle\tilde{\boldsymbol{u}}'\otimes\tilde{\boldsymbol{u}}'\rangle_t+\langle\boldsymbol{\tau}\rangle_t$, here the first and second right-hand side terms are the resolved and subgrid-scale stress tensor (this additive approach is necessary when

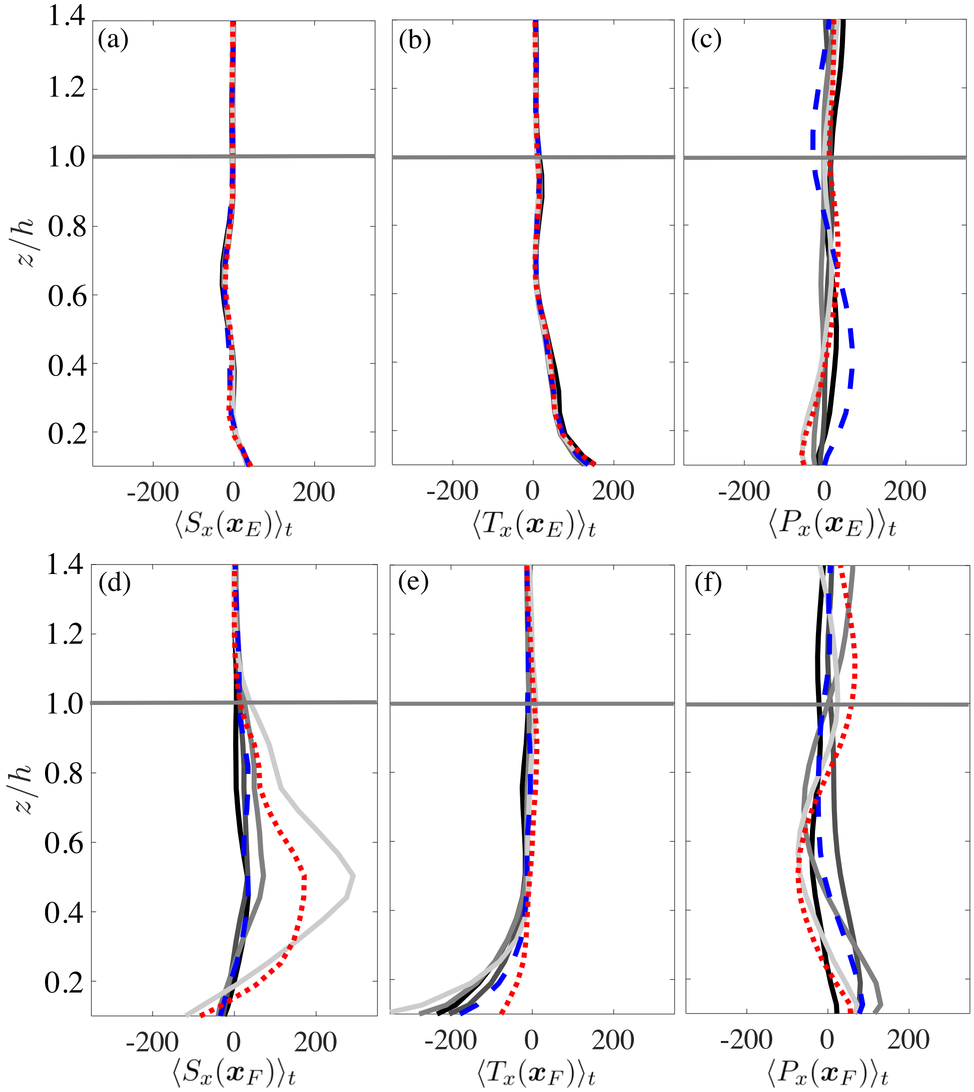

Figure 3.8. Vertical profiles of constituent right-hand side terms from Reynolds-averaged streamwise vorticity transport Equation (Equation 3.8), including vortex stretching $\langle S_x\rangle_t$ (a,d), vortex tilting $\langle T_x\rangle_t$ (b,e) and turbulent torque $\langle P_x\rangle_t$ (c,f) at discrete streamwise-spanwise locations collocated with Point $\boldsymbol{x}_E$ (a, b, c) and Point $\boldsymbol{x}_F$ (d, e, f) (see also Figure 2.2 (a)). Black, dark gray, gray, and light gray lines correspond with Case $S1_l$, $S2_l$, $S3'_l$, and $S4'_l$, respectively, while dashed blue and dotted red lines correspond with $S3_l$ and $S4_l$, respectively. Horizontal gray line denotes small dune height.

assembling the total stresses from LES datasets *a posteriori*); $\boldsymbol{f}$ represents imposed forces associated with the presence of solid obstacles via an immersed boundary method, while $\boldsymbol{\Pi}$ denotes any ambient pressure-gradient forcing. The transport equation for $\langle\tilde{\boldsymbol{\omega}}\rangle_t$ is derived via the curl of Equation 3.6, yielding:

$$\underbrace{\langle\tilde{\boldsymbol{u}}\rangle_t \cdot \nabla\langle\tilde{\boldsymbol{\omega}}\rangle_t}_{\text{Advection}} = \underbrace{\langle\tilde{\boldsymbol{\omega}}\rangle_t \cdot \nabla\langle\tilde{\boldsymbol{u}}\rangle_t}_{\text{Stretching and Tilting}} - \underbrace{\nabla \times \nabla \cdot \langle\mathsf{T}\rangle_t}_{\text{Turbulent torque}}, \tag{3.7}$$

where annotations have been used to denote the stretching and tilting of $\langle\tilde{\boldsymbol{\omega}}\rangle_t$ via mean-flow gradients, and gains/losses to $\langle\tilde{\boldsymbol{\omega}}\rangle_t$ via spatial heterogeneity of T (so called turbulent torque). The former and latter are also referred to as Prandtl's secondary flow of the first and second kind (Perkins, 1970; Bradshaw, 1987), respectively. In the preceding sections, "scour-and-channeling" effect at interdune region is illustrated. Thus, in this section, we will consider only the streamwise component of Equation 3.7:

$$\underbrace{\langle\tilde{\boldsymbol{u}}\rangle_t \cdot \nabla\langle\tilde{\omega}_x\rangle_t}_{\text{Advection}} = \underbrace{\langle\tilde{\omega}_x\rangle_t \partial_x \langle\tilde{u}\rangle_t}_{\text{Stretching, } \langle S_x(\boldsymbol{x})\rangle_t} + \underbrace{\langle\tilde{\omega}_y\rangle_t \partial_y \langle\tilde{u}\rangle_t + \langle\tilde{\omega}_z\rangle_t \partial_z \langle\tilde{u}\rangle_t}_{\text{Tilting, } \langle T_x(\boldsymbol{x})\rangle_t} - \underbrace{\epsilon_{xqi}\partial_q\partial_j\langle\mathsf{T}_{ij}\rangle_t}_{\text{Turbulent torque, } \langle P_x(\boldsymbol{x})\rangle_t} . \tag{3.8}$$

The symbolic annotations beneath each term in Equation 3.8 will be used later to explain mechanisms driving gains and losses to $\langle\tilde{\omega}_x\rangle_t$. It is apparent, from inspection, that the first right-hand side term corresponds with stretching of $\langle\tilde{\omega}_x\rangle_t$, while the second right-hand side term corresponds with tilting of $\langle\tilde{\omega}_y\rangle_t$ and $\langle\tilde{\omega}_z\rangle_t$ into the streamwise direction (note that the sum of these terms was referred to as $\langle P_x(\boldsymbol{x})\rangle_t$ by Perkins (Perkins, 1970)).

Figure 3.8 shows the vertical profiles of vorticity stretching $\langle S_x(\boldsymbol{x})\rangle_t$, tilting $\langle T_x(\boldsymbol{x})\rangle_t$, turbulent torque $\langle P_x(\boldsymbol{x})\rangle_t$, at locations $\boldsymbol{x}_E$ and $\boldsymbol{x}_F$, respectively. Figure 2.2 (a) has shown the discrete locations of $\boldsymbol{x}_E$ (gray point) and $\boldsymbol{x}_F$ (black point), respectively, where $\boldsymbol{x}_E$ is outside of the interdune zone, while, $\boldsymbol{x}_F$ is outside of that. Figure 3.8 (a-c) are profiles at location $\boldsymbol{x}_E$, (d-f) are profiles at location $\boldsymbol{x}_F$, respectively. Thus, the differences between the profiles on the two aforementioned locations are able to contribute to asymmetries associated with the channeling flow. At location $\boldsymbol{x}_E$, Figures 3.8 (a-c) shows that three terms profiles exhibit no dramatic differences in different cases, wherein turbulent torque $\langle P_x(\boldsymbol{x}_E)\rangle_t$ makes the dominant contribution to budgeting of Reynolds-averaged streamwise vorticity. However, comparatively vorticity stretching $\langle S_x(\boldsymbol{x}_E)\rangle_t$ and tilting $\langle T_x(\boldsymbol{x}_E)\rangle_t$ make a modest contribution. The profiles at location $\boldsymbol{x}_F$ exhibit dramatical changes in a special trend at different cases which could help to sustain the interdune roller evolving and channeling flow.

Figure 3.8 (d-f) show the three right hand side terms in Equation 3.8 at location $\boldsymbol{x}_F$. Obviously, the upcoming small dune changes the channeling flow critically. Comparing with the terms at location $\boldsymbol{x}_E$, the magnitude of all terms at $\boldsymbol{x}_F$ are bigger, associated with a heterogeneity beneath the small dune height (gray line in Figure 3.8). $\langle S_x(\boldsymbol{x}_F)\rangle_t$ displays a increasing trend as small dune gets closer to big dune, the maximum values of which are all on the elevation at $z/h \approx 0.5$, that is the interdune roller height (refer Figure 3.4). Consistently, $\langle S_x(\boldsymbol{x}_F)\rangle_t$ makes the dominant contribution in $S4_l$ (dotted red line) and $S4'_l$ (light gray line), where largest interdune vortex roller exists in the flow channeling region. This indicates that the vorticity stretching term in channeling flow sustains the streamwise vorticity. The magnitude of turbulent torque at $\boldsymbol{x}_F$ exceeds the magnitudes at $\boldsymbol{x}_E$, which, however, is still smaller than the contribution of vorticity stretching.

For completeness, the color flood contour of Reynolds-averaged vortex stretching term is displayed in Figure 3.9: the horizontal plane at elevation $z/h = 0.5$, which is the height of interdune roller, associated with low-pass filtered wake centerline at leeward. For the isolated case, the magnitude of the stretching term is equal and opposite on the dune stoss face without wake veering. As small dune gets closer to the large dune, the monotonic enhancement of vortex stretching is captured at the flow channeling region as s_x/h decreases, which consistently indicate same results with vertical profiles in Figure 3.8.

In the current chapter, monotonically heterogeneous changes of dune wake have been found due to enhancement of "flow channeling" as small dune approaches large dune "toe". "Wake veering" captures the momentum flux controlled upcoming dune wake centerlines.

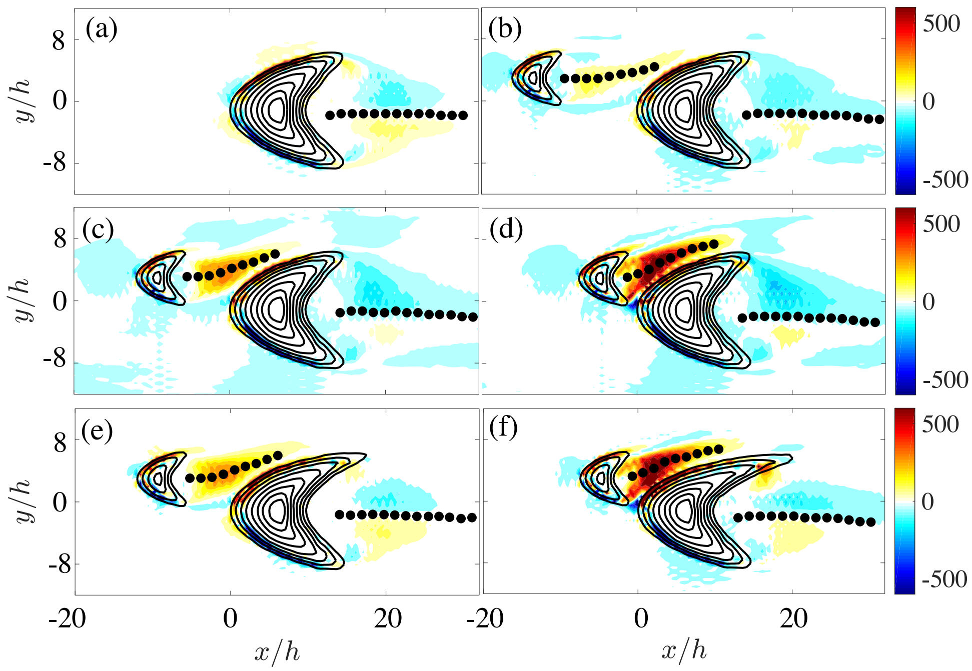

Figure 3.9. Color flood contour of Reynolds-averaged term responsible for stretching of streamwise vorticity, $\langle S_x \rangle_t(x, y, z/h = 0.5)$ (Equation 3.8). Panel (a-f) corresponds with Case $S1_l$, $S2_l$, $S3'_l$, $S4'_l$, $S3_l$, $S4_l$, respectively. Included on the color floods are low-pass filtered data points for the wake centerline, emanating from the small and large dunes, $\delta_s(x_s; z/h = 0.5)$ and $\delta_l(x_l; z/h = 0.5)$, respectively.

Three-dimensional visualizations provide evident vortex shedding at $St = 0.25$, where streamwise distance between successive vortex cores correlated with local dune crest height. An interdune roller persistently keeps positively streamwise rotating, associated with enhanced sediment erosion within interdune region. The right hand side terms of Reynolds-average streamwise vorticity transport equation have been analyzed for the gains and losses in interdune channeling flow. Two discrete sampling points have been chosen for comparison. The point locating outside flow channeling exhibits rare dramatic changes in different dune configurations, whereas, the profiles inside the interdune region are showing evident heterogeneity beneath small dune peak, which is correlated to streamwise offset spacing. Large magnitudes of vorticity stretching at elevation of interdune roller indicates its dominant contribution to sustain streamwise vortex roller.

CHAPTER 4

DUNE-FIELD COHERENT STRUCTURE GENESIS

In preceding sections, turbulence coherent structures, stimulated by dune feature, have been shown to scour sediments within interdune regions. This section consists of high-fidelity visualization of DFSL flow in idealized and realistic dune field. This section starts from the consideration of flow aloft idealized dune arrangements, for simplicity and the capability to isolate the salient turbulent flow mixing, and then move on to the study of realistic dune field in the White Sands National Monument (see Figure 2.2 for WSNM DEM). For such purpose, Reynolds-averaged flow, $\langle \tilde{\boldsymbol{u}}(\boldsymbol{x}) \rangle_t$, derived from precursor simulation, is used to initiate the simulation, $\tilde{\boldsymbol{u}}(\boldsymbol{x}, t=0) = \langle \tilde{\boldsymbol{u}}(\boldsymbol{x}) \rangle_t$. Such method has been adopted, recently, by (Bailey and Stoll, 2016) to study the mixing layer evolve over vegetative canopies. The mixing layer-like process has been observed via such method which confirms that DFSL falls within the broad scope of obstructed shear flows (Ghisalberti, 2009). Comparing with vegetative canopy, the merely difference is the streamwise interdune roller, observed in Chapter 3, inducing asymmetric erosion among proximal dunes. For completeness, this section concludes with presentation of a structural model, which summarizes the highlighting schematics. [1]

Herein, the spatial transects of turbulent kinetic energy $k(\boldsymbol{x})$ is presented:

$$k(\boldsymbol{x}) = \frac{1}{2}(\boldsymbol{u}' \cdot \boldsymbol{u}') = \frac{1}{2}(\tilde{u}'(\boldsymbol{x})^2 + \tilde{v}'(\boldsymbol{x})^2 + \tilde{w}'(\boldsymbol{x})^2). \tag{4.1}$$

Meanwhile, for the purpose of 3D visualization, instantaneous Q criterion is used as flow identifier to show the shear layer evolving in DFSL.

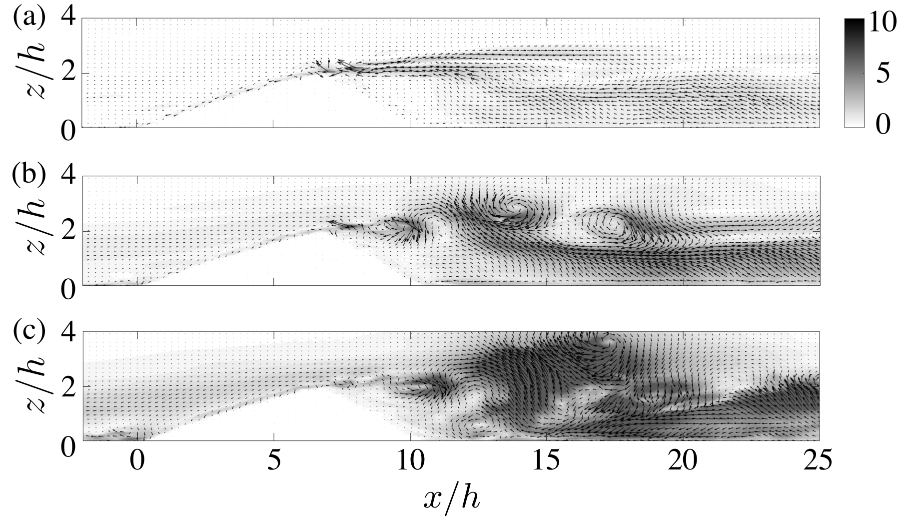

Figure 4.1. Streamwise–wall-normal transect visualization of instantaneous flow over Case $S1$ at different times: (a)$tU_0\delta^{-1} = 0.31$, (b)$tU_0\delta^{-1} = 1.08$, and $tU_0\delta^{-1} = 2.62$, where $tU_0\delta^{-1}$ is shear-normalized time, or number of large-eddy turnovers. Visualization shown at spanwise position, $y/h = 0$ (see Figure 2.2 Panel (a)). Contours are turbulent kinetic energy, $k(x, y/h = 0, z, t)$, and instantaneous fluctuating velocity, $\{\tilde{u}'(x, y/h = 0, z, t)/u_*, \tilde{w}'(x, y/h = 0, z, t)/u_*\}$.

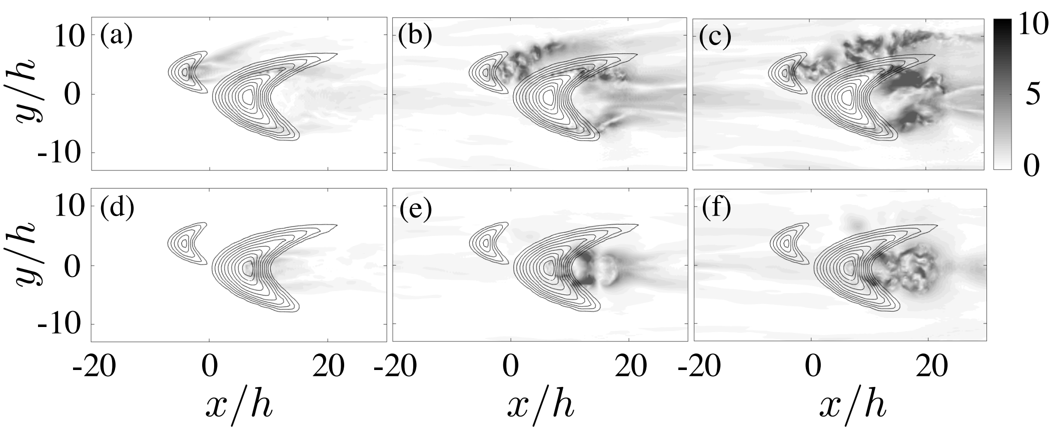

Figure 4.2. Streamwise–spanwise visualization of of instantaneous flow over Case $S4$ at different times: (a,d)$tU_0\delta^{-1} = 0.30$, (b,e)$tU_0\delta^{-1} = 1.05$, and (c,f) $tU_0\delta^{-1} = 1.80$, where $tU_0\delta^{-1}$ is shear-normalized time, or number of large-eddy turnovers. Visualization shown at different wall-normal elevations: (a-c) $z/h = 1.00$ (height of small dune) and (d-f) $z/h = 2.00$ (height of large dune). Contour is turbulent kinetic energy $k(\boldsymbol{x}, t)$.

4.1 Idealized Case

Figure 4.1 shows streamwise–wall-normal transects of instantaneous $k(\boldsymbol{x})$ over high-resolution case $S1$ at central spanwise transect $y/h = 0$ with velocity fluctuation vectors, $\{\tilde{u}'(x, y/h = 0, z, t)/u_*, \tilde{w}'(x, y/h = 0, z, t)/u_*\}$ superimposed on color contour (refer Figure 2.2 to see the topography information). The 2D visualization of solitary dune quantifies how the presence of proximal dunes perturbs flow field and induces the spatial asymmetry seen in nature. Figure 4.1 is composed of a time series of $k(\boldsymbol{x})$ evolving colormaps. Panel (a) shows the turbulent kinetic energy at early stage, $tU_0\delta^{-1} = 0.31$, where shear layer emanated from dune brinkline containing strong flow fluctuation. Generally, the key feature is elevated sheets of high-k flow in the downstream region, $0 \lesssim x/h \lesssim 20$ and $\lesssim z/h \lesssim 4$, which corresponds with mixing-layer type of shear. At advance stages, Panel (b) $tU_0\delta^{-1} = 1.08$, the Kelvin–Helmholtz instability induced vortex shedding eddies has been revealed at $x/h = 10, 13, 17$. At later stages Panel (c) $tU_0\delta^{-1} = 1.80$, the magnitude of kinetic energy is elevated, due to stronger flow fluctuating in shear layer. In fact, the shed eddies in leeward is the signature of hairpin vortex heads – vortical motions dominated by spanwise vorticity, the thickness and eddy length scales of which will grow in downstream. No asymmetric properties in the wake should be displayed in $x - z$ plane over Case $S1$. However, the turbulent kinetic energy distribution over Case $S4$ displays asymmetric turbulence evolving process in Figure 4.2.

Figure 4.2 shows visualization of instantaneous $k(\boldsymbol{x})$ in the streamwise-spanwise plane, at a series of shear-normalized times. In Figure 4.2, panels are shown for temporal increase from lefts to right panels, and wall-normal elevation increase from top to bottom panels. At the early stages (a,d), the magnitude of $k(\boldsymbol{x})$ is less than 5, which is even lower at higher elevation in Panel (d), since more turbulent mixing is stimulated near wall. The distribution of

[1]This chapter is based on the journal paper: Wang C, Anderson W. Turbulence Coherence Within Canonical and Realistic Aeolian Dune-Field Roughness Sublayers[J]. *Boundary-Layer Meteorology*, 2019: 1-26.

k has not been homogenized by coherent vortical process, which attenuates spatial coherence in wake. The wake veering of small and big dune is captured at $z/h = 1.00$ and $z/h = 2.00$, respectively (see Figure 3.1 for wake veering profiles). Obviously, k is much larger in interdune region, because flow fluctuation is more vigorous in flow channeling (remind PDF profiles in Figure 3.2). With time increasing, smaller turbulence length scales get developed to form swirling motion associated with higher magnitude fluctuating in leeward face. A train of eddies have been captured in (b) $0 \lesssim z/h \lesssim 10$, which are the signature of hairpin vortex shedding. In Panel (c,f), the preceding swirling eddies shed from brinkline in (b,e), are homogenized into mixed smaller length scale streaks, containing high turbulent kinetic energy, $\max(k) \gtrsim 10$. The temporal evolving progress of k in $x - z$ plane favorably recovers turbulence genesis in dune interaction. In consistency, k evolving distribution displays asymmetric pattern, aroused by flow channeling enhancement – the key difference to obstructed shear flows due to homogeneous canopies (particularly vegetative canopies). Recently, “Boil” has found to be a reason inducing large mass and momentum flux near bedform, which, in fact, is a small length scale turbulent ejecting event near ground (Omidyeganeh and Piomelli, 2011b). Panel (c) has captured the areas where “Boil” could easily get aroused (refer Figure A.1, where the yellow square denotes the Boil structure observed experimentally in flow channeling region).

For further outline the key differences of DFSL, Figure 4.3 shows isosurfaces of instantaneous Q criterion (Equation 3.2) in Case $S2$ (a,d), $S3$ (b,e) and $S4$ (c,f) at different times (Panel (a-c) at early time; Panel (d-f) at later time). At early time, integrated vortex rollers surround dune surface enveloped in shear layer and interdune region. Streamwise vortex roller sustained by $S(\boldsymbol{x}, t)$ (Equation 3.8) is profoundly affected by decreasing s_x/h, herein streamwise roller is stretched by interdune channeling flow associated with increasing lateral spatial extents. At later time, integrated vortex rollers break down into aggregations of head-up hairpin vortices and multiple streamwise rollers, which is also recently observed

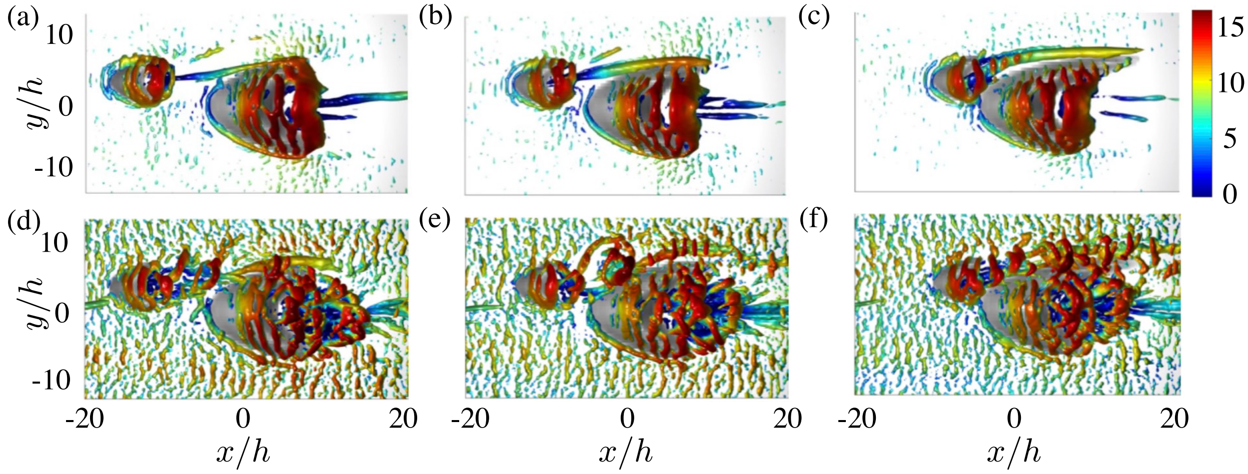

Figure 4.3. Streamwise-spanwise visualization of isosurface of instantaneous Q criterion for $Q = 20$ signed by instantaneous streamwise velocity $\tilde{u}(\boldsymbol{x})/u_*$ of Case $S2$ (a,d), $S3$ (b,e) and $S4$ (c,f) respectively at different times: (a,b,c) $tU_0\delta^{-1} = 0.75$, and (e,f,g) $tU_0\delta^{-1} = 2.25$.

in vegetative canopies (Bailey and Stoll, 2016). Meanwhile, spanwise roller wrapped on brinkline provide creation of leeward vortex shedding. It is not hard to find that hairpin vortices genesis has already been evolved in interdune vortex roller at early time in Panel (c) $-5 \lesssim x/h \lesssim 0$. This structure represents a key departure from obstructed shear flow processes. In next section, I will show a similar structure emerges in flow over realistic dune field, but visual coherence is confounded by the complexity of natural system. The implications of this structure for quantifying underlying similarity of DFSL turbulence is explored in Chapter 5.

Figure 4.4 shows the characteristic attributes of interdune roller turbulence from instantaneous data. Panel (a) shows instantaneous Q criterion in fully developed turbulent flow, where an evident interdune roller is marked by red circle. The red point denotes the quadrant analysis location near the ground, $z/h = 0.03$. Panel (b) shows the Reynolds-averaged initiated flow at $tU_0\delta^{-1} = 2.62$ in $S4$. From the x-z section in Panel (b), the fluctuating turbulent swirling process is agitated in interdune region, associated with enhanced turbulent events. Panel (c-f) reveal the quadrant analysis of the point in Panel (a), from that we can draw the

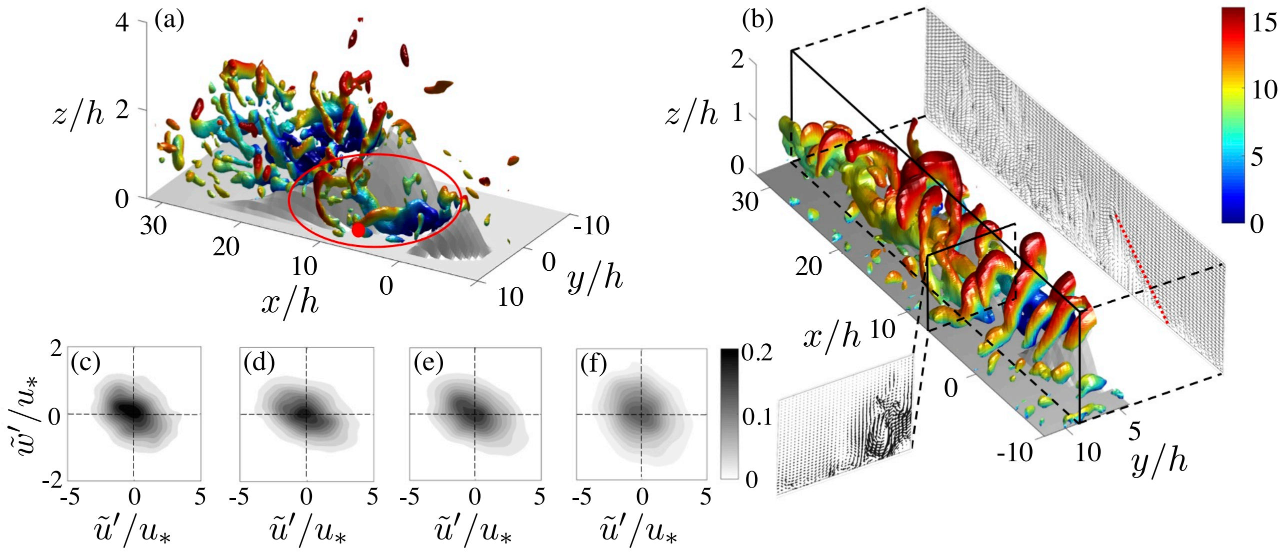

Figure 4.4. Panel (a) shows instantaneous Q-criterion($Q = 100$) of $S4$ in fully developed turbulent flow condition (red ellipse denotes the interdune roller, red point to show the quadrant analysis position). Panel (b) shows instantaneous Q-criterion($Q = 30$) of $S4$ at $tU_0\delta^{-1} = 2.62$ with instantaneous streamwise–wall-normal velocity fluctuation $\{\tilde{u}(x, y/h = 4.8, z)/u_*, \tilde{w}(x, y/h = 4.8, z)/u_*\}$ in x-z plane, and instantaneous spanwise–wall-normal $\{\tilde{v}(x/h = 7.5, y, z)/u_*, \tilde{w}(x/h = 7.5, y, z)/u_*\}$ quivers in the interdune region; Panel (c-f) show quadrant analysis at the red point position in Panel (a) at $S1 - S4$ respectively. The elevation of red point is at $z/h = 0.03$.

following conclusions: *(i)* turbulent ejection ($Q2$) and turbulent sweep ($Q4$) are dominant turbulent events in interdune region; *(ii)* as s_x/h decreases, increasing velocity fluctuation magnitudes indicate the consistency of PDF profiles in Figure 3.2 (a). The enhancement of fluctuating magnitude could induce stronger momentum and mass transport flux in some special turbulent structures such as “Boil”.

The turbulent event – “Boil” has been captured in Figure 4.5, which displayed two kinds of Boils respectively. Panel (a,b) show the Boil event in inertial layer; Panel (c,d) show the Boil event close to wall, $z/h = 0.03$. In Panel (b,d), turbulent kinetic energy $k(\boldsymbol{x})$ is displayed associated with velocity fluctuation $\{\tilde{u}'(\boldsymbol{x})/u_*, \tilde{v}'(\boldsymbol{x})/u_*\}$ at same elevations. The existence of head-up hairpin has been captured in inertial layer which is generated from the leeward of

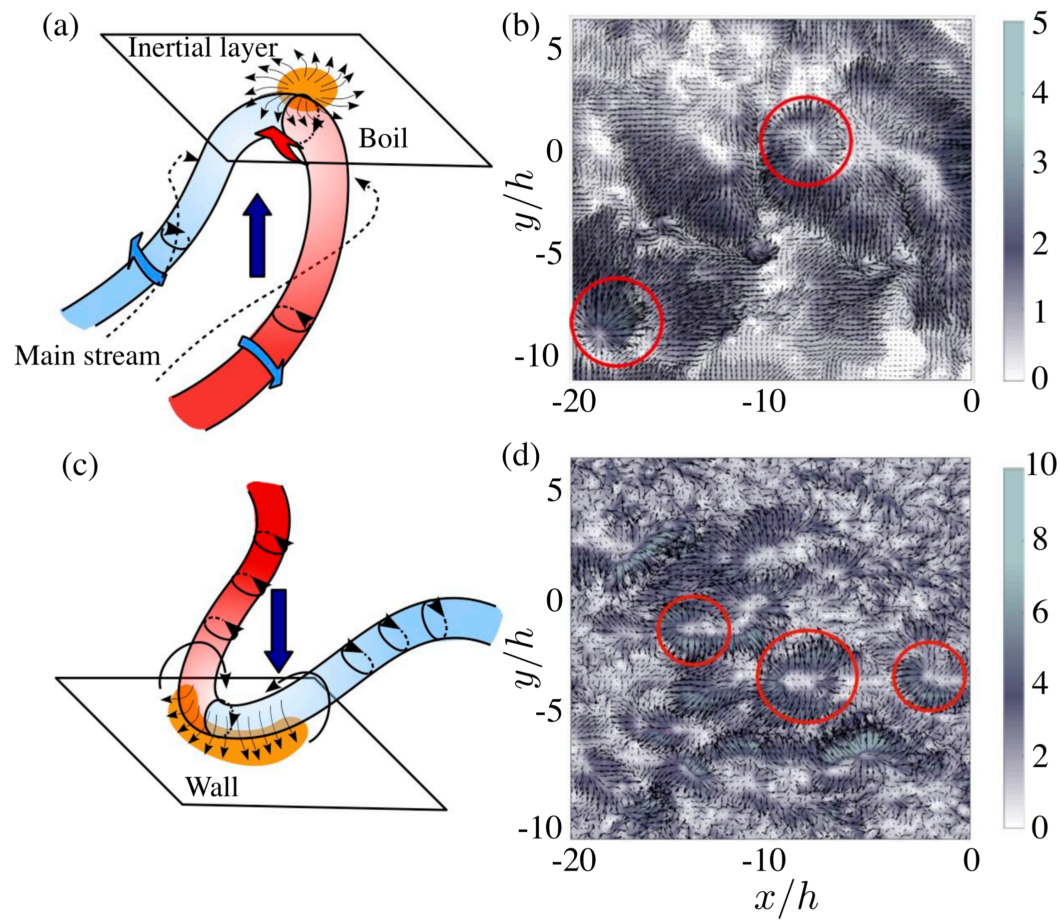

Figure 4.5. “Boil” events in ideal cases: Panel (a) shows schematic of “Boil” event at in inertial layer; Penal (b) shows $k(\boldsymbol{x})$ and streamwise and spanwise velocity fluctuation $\{\tilde{u}'(\boldsymbol{x})/u_*, \tilde{v}'(\boldsymbol{x})/u_*\}$ within inertial layer in Case $S1$; Panel (c) shows schematic of “Boil” event on the wall; Panel (d) shows $k(\boldsymbol{x})$ and streamwise velocity fluctuation $\tilde{u}'/u_*$ and spanwise velocity fluctuation $\tilde{v}'/u_*$ at the $z/h = 0.03$ in Case $S1$. Orange zones denote the “Boil” events. Blue quiver denotes low-momentum flux.

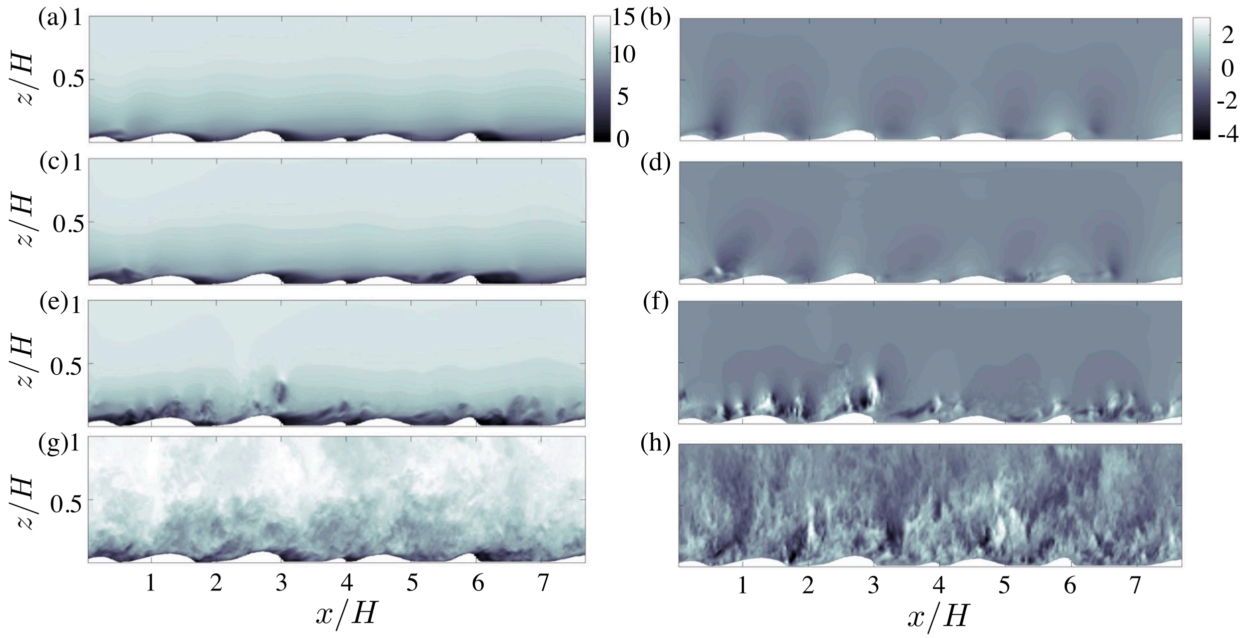

Figure 4.6. Color flood contour of instantaneous streamwise velocity $\tilde{u}(x, y/H = 3.84, z)/u_*$ (a,c,e,g) and wall-normal velocity $\tilde{w}(x, y/H = 3.84, z)/u_*$ (b,d,f,h) at central spanwise position, $y/H = 3.84$ (Figure 2.2 (b)) at different times: $tU_0\delta^{-1} = 1.22$ (a,b), $tU_0\delta^{-1} = 2.44$ (c,d), $tU_0\delta^{-1} = 4.88$ (e,f) and fully turbulent condition (g,h) respectively. Simulation results are from Case WSNM2 (Table 2.1 provides comprehensive simulation details).

big dune, advecting upwards by upcoming flow. While, head-down hairpin emerges close to ground. Previously, (Omidyeganeh and Piomelli, 2011a) has displayed the evolving progress of a large head-up hairpin vortex touching the surface, generating turbulent “Boil”. They elucidates the significant transport of momentum and mass in such structure. This finding highlights significance of the turbulence structure attributes in DFSL, where the turbulent eddies can profoundly affect the morphodynamic progress at different levels. In Chapter 5, the turbulence spatial attributes will be comprehensively exhibited in idealized and realistic dune fields respectively.

4.2 Realistic Case

Figure 4.6 presents streamwise–wall-normal transects of the temporal evolution of $\tilde{u}(\boldsymbol{x}, t)$ (a,c,e,g) and $\tilde{w}(\boldsymbol{x}, t)$ (b,d,f,h), but for the WSNM DEM (see Figure 2.2 (b)) at $y/h = 3.84$. The Reynolds-averaged flow was derived from precursor simulations, and is used as the initial condition in new simulations, which indeed facilitates qualitative interpretation on the evolution of turbulent structures (eg. Figures 4.1, 4.2. 4.3). The established Reynolds-averaged flow patterns quickly collapse and effectively vanish by $tU_0\delta^{-1} = 4.88$, especially in close proximity to the dunes ($z/h \lesssim 4$, consistent with preceding prognostic estimates for DFSL thickness). In inertial layer $z/h \gtrsim 4$, resemblance of Reynolds-averaged flow pattern still remains at $tU_0\delta^{-1} = 4.88$, however, for the fully turbulent boundary layer, turbulent mixing should engulf whole domain. Moreover, Figure 4.6 also reveals the inclined, coherent features within the inertial layer, $0.3 \lesssim z/H \lesssim 1$, but these are the signatures of coherent atmospheric motions within inertial layer.

Figure 4.6 has shown the DFSL emergence at dune proximity, but the large spatial extents undermine the observations and comparison with idealized dune flow. For a clear comparison with 3D flow visualization over idealized cases, isosurfaces of Q criterion over Box 1 to Box 4 topographies within WSNM (see Figure 2.2 (b) for Box 1 to Box 4 spatial informations) have been showed in Figure 4.7. In Figure 4.7, from left column to right column is $tU_0\delta^{-1} = 1.22$ (a,d,g,j), $tU_0\delta^{-1} = 2.44$ (b,e,h,k), $tU_0\delta^{-1} = 3.66$ (c,f,i,l), respectively; from top row to bottom row is Box 1 to Box 4 respectively. A great consistence with idealized dune flow has been revealed in Box 1 and Box 2, which corresponds to leeward vortex shedding and interdune streamwise roller. However, due to the complexity of natural dune field, Box 3 and 4 exhibit some exceptions in WSNM. Panel (g-i) present multiple hairpin vortices shed from a solitary dune brinkline, which is due to the elongated and inter tangled meandering brinkline in WSNM. While Panel (j-l) present the coupling process between two counter rotating interdune rollers, generating a train of hairpin vortices in flow channeling.

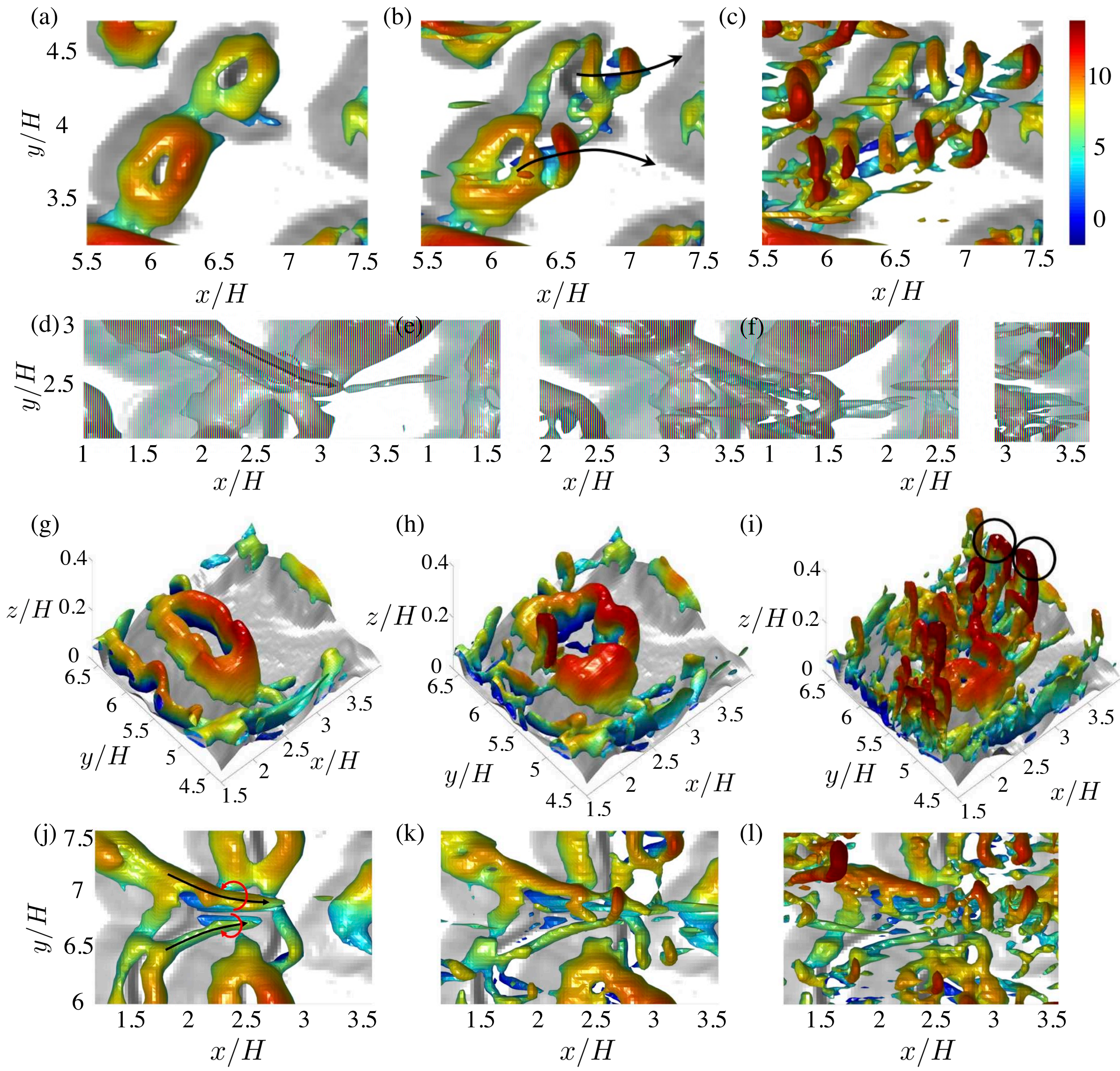

Figure 4.7. Isosurface of instantaneous Q criterion $Q = 100$ signed by instantaneous streamwise velocity, $\tilde{u}(\boldsymbol{x}, t)/u_*$, for LES of flow over Case WSNM2 (Table 2.1) at times: $tU_0\delta^{-1} = 1.22$ (a,d,g,j), $tU_0\delta^{-1} = 2.44$ (b,e,h,k), $tU_0\delta^{-1} = 3.66$ (c,f,i,l) in Box 1 (a-c), Box 2 (d-f), Box 3 (g-i), and Box 4 (j-l). See Figure 2.2 (b) for topography visualization. Black quivers denote hairpin vortex shedding directions in Panel (b). Black circles denote multiple hairpin vortices in dune leeward.

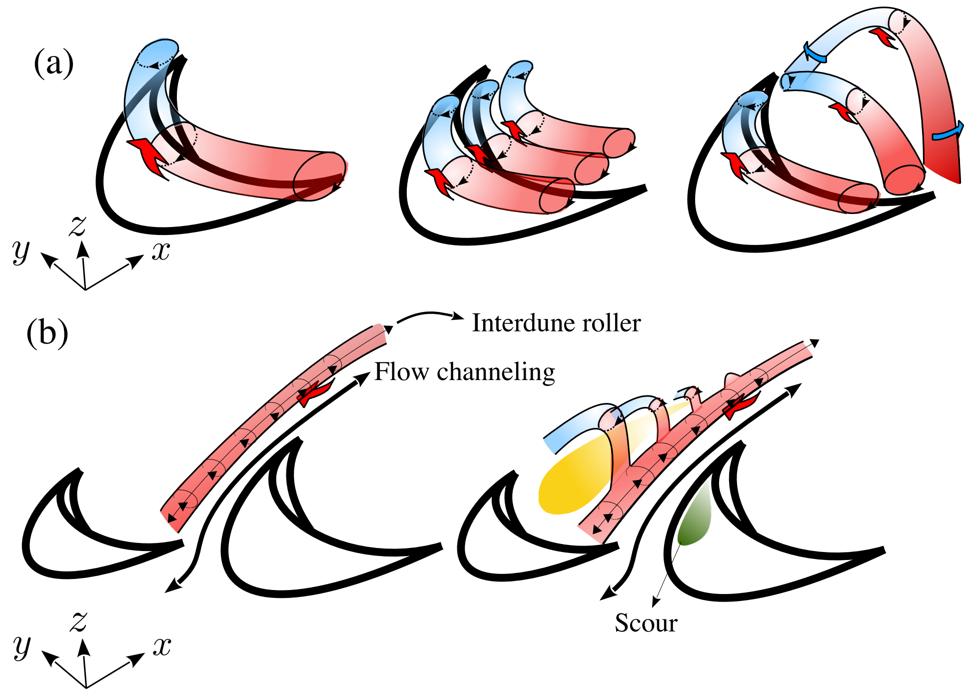

Figure 4.8. Conceptual schematic drawing of coherent structure genesis over a solitary idealized dune (a) and two interacting idealized dunes (b). On Panel (a), vortex shedding and the Kelvin–Helmholtz instability initiate large spanwise vortex rollers along the dune brinkline. With turbulence increasing, large spanwise vortex rollers will break down into a train of self-similar spanwise rollers. Under the effects of vortex tilting and stretching, spanwise rollers become hairpin vortices. On Panel (b), streamwise vortex roller gets sustained by the interdune vortex stretching in flow channeling. Large streamwise roller collapses into smaller scale streamwise vortex rollers which provide positive streamwise vortices to generate hairpin legs in the small dune wake. Green area denotes the enhanced sediment erosion because of interdune roller scouring event. Yellow area denotes the increasing turbulent events when upcoming dune interacting big dune. Red and blue colors denote positive and negative streamwise vorticity directions, respectively.

But these exceptions will not dilute the consistency in both cases, because the coherent structures in Box 3 and Box 4 can be treated as coextensive turbulence progresses.

With preceding 3D visualization of coherent structures, the interaction between inertial sublayer and roughness sublayer has been discovered. Accordingly, we can conclude the significant influence of dune configurations on the aloft turbulent flow. Meanwhile, such turbulent flow redistribution is able to stimulate strong sediment saltation and transportation.

Figure 4.8 is the conceptual schematic of the coherent structure evolution process. Panel (a) and (b) are the evolutionary process of spanwise and streamwise (interdune) vortex rollers respectively, where the red and blue color denote the positive and negative streamwise rotating direction. As panel (a) shows, the large spanwise roller in response to the Kelvin–Helmholtz instability is the original vortex resource to the coherent structures warping along dune brinklines (Figure 4.3 and 4.7). The spanwise roller keeps positive spanwise rotating associated with dune stoss side sediment saltation. When the turbulence gets developed with the full range of length scales being formed, the large scale roller breaks into the conglomeration of smaller length scale vortex rollers. The higher-order modes instability in mixing layer stretches and kinks the vortex rollers to a head-up hairpin vortex out of horizontal plane. Panel (b) shows the coherent structure, interdune roller, in response to the dune morphodynamic interaction (refer Figure 4.3 and 4.7). From the preceding results, the positive streamwise rotating interdune roller is sustained by the vortex stretching $S(\boldsymbol{x}, t)$ in the streamwise vorticity advection (Equation 3.8). As upcoming dune catches up the downflow dune, because of mass conservation, the high momentum flux dominates in flow channeling and strengthens the surface shear in the corresponding areas. Continuous rotating streamwise roller scours the sediment on downflow dune in an asymmetric pattern (the green area in figure 4.8 (b)). When small scales emerge, the interdune roller can break laterally (refer Figure 4.3 (b)) evolving into aggregations of hairpin vortices and small scale streamwise vortex rollers. In the following section, I will systematically explore the spatial extent of turbulence in DFSL, and pose the results within the context of physics.

CHAPTER 5

DUNE-FIELD BOUNDARY LAYER ANALYSIS

In previous sections, 3D visualization of flow over idealized and realistic cases reveals the emergence of two persistent vortex motions: *(i)* mixing-layer-like or hairpin-like vortices, primarily aloft the dune canopy; *(ii)* interdune streamwise vortex roller. In this section, to advance the analysis of DFSL and inertial layer, the spatial attributes of turbulence within DFSL and inertial layer is quantified via computation of the two-point correlation of fluctuating streamwise velocity:

$$\rho_{\tilde{u}'\tilde{u}'}(\boldsymbol{x};\lambda_x) = \frac{\langle \tilde{u}'(\boldsymbol{x},t)\tilde{u}'(x+\lambda_x,y,z,t)\rangle_t}{\langle(\tilde{u}')^2(\boldsymbol{x},t)\rangle_t^{1/2}\langle(\tilde{u}')^2(\boldsymbol{x},t)\rangle_t^{1/2}}, \tag{5.1}$$

where λ_x is spatial lag in the x direction, while $\langle(\tilde{u}')^2(\boldsymbol{x},t)\rangle_t^{1/2}$ is the root mean square of streamwise velocity fluctuation. From computation of $\rho_{\tilde{u}'\tilde{u}'}(\boldsymbol{x};\lambda_x)$, the integral length is as following:

$$L(\boldsymbol{x}) = \underbrace{arg}_{\Delta x}(\rho_{\tilde{u}'\tilde{u}'}(\boldsymbol{x};\Delta x) = \zeta), \tag{5.2}$$

where ζ is a pre-defined correlation threshold. According to extensive testing (not shown here), I have found $\zeta = 0.7$ is able to provide stable indication on the spatial attribute of dune flow (too low or high value for ζ can underestimate or overestimate the eddy length scale). Subsequently, low-pass filtered $L(\boldsymbol{x})$ at filter scale, $\delta_f/h = 4$, which removes the signal oscillations and facilitate the observations. Various external length scales have been considered to normalize the spatial extent of turbulence in wall-sheared turbulence. Within the canopy flow and roughness sublayer, vorticity thickness is adopted in the following works (Browand and Troutt, 1985; Raupach et al., 1996; Anderson and Chamecki, 2014):

$$l_\omega(\boldsymbol{x}) = \min\left(2\frac{\langle\tilde{u}(\boldsymbol{x},t)\rangle_{xyt}}{\frac{d\langle\tilde{u}(\boldsymbol{x},t)\rangle_{xyt}}{dz}}\right), \tag{5.3}$$

where the minimum of $l_\omega(\boldsymbol{x})$ is selected, because this value corresponds with the maximum of wall-normal shear and the elevation at which $\langle\tilde{u}(\boldsymbol{x},t)\rangle_{xyt}$ shows an inflection. This spatial external length scale metric has already been verified within roughness sublayer, wherein the maximum near-wall gradient is approximately co-located with the aggregate element height. Beyond roughness sublayer, $z/h \gtrsim 5$, the inertial layer overlaid, the attached-eddy hypothesis validity dictates the linear relation between the turbulence length scale and wall-normal elevation (Townsend, 1976):

$$l_\kappa(\boldsymbol{x}) = \kappa z, \tag{5.4}$$

where κ is Von Kármán constant. Recently, (Pan and Chamecki, 2016) has indicated the dissipation length l_ϵ can be sued as a transcendent normalizing length scale, which is defined as following:

$$l_\epsilon(\boldsymbol{x}) = \frac{u_*^3}{\epsilon(\boldsymbol{x})}, \tag{5.5}$$

where ϵ is the local dissipation, computed here via the presumption of a self-similar inertial-range cascade of turbulent kinetic energy across grid length scale, $\epsilon(\boldsymbol{x}) = \langle \boldsymbol{\tau}^d \rangle_t : \langle \mathbf{S} \rangle_t$ (Pope, 2000). The shear velocity in dissipation length is recovered a posteriori via the maximum streamwise–wall-normal Reynolds stress

$$u_*(\boldsymbol{x}) = \max(\langle T_{xz} \rangle_t(\boldsymbol{x})) = \max\left(\underbrace{\langle \tau_{xz} \rangle_t(\boldsymbol{x})}_{SGS} + \underbrace{\langle \tilde{u}'\tilde{w}' \rangle_t(\boldsymbol{x})}_{Resolved}\right), \tag{5.6}$$

which has the consistency with previous canopy flow works (Bailey and Stoll, 2016; Anderson and Chamecki, 2014). The following results in idealized and realistic dune fields, consistently, testify the integral length scales could be in l_ω and l_κ metric in the DFSL and inertial layer separately, following the verification for that DFSL could be categorized as an obstructed shear flow. Meanwhile, the results display that streamwise spacing can be used to fully collapse the integral lengths between cases, which, again, highlights the importance of dune configurations on spatial length scale of turbulence eddies in DFSL. The evidences are composed by idealized data (Section 5.1) and realistic data (Section 5.2) separately. [1]

[1]This chapter is based on the journal paper: Wang C, Anderson W. Turbulence Coherence Within Canonical and Realistic Aeolian Dune-Field Roughness Sublayers[J]. *Boundary-Layer Meteorology*, 2019: 1-26.

5.1 Idealized Case

Figure 5.1 shows the low-pass filtered integral length retrieved from Equation 5.2 in idealized cases, normalized by the small dune height h. Integral length profiles recovers turbulence eddy length scale in DFSL and inertial layer (Figure 5.1 (a) shows the direction of increasing height by the black quiver, which has been adopted in all panels in this figure). The integral length scale is shown over streamwise position x', which is denoted on Figure 2.2 (a) as the local streamwise coordinate with origin at the crest of the small dune for Case $S2$, $S3$, $S4$ (for Case $S1$, the origin of x' is taken as simply $x' = 30$). As expected, x'/h range is diminishing from $S2$ to $S4$, as interdune space decreasing. From the following results, s_x/h has found to be the correct length scale to normalize streamwise position x', giving various sets of collapsed profiles in all cases.

The top abscissa and right ordinate annotations denote the case and spanwise transect, respectively. Beginning with Case $S1$ (Panel a,e,i) which has served as a benchmark throughout the subsequent results, it interestingly captures the strong effect of large dune for integral length profiles, that is the near-wall integral length scale monotonically increases as the spanwise transect approaches the large dune centerline (from locations F_1 to F_3). Moreover, Panel (e,i) show that $L(x'/h)$ in inertial-layer is insensitive to x', while a critical change of $L(x'/h)$ emerges in the DFSL region as the large dune is approached. The perception of diminishing spatial extent is a natural consequence of discrete locations closer to the large dune, where the dune itself regulates the spatial extent of eddies by virtue of the attached-eddy hypothesis (Townsend, 1976).

According to Figure 5.1 Panel (b-d), (f-h) and (j-l), when a small dune gets closer to large dune, inertial-layer length scales remain constants effectively. However, the canopy length scale changes dramatically, compared with Case $S1$. Unlike $S1$ profiles, wherein the $L(x'/h)$ is constant close to the ground until attenuation via the large dune, for Case $S2$ and $S3$ there is a persistent pattern of growth and collapse. Such pattern keeps evident in

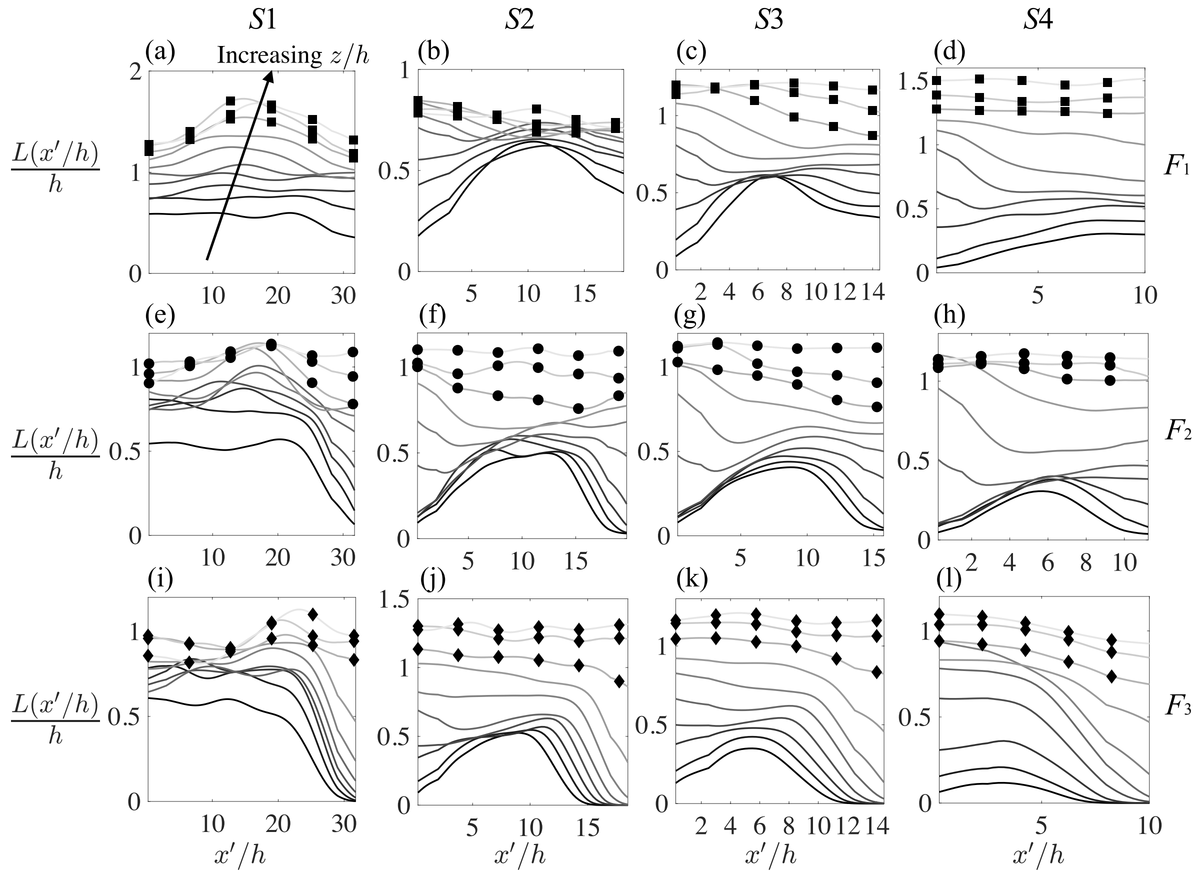

Figure 5.1. Local, low-pass filtered integral length (Equation 5.2), normalized by the small dune height h for all canonical cases at different wall-normal elevations; annotations are provided for the case (top abscissa), spanwise location (right ordinate), and elevation (Panel (a)). Figure 2.2 (a) shows the local coordinate axis, x', and spanwise locations, F_1, F_2 and F_3. From black to light gray line, the solid lines are $L(\rho_{\tilde{u}'\tilde{u}'} = 0.7)$ form $z/h = 0.25$ to $z/h = 2.5$, with vertical increment $\Delta_z/h = 0.25$. Panels (a,e,i): Case $S1$; Panel (b,f,j): Case $S2$; Panel (c,g,k): Case $S3$; Panel (d,h,l): Case $S4$. Panel (a-d), (e-h), (i-l) correspond with transects $F1$, $F2$, $F3$, respectively.

all transects (F_1 to F_3), although the spanwise-offset distance s_y/h is highlighted previously. In fact, this growth and collapse pattern is a consequence of the downflow thickening of Kevin-Helmholtz vortices, which is shed off from small dune brinkline (see Figure 4.1). As x' increases, downflow shed vortices length scale is growing and evolving ($0 \leqslant x' \lesssim 10$ for $S2$; $0 \leqslant x' \lesssim 8$ for $S3$), but the increasing trend of L is eventually precluded by downwind large dune. As downflow dune is approached, L shows a collapsing trend from different elevations, where $\partial_{x'} L < 0$ is evident in $S1$ to $S3$. However, in $S4$, as what we expected, small streamwise offset distance s_x/h precludes growing and collapsing pattern formations. Moreover, the shed vortices from small dune is constrained by the downflow dune immediately because of such limited streamwise offset.

For the understanding of integral length scale self-similarity in different layers (roughness layer and inertial layer), Figure 5.2 and 5.3 are prepared, wherein different length scales have been adopted to normalize selected integral length scales. Figure 5.2 shows selected integral length scales from Figure 5.1 normalized by small dune height h (Panel (a-d)), dissipation length l_ϵ (Panel (d-f), Equation 5.5), and vorticity thickness l_ω (Panel (g-i), Equation 5.3). Figure 5.3 shows the profiles of streamwise-averaged inertial layer length scales against attached-eddy length scale (wall-normal elevation) l_κ, respectively. The effects of streamwise offset spacing is obviously isolated via placing the profiles for Case $S2$, $S3$ and $S4$ in same panel.

Figure 5.2 (a-c) show $L(x'/h)$, collected from Transect F_2 (the centerline of small dune), is normalized by the small dune height and x' is normalized by streamwise offset s_x (see Table 2.1). The profiles at three different elevations exhibit growing and collapsing pattern, which has been discussed in Figure 5.1. The growing rate is depends on streamwise offset spacing, s_x. The attenuation to the increasing trend of L is affected by the downwind dune, however, the attenuation strength is weaker on lower elevations (compare with Panel (a) and (c)). For Panel (d-i), x' is normalized by s_x, and L is normalized by l_ϵ (d-f), and l_ω

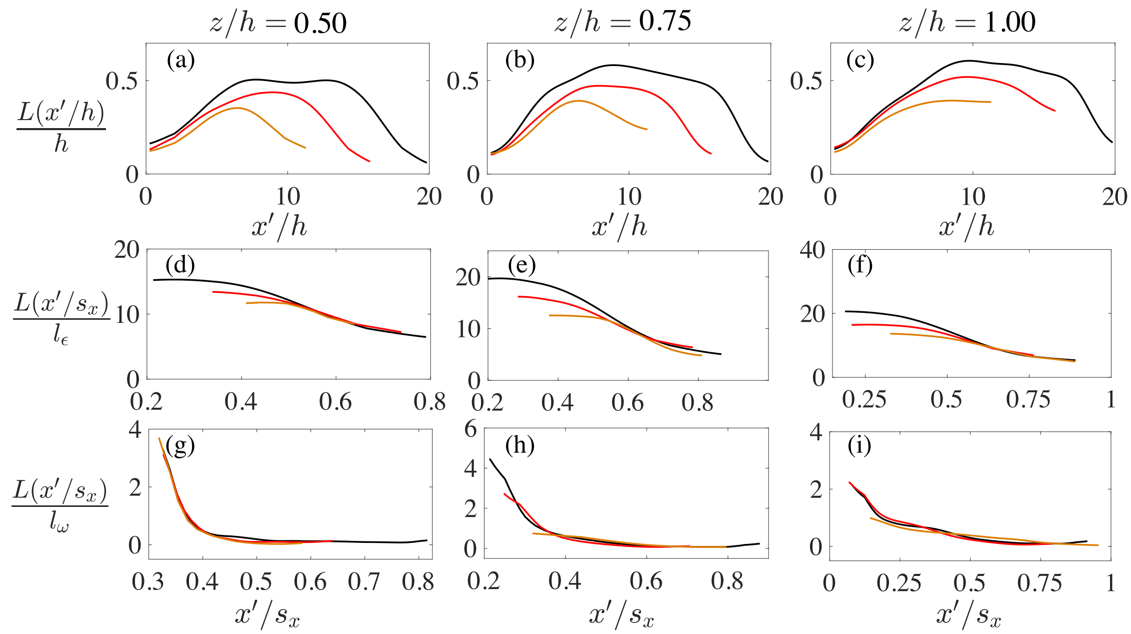

Figure 5.2. Integral lengths normalized by small dune height (a-c), dissipation length (d-f, Equation 5.5), and vorticity thickness (g-i, Equation 5.3); the profiles are shown for select elevations, $z/h = 0.5$, $z/h = 0.75$, and $z/h = 1.0$, from Figure 5.1, for Case $S2$ (black), $S3$ (red), and $S4$ (orange). Streamwise displacement is normalized by streamwise spacing between the small and large dune, which is denoted on Figure 2.2 (a).

(g-i). To varying degrees, the profiles collapse, wherein a greater self-similarity is obtained via L normalized by l_ω for all x'/s_x. For $x' \gtrsim 0.5$, the L/l_ϵ collapse is similar to L/l_ω. Note that the differing magnitudes of L/l_ϵ and L/l_ω is resulted by the different length scale magnitudes. According to the results, two key deductions can be achieved: *(i)* in DFSL, at least for the offset interaction considered here, is self-similar, even with decreasing streamwise offset spacing s_x; *(ii)* vorticity thickness l_ω is an appropriate length scale to normalize length scales in DFSL, which favorably provides evidence that DFSL could be categorized as an obstructed shear layer, although subtle aspects of the canopy flow are unique to dunes (i.e., Figure 4.3, 4.7, 4.8). Meanwhile, such results consistently verified the previous finding that the obstructed shear flow in DFSL displays mixing-layer analogy (Anderson and Chamecki, 2014).

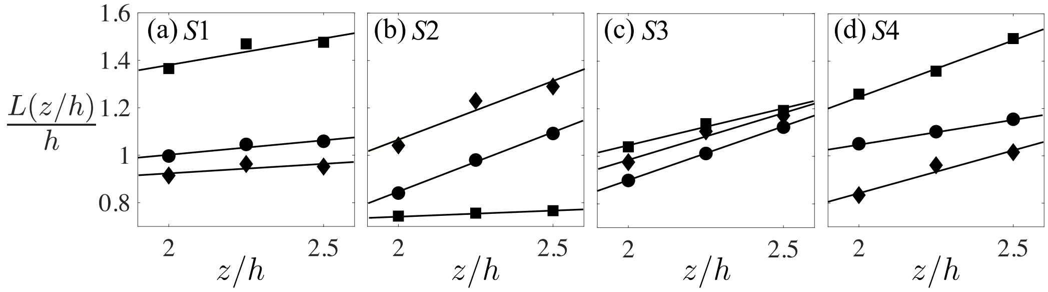

Figure 5.3. Streamwise-Averaged integral length at three different heights: $z/h = 2, 2.25, 2.50$, which corresponds with the highest three profiles on Figure 5.1 and immersed within inertial layer aloft (the consistent symbols are used in both figures). Panel (a-d) are Case $S1$ to $S4$. The cube, circle and diamond denote the integral value at spanwise transects $F1$, $F2$, $F3$. A linear fit has been added for perspective.

Figure 5.2 focuses on analysis of the spatial attributes of turbulent eddies in DFSL. While, Figure 5.3 shows the spatial characteristics at higher elevations. From (Grass, 1971), spatial heterogeneity of DFSL homogenizes with increasing elevations and at some multiple of obstacle heights above the canopy, the flow attains 'channel-like' conditions. Figure 5.3 demonstrate the similar transition for the flow over dune field via showing the high-elevation integral length profiles from Figure 5.1 (profiles with markers). In all Transects F_1, F_2 and F_3, streamwise-averaged integral length scales is linearly correlated to the wall-normal elevation, $L/h \sim z$, consistent with the notion of attached-eddy spatial extents increasing linearly with wall normal elevation ($L \sim l_\kappa$).

In this chapter, through integral length scale calculation in idealized dune cases, the growing and collapsing pattern of interdune eddies was established. Via the representational length scale normalizing, mixing-layer analogy for shear flow in DFSL has been verified efficiently. Indeed, DFSL is an obstructed shear flow, but the application to canonical arrangements limits generality. In the next section, same length scale analysis will be executed on realistic WSNM dune topography, which shows a great consistency.

5.2 Realistic Case

Figure 5.4 shows the integral length profiles normalized by the maximum of dune height, h_w (see Table 2.1, $h_w = \max(h(\boldsymbol{x}))/H$). In Figure 3.7, x' origin is placed at the local upflow crest. Unlike the idealized dune cases, in White Sands National Monument dune field, the obvious streamwise or spanwise offset spacing does not clearly exist. In order to execute comparing work with ideal cases, a series of transects have been selected shown in Figure 2.2 as T_1 to T_{16}, for the universality and representativity. As per the idealized case arrangements, the outer-layer integral length scales keeps impactful invariant on x', but inside of the roughness sublayer, evident growing and collapsing pattern exists at every transect, however, the magnitude of which is different and depends on local dune field attributes. Transects T_{11} and T_{15} (Panel (k,o)) display a very evident growing trend at the x' starting region, corresponding to a fast thickening Kevin-Helmholtz mixing layer. Unlike vegetative canopies, the loose distribution with crescentic hill feature provides a sufficient spacing for mixing layer eddies evolving (see Figure 5.1). Based on the realistic dune results, such underlined deduction becomes more potent. From the inspection of Figure 2.2, T_{11} and T_{15} correspond with transects following distinct crests and relatively large interdune spaces preceding the next dunes. Comparatively, T_1, T_4 and T_7 are showing weaker growing gradient in Panel (a,d,g). These transects corresponds with smaller interdune spacing, associated with less growing space for mixing layer eddies. Thus, accordingly, the gradient of growth for L shows evidently strong dependence on interdune space. From Figures 5.1 and 5.4, T_{11}, T_{15} exhibit a strikingly great consistency with $S2$; while, T_1, T_4 and T_7 maintain the deduction in $S4$.

The growing and collapsing pattern keeps a great evidence in WSNM topography, although some differences or invariances in integral length scales are observed in some transects due to the complexity of the current DEM. Figure 5.1 and Figure 5.4 indicate a consilient mixing layer evolving feature, already captured via preceding 2D visualization of turbulent

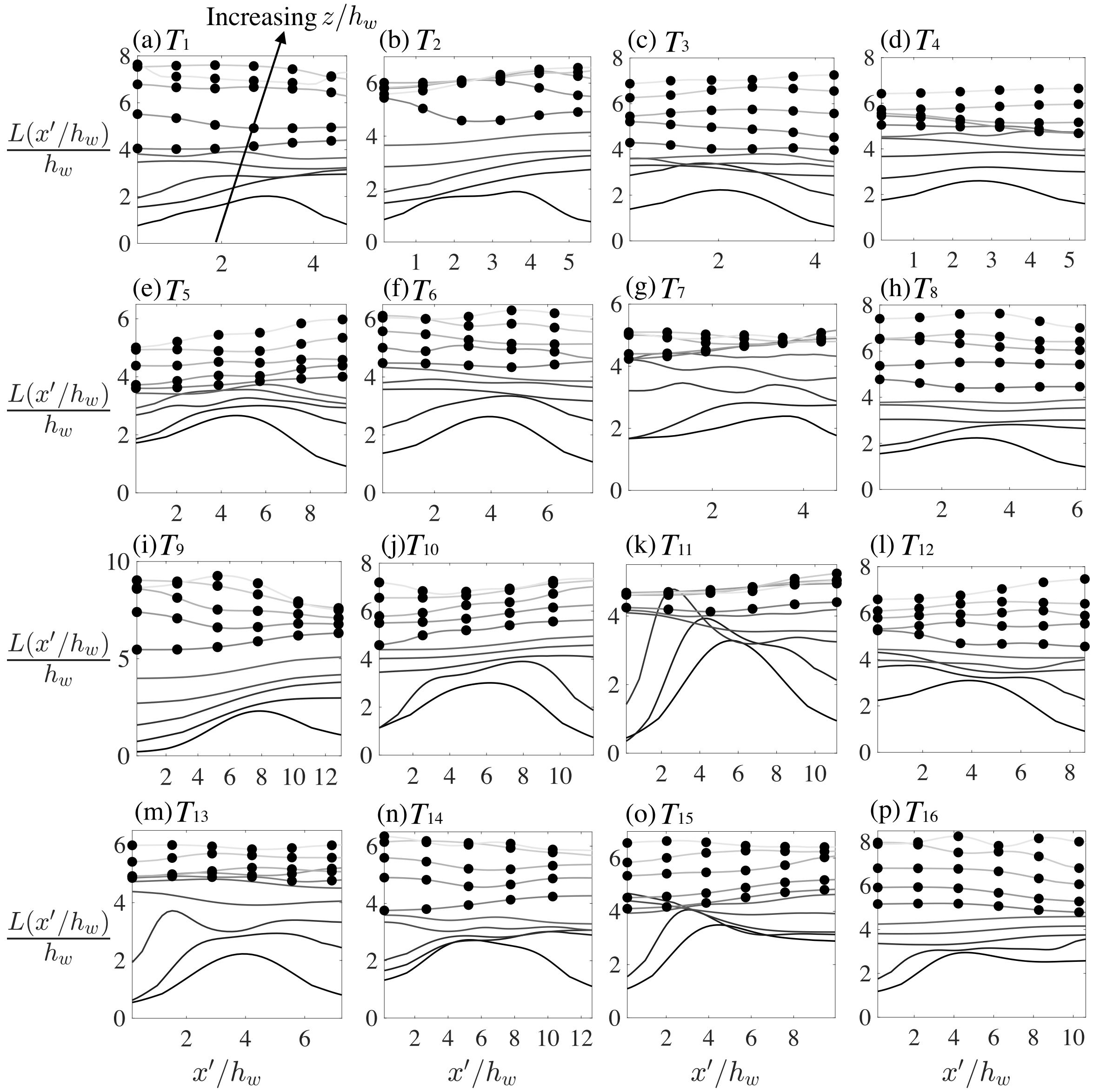

Figure 5.4. Local, low-pass filtered integral length scale, normalized by h_w, recovered by *a posteriori* from LES of flow over the WSNM DEM. The integral length is shown at a series of wall-normal elevations, from $z/h_w = 0.13$ (black) to $z/h_w = 2.5$ (light gray), with uniform vertical increment, $\Delta_z/h_w = 0.26$. On Panel (a), the black quiver denotes the direction of increasing wall-normal elevation. Panel (a-p) corresponds with Transects T_1 to T_{16} respectively on Figure 5.1 (b). Simulation results are from WSNM3 (Table 2.1 contains simulation attributes).

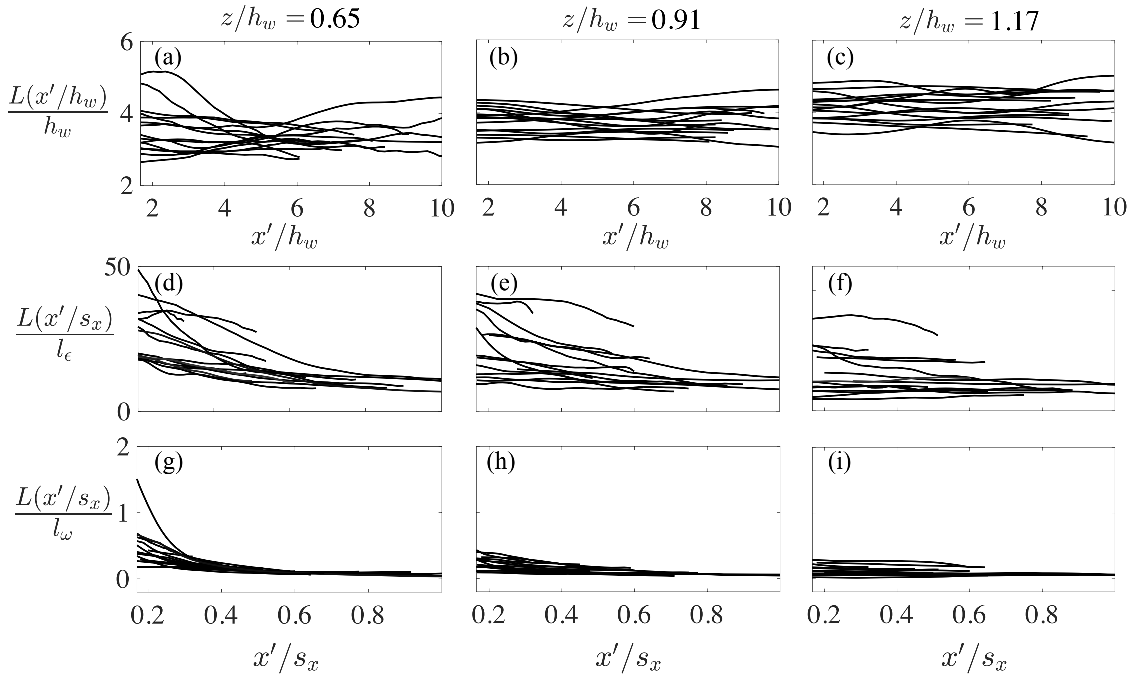

Figure 5.5. Local, low-pass filtered spatial integral length, L (Equation 5.2), normalized by different length scales at a series of different wall-normal elevations within the roughness sublayer $z/h_w = 0.65$ (a,d,g), $z/h_w = 0.91$ (b,e,h), and $z/h_w = 1.17$ (c,f,i). Panel (a-f): $L(x')/h_w$ against x'/h_w; Panel (d-f): $L(x')/l_\epsilon$ against x'/h_w; Panel (g-i): $L(x')/h_w$ against x'/h_w. Simulation results are from WSNM3 (Table 2.1 contains simulation attributes).

kinetic energy in $S1$ (Figure 4.1). The growth of mixing layer eddies corresponds to the positive $\partial L(x')/\partial x' > 0$, the thickening progress of vortex shedding in dune leeward. While, the collapsing profiles associated with $\partial L(x')/\partial x' < 0$ is due to the downwind shear flow obstructed. Like Figure 5.1, should the regulating length be distance to the ground, the integral length will remain approximately constant in the downflow direction – as is observed at Transect T_2 and T_{10}, where inspection from Figure 2.2 indicates these transects correspond to large interdune space and relatively modest downflow dune steepness. Meanwhile, for both cases, the integral length scales eventually come forth as the regulating length scales which is noted the beginning of the collapse phase through the attached-eddy hypothesis (Townsend, 1976).

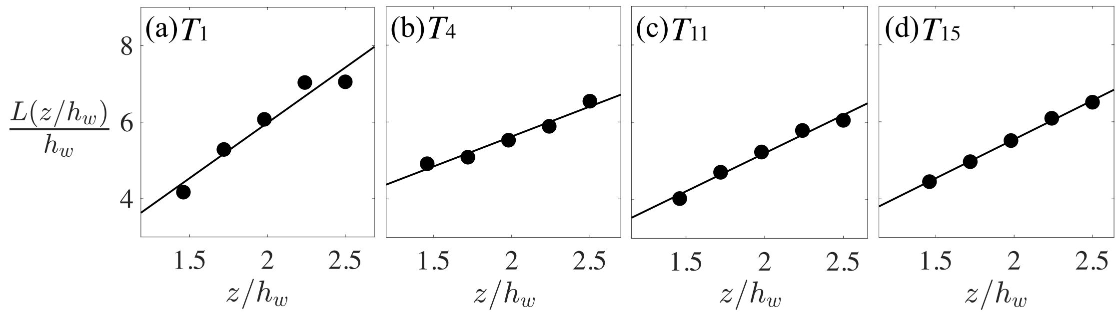

Figure 5.6. Streamwise-averaged integral length at five different heights: $z/h_w = 1.46, 1.72, 1.98, 2.24, 2.50$ respectively, which corresponds with the highest five profiles in Figure 5.4. Panels (a-d) corresponds with Transects T_1, T_4, T_{11}, T_{15} respectively. A linear line of best fit has been added (solid black) for reference. Simulation results are from WSNM3 (Table 2.1 contains simulation attributes).

Within dune field roughness sublayer, Figure 5.5 shows the superimposed integral length scales scaled by different length scales: Panel (a-c) maximum dune height h_w; Panel (d-f) dissipation length scale l_ϵ; Panel (g-i) mixing layer length scales l_ω. In Panel (a-c), x' is normalized by h_w, while in Panel (d-i), x' is normalized by streamwise offset spacing, s_x. L/h_w displays a wide range of variability at all elevations in Panel (a-c). The varying range gets reduced after being normalized by dissipation length l_ϵ and shown against x'/s_x, where there is a general descending correlation with x'/s_x increasing. However, the optimal collapse is achieved when L is scaled by l_ω and shown against x'/s_x, consistent with idealized dune results (Figure 5.2). This result provides the further evidence that within the complex natural dune field, the dune field roughness sublayer is showing obstructed shear flow attributes, which pertains highlighted mixing-layer flow analogies.

The scaling results of outer-layer integral length scales over realistic dune field are displayed in Figure 5.6. The selected integral length profiles are highlighted in Figure 5.4 at highly elevated positions, like the idealized cases. The streamwise-averaged values are retrieved from these data points which are shown against wall-normal elevations z/h_w. In the interest of brevity, we have not displayed inertial-layer profiles L/h_w over all Transects, instead, have shown the selected ones – T_1, T_4, T_{11} and T_{15}, where the former two and latter two transects correspond to the least and most DFSL disturbances. The apparent linear relation between L/h_w and z/h_w validates the preceding notion $L \sim l_\kappa$, as per the attached-eddy hypothesis, which indicates the wall-normal elevation regulated turbulent eddy spatial extents. For the completeness, Figure 5.7 has been displayed to summarize the dune-field boundary layer characteristics.

In this chapter, spatial attributes of turbulent boundary layer over dune field has been reveal via integral length scales calculations (Equation 5.2) in idealized and realistic dune cases. The growing and collapsing pattern of integral lengths reveal the vortex shedding thickening progress in dune leeward, associated with the evidence of attached-eddies feature in the downwelling of idealized cases. Such evolving progress has been captured in Chapter 4. Consilient scaling results indicate that dune field roughness sublayer (DFSL) is, in fact, the shear flow induced by dune topographies which shows mixing layer analogies, and attached-eddies is dominantly propagated at outer-layer with linearly wall-normal-elevation related spatial extent.

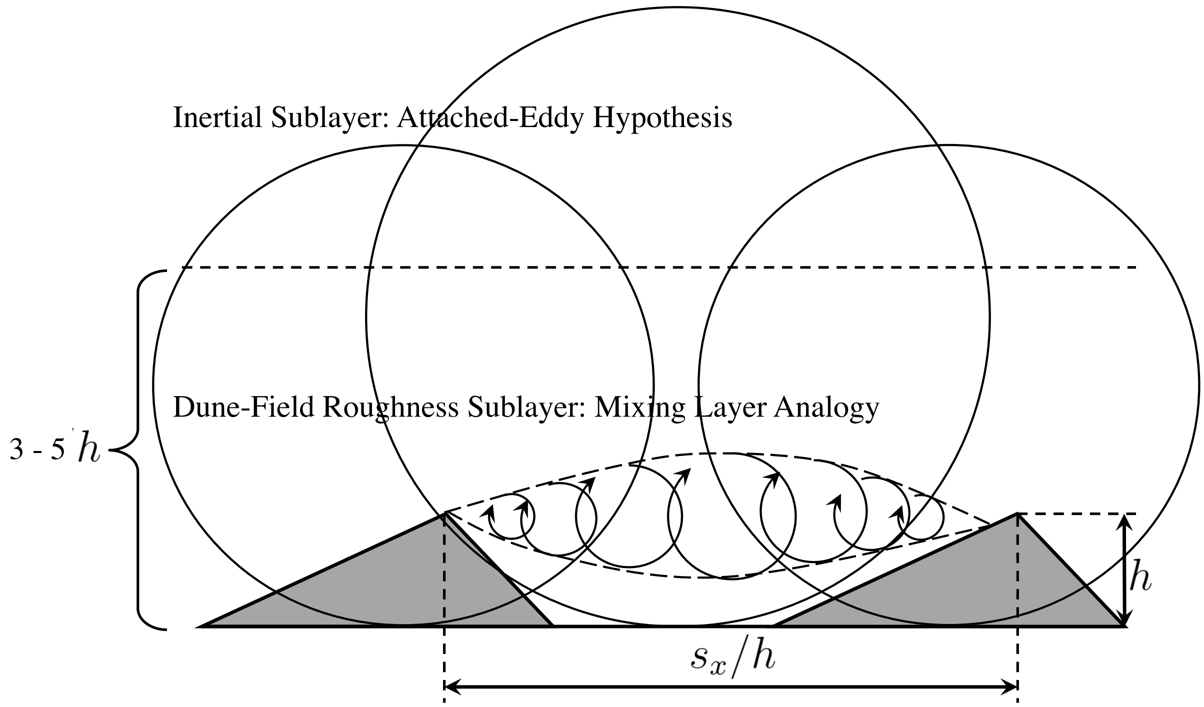

Figure 5.7. The structural model for dune-field boundary layer. It is composed by two subranges, inertial sublayer and dune-field roughness sublayer (DFSL) aloft local dune topographies. The wall-normal range of dune-field roughness sublayer can be 3 to 5 times dune field maximum heights h from the previous results. The turbulent coherency within DFSL displays mixing layer analogy where vortex shed off from dune brinklines and grows and thickened in the downwelling, consistent with the "growing trend" of the local integral length profiles; shed turbulent shear eddies advected by the upcoming wind and impinges on the downstream dune stoss side face and breaks into smaller length scale turbulent coherences, corresponding to the "collapsing trend" of the local integral lengths. The mixing layer attributes in DFSL has been revealed by the self-similarity of L/l_ω. Inertial layer overlays on DFSL where streamwise velocity keeps logarithmic profile associated with wall turbulence regime including attached-eddy hypothesis.

CHAPTER 6

CONCLUSION

Dune morphodynamics are affected by three major factors: *(i)* sediment availability (source); *(ii)* sediment stability (stability), which is related to vegetative density and soil moisture; *(iii)* turbulent flow (aeolian). Some other effects such as local topographic heterogeneity or seasonal effects could be effective in some critical scenarios, but in a certain location, these attributes are comparatively stable. In these aforementioned three crucial factors, sediment availability and stability have less variety for a very long time range at certain locations, which results in the significant role of atmospheric turbulent flow. The transient attributes of atmospheric flow complicate the analysis of morphodynamics, since surface aerodynamic loading is profoundly affected by turbulent flow. The surface aerodynamic loading, or surface shear, is a primary analyzing criteria for sediment erosion, wherein the surface threshold shear have been well defined by Bagnold Scheme (Equation 3.5) for morphodynamic prediction. To recover turbulent flow agitated by sand dunes' obstruction, Large-Eddy Simulation (LES) method is used in this work, the results of which have been well validated by Particle Image Velocimetry (PIV) experimental data displayed in Appendix A. Flow aloft sand dune field is in high-Reynolds number regime, wherein fluid viscosity can be neglected. In LES, large scale eddies are solved numerically and the filtered small scale eddies are obtained by the Lagrangian scale-dependent dynamic model. Under the fully rough conditions typical of environmental flows in rivers (fluvial) or the proximal effects responsible for a "building block" or elementary dune interaction known as an offset merger. The static dune arrangements in specific spatial locations are adopted as idealized case (Figure 2.2), which were informed by Figure 1.3 series of photographs which show how a small upflow dune approaching a downflow large dune. As the small dune approaches the large dune, the morphology of large dune is completely altered while the small dune morphology remains essentially invariant. In this arrangement, the small dune will eventually merge with the large dune while, simultaneously, a small dune will be ejected from the large dune (Ewing and Kocurek, 2010a; Kocurek et al., 2007; Frank and Kocurek, 1996; Kocurek and Ewing, 2005; Wang et al., 2016). To capture the aero- and hydrodynamic effects during the interaction, tow of the configurations featured downflow dunes with significant asymmetry ($S3$, $S4$, $S3_l$, $S4_l$) (Wang and Anderson, 2018b). In the interest of generality, White Sands National Monument (WSNM) aeolian dune field in southern New Mexico has been used as realistic study case. WSNM dune field is located in the Tularosa Basin of the Rio Grande Rift, between the San Andres and Sacramento Mountain Ranges. It consists of a core of barchan dunes, which abruptly transition to parabolic dunes (Kocurek et al., 2007; Ewing and Kocurek, 2010b). The major contributions of this work is revealing turbulent coherence evidences in dune-field roughness sublayer and ingeniously dictating mixing-layer flow characteristics from two points: *(i)* mixing-layer turbulent coherence genesis within DFSL; *(ii)* vorticity thickness scaled turbulent length scales.

6.1 Turbulent Coherence

The Reynolds-averaged wake profiles of each configuration in idealized case has been shown. The monotonically increasing trend of the wake centerline slope is highly correlated to streamwise offset spacing s_x, which is the so-called dune "wake-veering". The wake-veering magnitude is impaired by downflow dune asymmetric erosion Δx, which could increase downflow dune frontal area to absorb more interdune momentum flux. "Flow channeling" has been found as a crucial impactor for wake veering and upflow dune wake meandering. It is due to the downflow dune obstruction and flow mass conservation. Decreasing interdune region enhance flow channeling strength where elevated interdune momentum flux and turbulent mixing agitate stronger aeolian erosion on surface. Hairpin vortex shedding has been captured via instantaneous and conditionally-averaged Q criterion. Hairpin vortices shed off from dune brinkline, wherein the successive vortex core distance is linearly correlated to local dune crest height, $\lambda \sim h$, where h is the local dune crest height. According to the calculation of global wavelet power spectrum, accomplished by convolving the input time series of streamwise velocity fluctuations with a spectrum of wavelet functions, we can relate vortex shedding to Strouhal number in high-Reynolds number, $St = 0.25$. Meanwhile, the global energy spectrum in small dune wake reveals the monotonic increasing trend of vortex shedding energy depends on streamwise offset distance, s_x. Q criterion visualization also reveals a persistent interdune roller, the streamwise rotating of which is elucidated by isosurfaces of differential helicity. The large value of differential helicity in interdune roller indicates two attributes of local secondary flow: *(i)* flow channeling wherein streamwise velocity magnitude gets elevated by downflow dune obstructing, because of the mass conservation; *(ii)* positive streamwise rotating associated with the high-magnitude streamwise vorticity. Inspired by (Perkins, 1970), Reynolds-averaged streamwise vorticity transport equation has been studied in inside and outside of interdune region, respectively, via that, it is rational to ascribe interdune roller to vorticity stretching, $S(\boldsymbol{x})$. Such Prandtl's secondary flow of the first kind advances the understanding of turbulence in morphodynamics, which maintains a dune spacing related vortex structure inducing strong sediment saltation at interdune zone, triggering asymmetric erosion of downflow large dune. To testify this deduction, Bagnold Scheme is adopted to quantify sediment erosion through Immersed Boundary Method to approach surface shear. Results herein suggest that coherent flow structures within the interdune space – critical to the spatial distributions of basal stress, but entirely neglected by existing flow descriptions based on surface slope – are important in shaping the spatial complexity of natural dunes (Wang and Anderson, 2018b).

6.2 Mixing-Layer Analogy

Afterwards, two complementary components are displayed to understand preceding turbulent coherent structures in dune field roughness sublayer (interdune roller, hairpin vortices): *(i)* the evolving progress of vortical motions in dune field, accomplished by using Reynolds-averaged flow field, achieved from precursor simulations, as initial condition; *(ii)* underline the self-similarity of spatial nature of turbulence in roughness sublayer over dune field, which is accomplished via computation of the integral length at a series of spanwise transects spanning the idealized interaction and the White Sands National Monument dune field (Wang and Anderson, 2019a). The first component focuses on flow visualization in idealized and realistic dune field via Q criterion isosurfaces. Since the initial condition is Reynolds-averaged flow data, dune field perturbing flow instability in different length scales can be captured in all cases, where the emergence of mixing-layer-like hairpins (spanwise rollers) is evident above the dunes within DFSL. Within the dune canopy height, multiple persistent interdune rollers (streamwise vortex roller) are captured in flow channeling as well. With time advancing, spanwise rollers break into aggregations of small scales of turbulent eddies, which will grow and thicken in the downwelling region analogy mixing-layer type instabilities. Streamwise rollers will evolve to a train of hairpin vortices in small dune wake with increasing magnitude of turbulent $Q2$ and $Q4$ events. Turbulent ejection induced “Boil” event has been observed near the ground, inducing strong momentum and sediment mass flux (Omidyeganeh and Piomelli, 2011a). Thus, consistent with vegetative canopy, dune field flow features similar mixing-layer-like vortices, but interdune roller is distinct to dune fields due to special canopy configurations. Thereupon, to dig into the DFSL spatial attributes, integral length scales in idealized and realistic dune field has been computed. In all cases, the integral length scales display linear correlation with wall-normal elevation in the inertial layer, but the existences of dune topographies imparts significant influence on the spatial extent of turbulence in DFSL. A growing-collapsing trend pattern is robust in all cases. The growing trend is due to the thickening vortex shedding from upflow dune, and the collapsing is because of downflow dune obstructing (Wang and Anderson, 2019a). From the well collapsing of vorticity thickness normalized integral length scales, the innate character of DFSL is revealed, that is mixing-layer-analogized shear flow obstructed by dunes. For the turbulent eddies beyond five dune crest heights, bottom dune topographies has less influence, where turbulent coherent length scale shows linear correlation with local wall-normal elevation. It highlights the channel-flow characteristics within inertial sublayer.

APPENDIX A

EXPERIMENTAL VALIDATION

In this appendix, 2D snapshots of instantaneous results are presented from experiments and simulations in a manner that facilitates comparison. We stress, however, that dimensions are treated differently between both techniques. For generality, all spatial positions are normalized by small dune height, h, while the origin is centered at the toe of the large dune (see also Figure 2.2). The LES flow fields are normalized by the simulation shear velocity, u_*. The experimental flow fields, in contrast, are all shown in dimensional form (i.e., velocity, vorticity, and stresses are $\boldsymbol{u}\,[=]\,l\ t^{-1}$, $\boldsymbol{\omega}\,[=]\,t^{-1}$). Therefore, when viewing Figures A.1, A.2 and A.3, only spatial distributions of the different flow quantities can be compared. We necessarily present the data in this way since the experimental shear velocity is not available (if it were available, all experimental data would have been normalized in a manner identical to the simulation data). For comparison, a special case $S5$ has been adopted. (See Table 2.1 for $S5$ informations).

Experimental results shown in this session are reproduced results in (Wang et al., 2016) with permission from authors. The experiments were conducted in a Refractive-Index-Matched (RIM) flow facility located in the Laboratory for Turbulence and Complex Flow (LTCF) at the University of Illinois at Urbana-Champaign (Blois et al., 2012). The facility employs an aqueous solution (~63% by weight) of sodium iodide (NaI) as the working fluid (refractive index, RI, $n_f \sim 1.49$). The test section of the tunnel, constructed from acrylic, is 2.50 m long with a constant cross-section of 0.1125 × 0.1125 m. A temperature control system allowed fine-tuning the RI of the fluid by maintaining the temperature constant within 0.05°C, which translates to a 0.001% change in the fluid IR. Additional details on the RIM_UIUC facility are given in Blois et al. (2012) (Blois et al., 2012). Experiments were performed for one specific flow condition. The flow rate in the tunnel was kept constant.

The freestream velocity was $U_0 = 0.38$ m s^{-1}, while the boundary layer thickness was ≈ 45 mm at the measurement plane.

The barchan dune models were fabricated by casting a clear urethane material ($n_s \sim 1.49$) into specific molds. The physical dimensions of the larger barchan model were: height $h =$ 15 mm, width $w = 70$ mm, and length, $\lambda = 70$ mm (recall definition of these lengths on Figure 1.2 and accompanying text). The small barchan model had the same morphology but was 1/8$^{\text{th}}$ in volume. The barchan models were fixed to the side wall of the test section and immersed into the working fluid. By fine-tuning the temperature of the working fluid, the refractive indices of the fluid and the solid model were matched precisely. This procedure rendered the model invisible therefore facilitating full optical access to the flow around this complex three-dimensional topography.

The particle-image velocimetry (PIV) technique was used to acquire planar instantaneous velocity fields in select streamwise-spanwise ($x - y$) planes with a field of view large enough to capture the flow around both barchan models. Silver-coated hollow glass spheres (mean diameter, $\phi = 14$ μm) with a density of 1.7 g cm^{-3} were added to the flow to serve as PIV tracer particles. An 11 million pixel camera was used to image the flow, which was illuminated by a 50 mJ/pulse, dual-cavity, Nd:YAG laser (Litron Nano L PIV).

A series of optics were used to form a light sheet in the streamwise-spanwise plane (x-y) that was wide enough to illuminate the entire flow around both barchan models and to obtain a constant light-sheet thickness (~ 1 mm). The light was conveyed from the bottom of the tunnel using a system of optics mounted on a transition stage adjustable in the wall-normal (z) direction, which facilitated accurate positioning of the light sheet. Measurements in the x-y planes were performed at three wall-normal locations: $z/h = 1.0$, 2.0, and 2.66 for the data validation. An LES simulation has done based on the 3D model of barchan dunes in PIV measurement, for numerical results verifications.

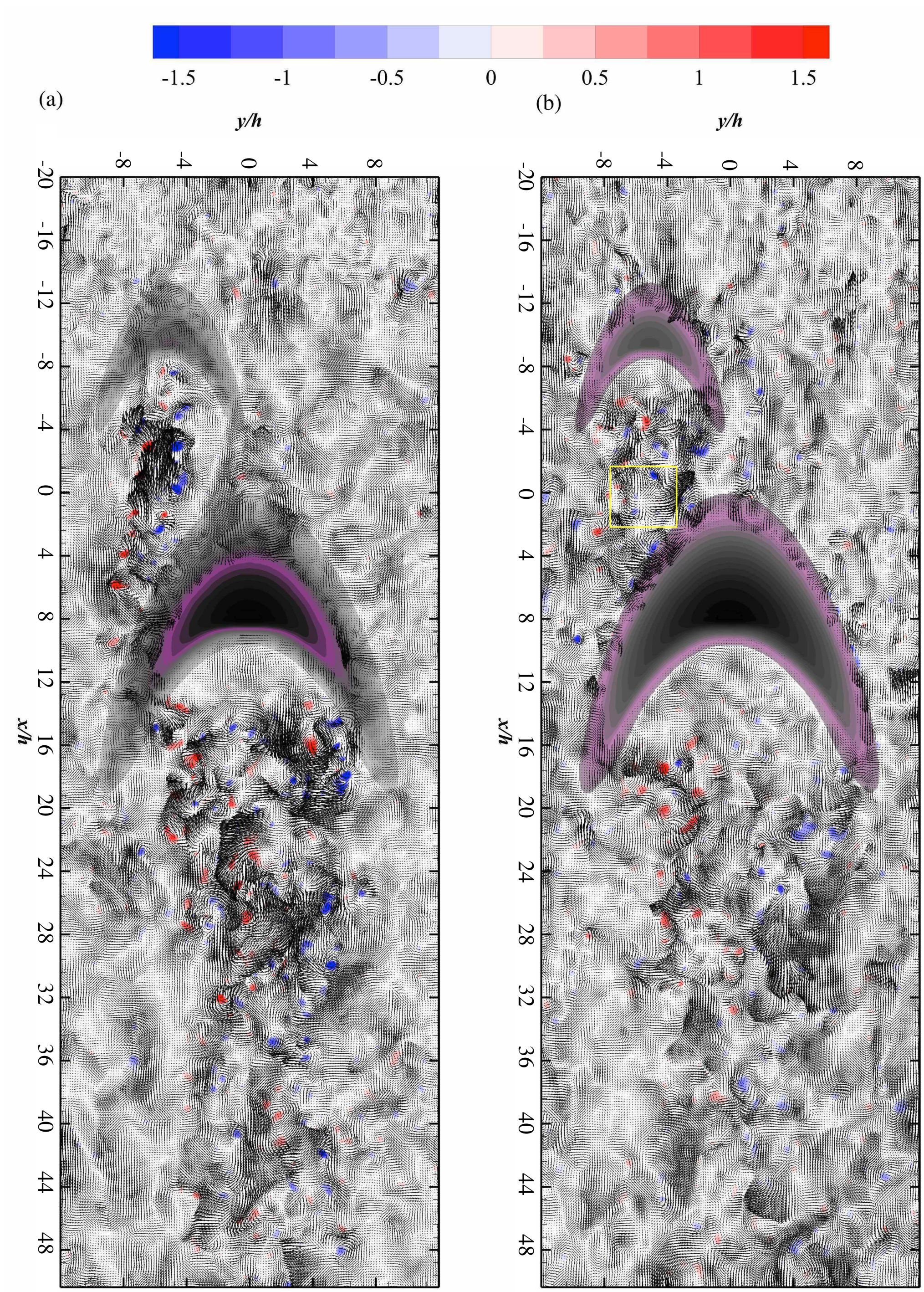

Figure A.1. Instantaneous visualization of flow over two interacting dunes in streamwise-spanwise planes at wall-normal elevations: (a) $z/h = 1.00$; and (b) $z/h = 0.50$. Contour and vectors are signed swirl strength, $\lambda^*_{c,z} = \lambda_c \hat{i}_{\omega,z}$, and fluctuating velocity comonents, $\{\tilde{u}'(x, y, z/h = 0.5, 1.0)/u_*, \{\tilde{v}'(x, y, z/h = 0.5, 1.0)/u_*\}$, respectively. Yellow square added in Panel (b) to highlight turbulent "Boil". Results are from PIV experiment.

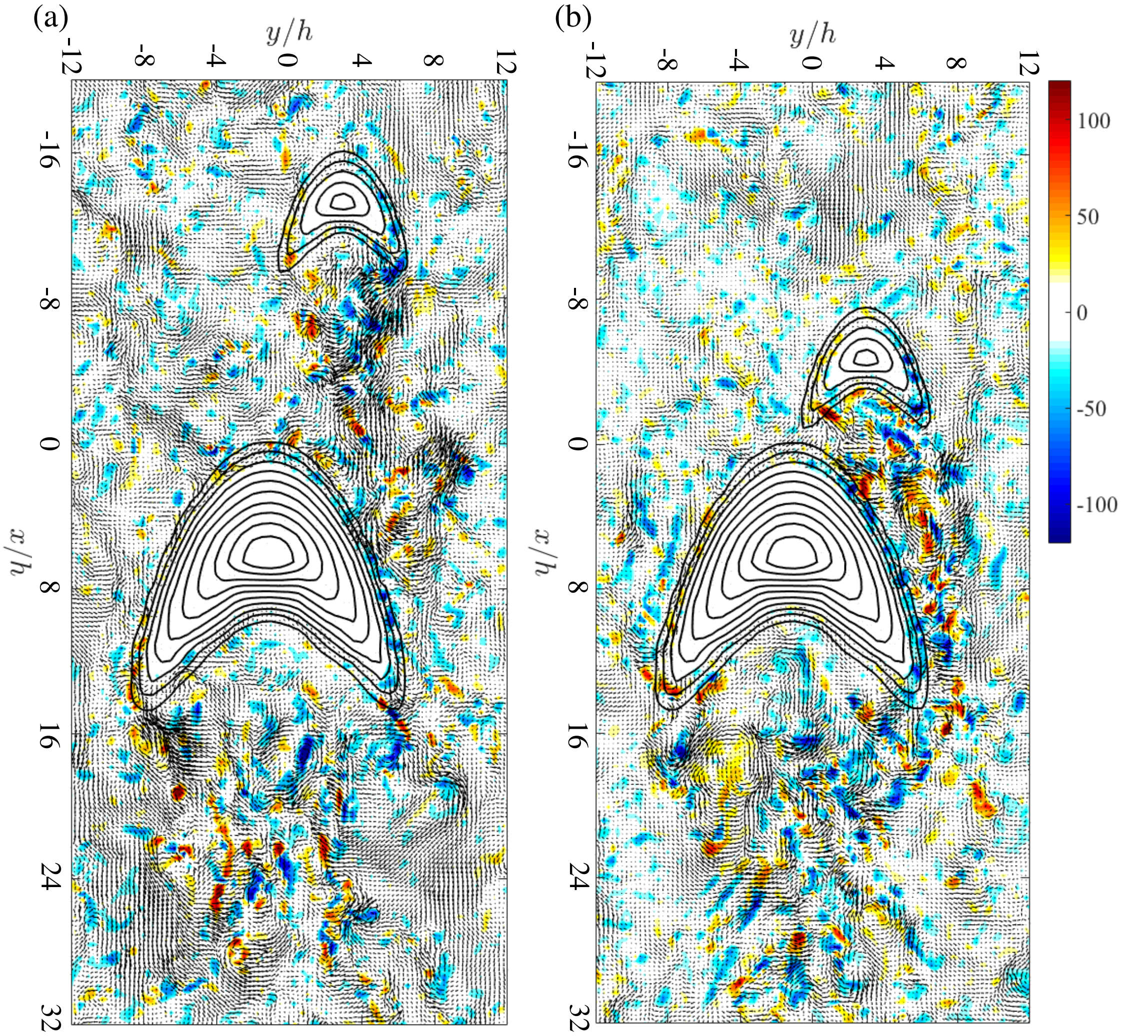

Figure A.2. Instantaneous visualization of flow over two interacting dunes in streamwise-spanwise planes at wall-normal elevation $z/h = 0.5$ in Case $S3'$ (a) and $S4'$ (b), respectively. Contour and vectors are signed swirl strength, $\lambda^*_{c,z} = \lambda_c \hat{i}_{\omega,z}$, and fluctuating velocity components, $\{\tilde{u}'(x, y, z/h = 0.5)/u_*, \{\tilde{v}'(x, y, z/h = 0.5)/u_*\}$, respectively.

Figure A.1 and A.2 both shows the instantaneous visualization of flow over idealized dune cases at different wall-normal elevations. Figure A.1 is retrieved from PIV measurements, while Figure A.2 is numerical results in Case $S3'$ (a) and $S4'$ (b), respectively. Both figures show instantaneous visualization of swirl strength signed by wall-normal component of the resolved vorticity unit vector, $\hat{\boldsymbol{i}}_\omega = \tilde{\boldsymbol{\omega}}/|\tilde{\boldsymbol{\omega}}| = \tilde{\omega}_x/|\tilde{\boldsymbol{\omega}}|\hat{i} + \tilde{\omega}_y/|\tilde{\boldsymbol{\omega}}|\hat{j} + \tilde{\omega}_z/|\tilde{\boldsymbol{\omega}}|\hat{k}$ (Wu and Christensen, 2010). Thus, the swirl strength is a vector quantity, $\boldsymbol{\lambda}_c^* = \lambda_c \hat{\boldsymbol{i}}_\omega$. Swirl strength is an illustrative quantity since it captures rotation, but not shear (as would otherwise be resolved with vorticity). The turbulent mixing process is evident at dune wake in both figures, associated with opposite swirling directions emanating from "left" and "right" horn in figures. In Figure A.1, experimental result has captured very fine resolution flow statistics, wherein even "Boil" structure has been observed at $z/h = 0.50$. Like the preceding shear layer visualization in Figure 4.1 and 4.2, large spanwise vortex rollers surrounding dune brinkline break into multiple small scale hairpin vortices in the wake and will grow and thicken afterwards. Besides, small dune wake veering phenomenon is evident in Panel (a). Same with experimental results, the effects of wake veering is evident in Figure A.2, but the enhanced flow channeling, indeed, stimulates more vibrant turbulent mixing. Thus, through comparing experimental and numerical results, the underlined conclusions, such as wake veering and flow channeling, have been well verified. However, it is still not precise enough to perorate via comparing 2D instantaneous visualization, because of the hardly-controlled temporally-dependent fluctuations and highly-density of velocity quivers. To advance the comparison, Case $S5$ is used here. $S5$ keeps the same spatial arrangements of dunes in PIV measurements, such as the streamwise and spanwise offset spacings. Except experimental s_x and s_y values, the other numerical parameters are maintained (see Table 2.1).

Figure A.3 (a) shows the Reynolds-averaged wall-normal vorticity $\langle\tilde{\omega}_z(\boldsymbol{x})\rangle_t = \partial\langle\tilde{v}\rangle_t/\partial x - \partial\langle\tilde{u}\rangle_t/\partial y$, overlapped with wake centerline data points, $\langle\tilde{\omega}_z(\boldsymbol{x})\rangle_t \approx 0$. Figure A.3 (b) shows the wake centerline profiles of small dune, where red data points are from PIV results, and

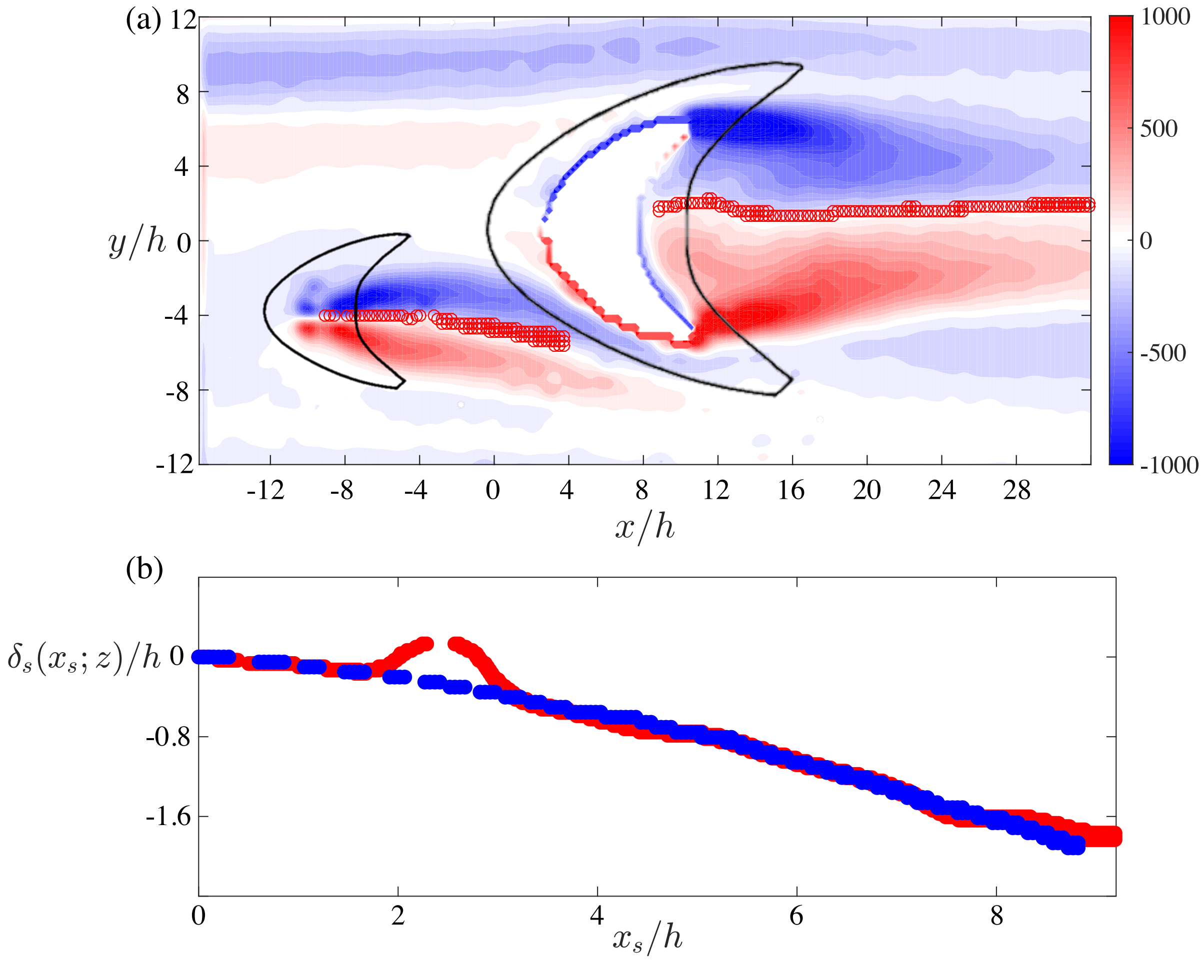

Figure A.3. Panel (a) shows the Reynolds-averaged wall-normal vorticity $\langle\tilde{\omega}_z(x,y,z/h=1.0)\rangle_t$ at the elevation of small dune height, $z/h = 1.0$, overlapped with data points where $\langle\tilde{\omega}(\boldsymbol{x})\rangle_t \approx 0$. Result is from PIV experimental measurement. Panel (b) shows the wake veering profiles of small dune at $z/h = 1.0$ from the PIV data and Case $S5$. The LES simulation $S5$ is trying to recover the experimental, which maintains the same spatial attributes with PIV dune models.

blue data points are from Case $S5$. From Panel (a), $\langle\tilde{\omega}_z(\boldsymbol{x})\rangle_t$ displays negative and positive distribution in each dune leeward. This is because in dune wake, $\partial\langle\tilde{v}\rangle_t/\partial x \ll \partial\langle\tilde{u}\rangle_t/\partial y$, thus $\langle\tilde{\omega}_z(\boldsymbol{x})\rangle_t \approx -\partial\langle\tilde{u}\rangle_t/\partial y$. Meanwhile, the overlapped wake centerline is evidently showing small and large dune wake veering. In Panel (b), the great collapse for blue and red data points indicates the validation of LES method results.

In this current appendix, LES data has been well verified by the comparing numerical and experimental datasets. Wake veering and flow channeling effects are evidently displayed in all results. For the convenience of comparison, $S5$ is used to match the experimental dune arrangements. The well collapsing wake veering profiles indicate the high credibility of LES data in this work. To verify the grid insensitivity of LES code, Appendix B will show gird insensitivity testing.

APPENDIX B

GRID INSENSITIVITY

For the universality and credibility of LES results in current work, the grid insensitivity test will be shown in the current appendix. Figure B.1 shows vertical profiles of plane- and Reynolds-averaged streamwise velocity in WSNM case (Panel (a)), and the idealized cases (Panels (b-e)), where panel annotations denote corresponding case. Profiles are shown for the relatively high- and low-resolution cases summarized in Table 2.1, where dashed and solid lines indicate low- and high-resolution cases, respectively. For all panels, the elevation, $\max(h)/H$, is shown for perspective (horizontal solid black line). The WSNM represents a 'field' type of flow statistics (Anderson and Chamecki, 2014), and as such plane-averaged streamwise velocity profile exhibits an inflection against wall-norma elevation, which is a distinctive attribute of canopy flows and responsible for the continual production of Kelvin–Helmholtz eddies. Although the idealized cases are also a portion of a field of identical interactions – by virtue of the periodic boundary conditions – the spatial extent of the computational domain minimizes the emergence of field-like conditions (Panel (a)). In terms of that, a pronounced inflection is not recovered in Panel (b-e). Nevertheless, it is evident that LES grid insensitivity has been achieved in all cases, at least within the context of the plane- and Reynolds-averaged streamwise velocity component.

To demonstrate grid insensitivity in a higher-order turbulence statistics, the profiles of the integral length are exhibited in Figure B.2, normalized by dune height (see Table 2.1 for the value of maximum dune crest height h_w in WSNM and h in idealized case) and vorticity thickness l_ω against x'/s_x for the idealized (Figure B.2 (a,b)) and realistic (Figure B.2 (c,d)) dune field. The profiles are displayed for the low- and high-resolution LES in dashed and solid lines, respectively, where Table 2.1 summarizes the simulation attributes. According to Figure B.2, different resolution will not induce evident results deviation. Thus, LES grid insensitivity is effectively verified via results comparison in different resolution cases.

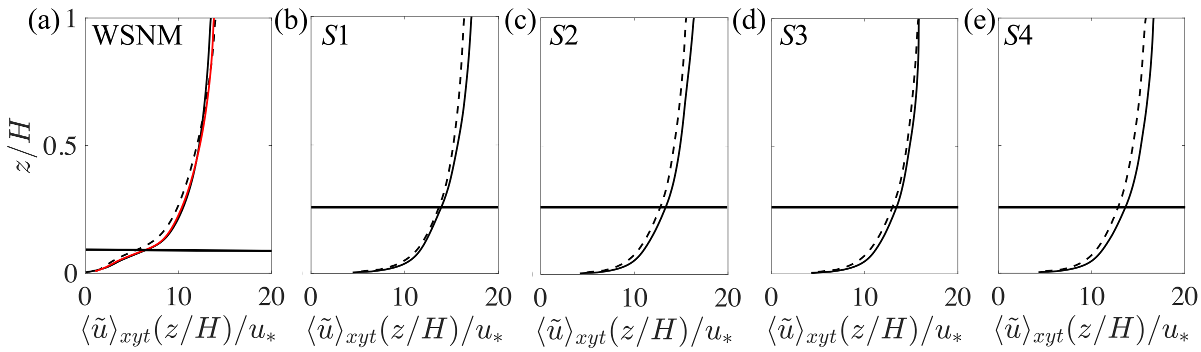

Figure B.1. Vertical profiles of plane- and Reynolds-averaged streamwise velocity for flow over WSNM (a) and idealized cases (b-e). On all panels, the solid and dashed black lines denoted relatively high- and low-resolution cases (see Table 2.1 for simulation details). The horizontal solid line denotes $\max(h(\boldsymbol{x}))$.

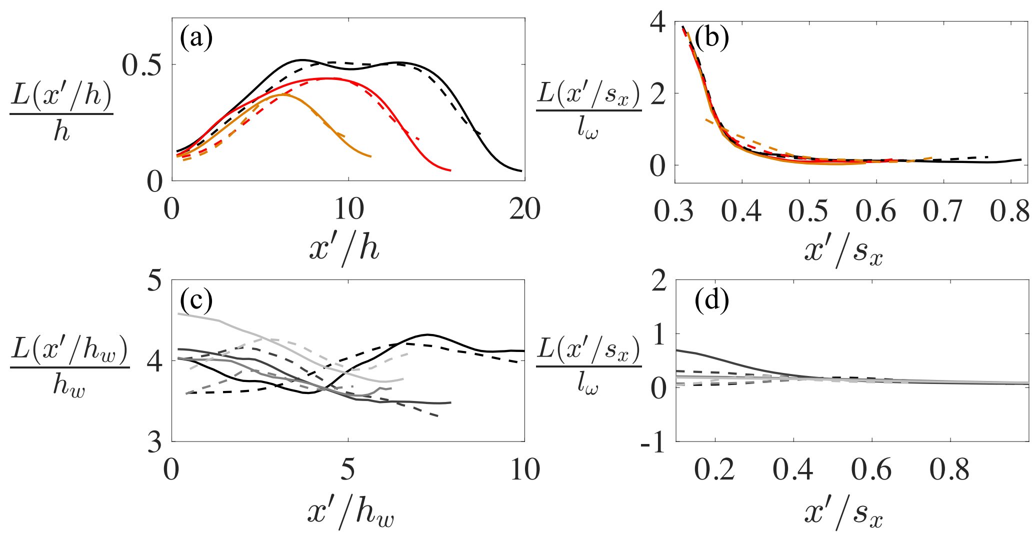

Figure B.2. Local low-pass filtered spatial integral length in idealized case (a,b) and realistic case (c,d) normalized by different length scales. Panel (a) and (b) are normalized by small dune height h and vorticity thickness l_ω respectively at $z/h = 0.5$ on line $F2$, where black, red and orange solid lines are cases $S2$, $S3$ and $S4$ respectively, while black, red and orange dashed lines are cases $S2_l$, $S3_l$ and $S4_l$ respectively. Panel (c) and (d) are normalized by WSNM dune height h_w and vorticity thickness l_ω respectively at $z/h_w = 0.91$. From gray line to black lines are Transects T_4, T_8, T_{12} and T_{16} respectively. Dashed lines are results in WSNM1. While solid lines are results in WSNM3.

Table B.1. Summary of variables in this work.

Variable	Definition	Formula
H	Domain height	/
L_x	Streamwise extent	/
L_y	Spanwise extent	/
L_z	Wall-normal extent	/
N_x	Streamwise grid number	/
N_y	Spanwise grid number	/
N_z	Wall-normal grid number	/
h	Small dune crest height	/
h_w	WSNM dune crest height	/
$\tilde{.}$	Grid-filtered quantity	/
$\hat{.}$	Conditionally-averaged quantity	/
$\langle . \rangle_n$	Averaged quantity on n dimension	/
$.'$	Fluctuating quantity	$. - \langle . \rangle_t$
s_x/h	Streamwise offset distance	/
s_y/h	Spanwise offset distance	/
$\Delta x/h$	Asymmetric distance	/
$\boldsymbol{u}(\boldsymbol{x}, t)$	Flow velocity	/
$\langle \tilde{\omega}_z \rangle_t$	Reynolds-averaged wall-normal vorticity	$\partial_x \langle \tilde{v} \rangle_t - \partial_y \langle \tilde{u} \rangle_t$
$\delta_s(x_s; z)$, $\delta_l(x_l; z)$	Small and large dune wake veering	/
$P(x)$	Probability density function	/
$Q(\boldsymbol{x})$	Q criterion	$\dfrac{1}{2}(\mathbf{S} : \mathbf{S} - \boldsymbol{\Omega} : \boldsymbol{\Omega})$
$\boldsymbol{\Omega}$	Rotation rate tensor	$\frac{1}{2}\left(\nabla \tilde{\boldsymbol{u}} - \nabla \tilde{\boldsymbol{u}}^{\mathrm{T}}\right)$
$\mathbf{S}$	Strain rate tensor	$\frac{1}{2}\left(\nabla \tilde{\boldsymbol{u}} + \nabla \tilde{\boldsymbol{u}}^{\mathrm{T}}\right)$
λ	Hairpin shedding distance	$\lambda \sim h(\boldsymbol{x})$
St	Strouhal number	$fh(\boldsymbol{x}) \langle \tilde{u}(\boldsymbol{x}) \rangle_t^{-1}$
$h_l(\boldsymbol{x})$	Differential helicity	$\langle \tilde{\boldsymbol{\omega}}(\boldsymbol{x}, t) \cdot \tilde{\boldsymbol{u}}(\boldsymbol{x}, t) \rangle_t$
$q(\boldsymbol{x}, t)$	Sand flux	$q(\boldsymbol{x}, t) \sim (u_*(\boldsymbol{x}, t))^3$
$u_*(\boldsymbol{x}, t)$	Friction velocity	$(\delta_z \lvert \boldsymbol{f}(\boldsymbol{x}, t) \rvert)^{1/2}$
$u_{*,t}$	Threshold friction velocity	$A_B \left(\frac{\rho_p}{\rho_a} g D_p\right)^{1/2}$
$\langle S_x(\boldsymbol{x}) \rangle_t$	Vorticity stretching	$\langle \tilde{\omega}_x \rangle_t \partial_x \langle \tilde{u} \rangle_t$
$\langle T_x(\boldsymbol{x}) \rangle_t$	Vorticity tilting	$\langle \tilde{\omega}_y \rangle_t \partial_y \langle \tilde{u} \rangle_t + \langle \tilde{\omega}_z \rangle_t \partial_z \langle \tilde{u} \rangle_t$
$\langle P_x(\boldsymbol{x}) \rangle_t$	Turbulent torque	$\epsilon_{xqi} \partial_q \partial_j \langle \mathsf{T}_{ij} \rangle_t$
$k(\boldsymbol{x})$	Turbulent kinetic energy	$\frac{1}{2}(\boldsymbol{u}' \cdot \boldsymbol{u}')$
$L(\boldsymbol{x})$	Integral length	$\underbrace{arg}_{\Delta x}(\rho_{\tilde{u}'\tilde{u}'}(\boldsymbol{x}; \Delta x) = \zeta)$
$l_\omega(\boldsymbol{x})$	Vorticity thickness	$\min\left(2 \frac{\langle \tilde{u}(\boldsymbol{x}, t) \rangle_{xyt}}{\frac{d \langle \tilde{u}(\boldsymbol{x}, t) \rangle_{xyt}}{dz}}\right)$
$l_\epsilon(\boldsymbol{x})$	Dissipation length	$\frac{u_*^3}{\epsilon(\boldsymbol{x})}$

REFERENCES

Albertson, J. and M. Parlange (1999). Surface length scales and shear stress: implications for land-atmosphere interaction over complex terrain. *Water Resour. Res. 35*, 2121–2132.

Alvarez, C. A. and E. M. Franklin (2018). Role of transverse displacements in the formation of subaqueous barchan dunes. *Physical review letters 121*(16), 164503.

Alvarez, C. A. and E. M. Franklin (2019, Oct). Horns of subaqueous barchan dunes: A study at the grain scale. *Phys. Rev. E 100*, 042904.

Anderson, W. (2012). An immersed boundary method wall model for high-reynolds number channel flow over complex topography. *Int. J. Numer. Methods Fluids 71*, 1588–1608.

Anderson, W. (2016). Amplitude modulation of streamwise velocity fluctuations in the roughness sublayer: evidence from large-eddy simulations. *J. Fluid Mech. 789*, 567–588.

Anderson, W. and M. Chamecki (2014). Numerical study of turbulent flow over complex aeolian dune fields: The White Sands National Monument. *Physical Review E 89*, 013005–1–14.

Anderson, W., Q. Li, and E. Bou-Zeid (2015). Numerical simulation of flow over urban-like topographies and evaluation of turbulence temporal attributes. *J. Turbulence 16*, 809–831.

Anderson, W. and C. Meneveau (2010). A large-eddy simulation model for boundary-layer flow over surfaces with horizontally resolved but vertically unresolved roughness elements. *Boundary-Layer Meteorol. 137*, 397–415.

Anderson, W. and C. Meneveau (2011). A dynamic large-eddy simulation model for boundary layer flow over multiscale, fractal-like surfaces. *J. Fluid Mech. 679*, 288–314.

Andreotti, B., P. Claudin, and S. Douady (2002). Selection of dune shapes and velocities part 1: Dynamics of sand, wind and barchans. *The European Physical Journal B-Condensed Matter and Complex Systems 28*(3), 321–339.

Bagnold, R. (1956). *The Physics of Blown Sand and Desert Dunes.* Chapman and Hall.

Bailey, B. N. and R. Stoll (2016). The creation and evolution of coherent structures in plant canopy flows and their role in turbulent transport. *Journal of Fluid Mechanics 789*, 425–460.

Best, J., R. Kostaschuk, and P. Villard (2001). Quantitative visualization of flow fields associated with alluvial sand dunes: results from the laboratory and field using ultrasonic and acoustic doppler anemometry. *Journal of Visualization 4*(4), 373–381.

Blois, G., K. Christensen, J. Best, G. Elliott, J. Austin, C. Dutton, M. Bragg, M. Garcia, and B. Fouke (2012). A versatile refractive-index-matched flow facility for studies of complex flow systems across scientific disciplines. *AIAA Paper*, doi: 10.2514/6.2012–736.

Bou-Zeid, E., C. Meneveau, and M. Parlange (2005). A scale-dependent lagrangian dynamic model for large eddy simulation of complex turbulent flows. *Phys. Fluids 17*, 025105.

Bourke, M., N. Lancaster, L. Fenton, E. Parteli, J. Zimbelman, and J. Radebaugh (2010). Extraterrestrial dunes: An introduction to the special issue on planetary dune systems. *Geomorphology 121*, 1–14.

Bradshaw, P. (1987). Turbulent secondary flows. *Ann. Rev. Fluid Mech. 19*, 53–74.

Bristow, N., G. Blois, J. L. Best, and K. Christensen (2018). Turbulent flow structure associated with collision between laterally offset, fixed-bed barchan dunes. *Journal of Geophysical Research: Earth Surface 123*(9), 2157–2188.

Bristow, N., G. Blois, J. L. Best, and K. Christensen (2019). Spatial scales of turbulent flow structures associated with interacting barchan dunes. *Journal of Geophysical Research: Earth Surface 124*(5), 1175–1200.

Bristow, N., C. Wang, G. Blois, J. Best, and K. Anderson, W.and Christensen (2017). Experimental measurements of turbulent flow structure associated with colliding barchan dunes. *Proc. 5th International Planetary Dunes Workshop, St.George, UT*.

Browand, F. and T. Troutt (1985). The turbulent mixing layer: geometry of large vortices. *J. Fluid Mech. 158*, 489–509.

Castro, I. (2007). Rough-wall boundary layers: mean flow universality. *J. Fluid Mech. 585*, 469–485.

Chauhan, K., J. Philip, and I. Marusic (2014). Scaling of the turbulent/non-turbulent interface in boundary layers. *Journal of Fluid Mechanics 751*, 298–328.

Christensen, K. and R. Adrian (2001). Statistical evidence of hairpin vortex packets in wall turbulence. *J. Fluid Mech. 431*, 433–443.

Cohen, L. (1989). Time-frequency distributions-a review. *Proceedings of the IEEE 77*(7), 941–981.

Durán, O., E. J. Parteli, and H. J. Herrmann (2010). A continuous model for sand dunes: Review, new developments and application to barchan dunes and barchan dune fields. *Earth Surface Processes and Landforms*.

Endo, N., K. Taniguchi, and A. Katsuki (2004). Observation of the whole process of interaction between barchans by flume experiments. *Geophysical Research Letters 31*(12).

Ewing, R. and G. Kocurek (2010a). Aeolian dune-field pattern boundary conditions. *Geomorphology 114*, 175–187.

Ewing, R. and G. Kocurek (2010b). Aeolian dune interactions and dune-field pattern formation: White Sands Dune Field, New Mexico. *Sedimentology 57*, 1199–1218.

Farge, M. (1992). Wavelet transforms and their applications to turbulence. *Annual review of fluid mechanics 24*(1), 395–458.

Fernandez-Luque, R. and R. van Beek (1976). Erosion and transport of bed-load sediment. *J. Hydraul. Res. 14*, 127–144.

Finnigan, J. (2000). Turbulence in plant canopies. *Ann. Rev. Fluid Mech. 32*, 519–571.

Finnigan, J., R. Shaw, and E. Patton (2009). Turbulence structure above a vegetation canopy. *J. Fluid Mech. 637*, 387–424.

Flack, K. and M. Schultz (2010). Review of hydraulic roughness scales in the fully rough regime. *ASME J. of Fluids Eng. 132*, 041203–1–10.

Frank, A. and G. Kocurek (1996). Airflow up the stoss slope of sand dunes: limitations of current understanding. *Geomorphology 17*, 47–54.

Funada, T. and D. Joseph (2001). Viscous potential flow analysis of kelvin–helmholtz instability in a channel. *Journal of Fluid Mechanics 445*, 263–283.

Germano, M. (1992). Turbulence: the filtering approach. *J. Fluid Mech. 238*, 325–336.

Germano, M., U. Piomelli, P. Moin, and W. Cabot (1991). A dynamic subgrid-scale eddy viscosity model. *Phys. Fluids A 3*, 1760–1765.

Ghisalberti, M. (2009). Obstructed shear flows: similarities across systems and scales. *J. Fluid Mech. 641*, 51.

Grass, A. (1971). Structural features of turbulent flow over smooth and rough boundaries. *J. Fluid Mech. 50*, 233–255.

Grotzinger, J., D. Sumner, L. Kah, K. Stack, S. Gupta, L. Edgar, D. Rubin, K. Lewis, J. Schieber, N. Mangold, R. Milliken, P. Conrad, D. DesMarais, J. Farmer, K. Siebach, F. Calef, J. Hurowitz, S. McLennan, D. Ming, D. Vaniman, J. Crisp, A. Vasavada, K. Edgett, M. Malin, D. Blake, R. Gellert, P. Mahaffy, R. Wiens, S. Maurice, J. Grant, S. Wilson, R. Anderson, L. Beegle, R. Arvidson, B. Hallet, R. Sletten, M. Rice, J. Bell, J. Griffes, B. Ehlmann, R. Anderson, T. Bristow, W. Dietrich, G. Dromart, J. Eigenbrode, A. Fraeman, C. Hardgrove, K. Herkenhoff, L. Jandura, G. Kocurek, S. Lee, L. Leshin, R. Leveille, D. Limonadi, J. Maki, S. McCloskey, M. Meyer, M. Minitti, H. Newsom, D. Oehler,

A. Okon, M. Palucis, T. Parker, S. Rowland, M. Schmidt, S. Squyres, A. Steele, E. Stolper, R. Summons, A. Treiman, R. Williams, and A. Yingst (2014). A habitable fluvio-lacustrine environment at Yellowknife Bay, Gale Crater, Mars. *Science 343*, 1242777–1–14.

Hayward, R., K. Mullins, L. Fenton, T. Hare, T. Titus, M. Bourke, A. Colaprete, and P. Christensen (2007). Mars global digital dune database and initial science results. *J. Geophys. Research 112*, doi:10.1029/2007JE002943.

Herrmann, H. J., J. S. A. Jr., V. Schatz, G. Sauermann, and E. J. R. Parteli (2005). Calculation of the separation streamlines of barchans and transverse dunes. *Physica A 357*, 44–49.

Hersen, P., K. Andersen, H. Elbelrhiti, B. Andreotti, P. Claudin, and S. Douady (2004). Corridors of barchan dunes: Stability and size selection. *Phys. Rev. E 69*, 011304.

Hersen, P. and S. Douady (2005). Collision of barchan dunes as a mechanism of size regulation. *Geophys. Res. Lett. 32*, doi:10.1029/2005GL024179.

Hutchins, N. and I. Marusic (2007). Evidence of very long meandering features in the logarithmic region of turbulent boundary layers. *J. Fluid Mech. 579*, 1–28.

Hutchins, N., J. Monty, B. Ganapathisubramani, H. Ng, and I. Marusic (2011). Three-dimensional conditional structure of a high-reynolds-number turbulent boundary layer. *J. Fluid Mech. 673*, 255–285.

Jackson, P. and J. Hunt (1975). Turbulent wind flow over a low hill. *Quarterly Journal of the Royal Meteorological Society 101*(430), 929–955.

Jacob, C. and W. Anderson (2016). Conditionally averaged large-scale motions in the neutral atmospheric boundary layer: insights for aeolian processes. *Boundary-Layer Meteorology*.

Jeong, J. and F. Hussain (1995). On the identification of a vortex. *J. Fluid Mech. 285*, 69–94.

Jerolmack, D. and D. Mohrig (2005). A unified model for subaqueous bed form dynamics. *Water Resour. Res. 41*, doi:10.1029/2005WR004329.

Jimenez, J. (2004). Turbulent flow over rough wall. *Annu. Rev. Fluid Mech. 36*, 173.

Khosronejad, A. and F. Sotiropoulos (2017). On the genesis and evolution of barchan dunes: morphodynamics. *Journal of Fluid Mechanics 815*, 117–148.

Kocurek, G., M. Carr, R. Ewing, K. Havholm, Y. Nagar, and A. Singhvi (2007). White sands dune field, New Mexico: Age, dune dynamics and recent accumulations. *Sedimentary Geology 197*, 313–331.

Kocurek, G. and R. Ewing (2005). Aeolian dune field self-organization – implications for the formation of simple versus complex dune-field patterns. *Geomorphology 72*, 94–105.

Kok, J., E. Parteli, T. Michaels, and D. Karam (2012). The physics of wind-blown sand and dust. *Reports on Progress in Physics 75*, 106901:1–72.

Lancaster, N. (1982). Dunes on the Skeleton Coast, SWA/Namibia: geomorphology and grain size relationships. *Earth Surface Proc. Landforms 7*, 575–587.

Lancaster, N. (1989a). The dynamics of star dunes: an example from the Gran Desierto, Mexico. *Sedimentology 36*, 273–289.

Lancaster, N. (1989b). The Namib Sand Sea: Dune forms, processes, and sediments. *A.A. Balkema, Rotterdam.*

Leonardi, S., P. Orlandi, R. Smalley, L. Djenidi, and R. Antonia (2003). Direct numerical simulations of turbulent channel flow with transverse square bars on one wall. *J. Fluid Mech. 491*, 229–238.

Livingstone, I., G. Wiggs, and C. Weaver (2006). Geomorphology of desert sand dunes: A review of recent progress. *Earth-Science Review 80*, 239–257.

Melton, F. A. (1940). A tentative classification of sand dunes its application to dune history in the southern high plains. *The Journal of Geology 48*(2), 113–174.

Meneveau, C. and J. Katz (2000). Scale-invariance and turbulence models for large-eddy simulation. *Annual Review of Fluid Mechanics 32*, 1–32.

Metias, O. (1964). Direct and large eddy simulations of coherent vortices in three dimensional turbulence. In J. Bonnet (Ed.), *Eddy structure identification*, pp. 334–364. Springer-Verlag, New York.

Meyer-Peter, E. and R. Müller (1948). Formulas for bed-load transport. *Proc. 2nd Meeting Inte. Assoc. Hydraulic Structures Res. (Int. Assoc. for Hydraul. Res., Madrid.)*, 39–64.

Mittal, R. and G. Iaccarino (2005). Immersed boundary methods. *Annual Rev. Fluid Mech. 37*, 239–261.

Müller, A. and A. Gyr (1986). On the vortex formation in the mixing layer behind dunes. *J. Hydraul. Res. 24*, 359–375.

Narteau, C., D. Zhang, O. Rozier, and P. Claudin (2009). Setting the length and time scales of a cellular automaton dune model from the analysis of superimposed bed forms. *Journal of Geophysical Research: Earth Surface 114*(F3).

Nelson, J. M., S. R. McLean, and S. R. Wolfe (1993). Mean flow and turbulence fields over two-dimensional bed forms. *Water Resources Research 29*(12), 3935–3953.

Nishimori, H. and N. Ouchi (1993). Formation of ripple patterns and dunes by wind-blown sand. *Physical Review Letters 71*(1), 197.

Omidyeganeh, M. and U. Piomelli (2011a). Large-eddy simulation of two-dimensional dunes in a steady, unidirectional flow. *Journal of Turbulence*.

Omidyeganeh, M. and U. Piomelli (2011b). Large-eddy simulation of two-dimensional dunes in a steady, unidirectional flow. *J. Turbulence 12*, 1–31.

Omidyeganeh, M. and U. Piomelli (2013a). Large-eddy simulation of three-dimensional dunes in a steady, unidirectional flow. part 1. turbulence statistics. *J. Fluid Mech. 721*, 454–483.

Omidyeganeh, M. and U. Piomelli (2013b). Large-eddy simulation of three-dimensional dunes in a steady, unidirectional flow. part 2. flow structures. *Journal of Fluid Mechanics 734*, 509–534.

Omidyeganeh, M., U. Piomelli, K. Christensen, and J. Best (2013). Large eddy simulation of interacting barchan dunes in a steady, unidirectional flow. *Journal of Geophysical Research: Earth Surface 118*(4), 2089–2104.

Ortiz, P. and P. K. Smolarkiewicz (2009). Coupling the dynamics of boundary layers and evolutionary dunes. *Physical Review E 79*, 041307.

Pähtz, T., J. F. Kok, and H. J. Herrmann (2012). The apparent roughness of a sand surface blown by wind from an analytical model of saltation. *New Journal of Physics 14*(4), 043035.

Palmer, J., R. Mejia-Alvarez, J. Best, and K. Christensen (2012a). Particle-image velocimetry measurements of flow over interacting barchan dunes. *Exp. Fluids 52*, 809–829.

Palmer, J. A., R. Mejia-Alvarez, J. L. Best, and K. T. Christensen (2012b). Particle-image velocimetry measurements of flow over interacting barchan dunes. *Experiments in fluids 52*(3), 809–829.

Pan, Y. and M. Chamecki (2016). A scaling law for the shear-production range of second-order structure functions. *Journal of Fluid Mechanics 801*, 459–474.

Parteli, E. J., O. Durán, M. C. Bourke, H. Tsoar, T. Pöschel, and H. Herrmann (2014). Origins of barchan dune asymmetry: Insights from numerical simulations. *Aeolian Research 12*, 121–133.

Parteli, E. J., O. Durán, H. Tsoar, V. Schwämmle, and H. J. Herrmann (2009). Dune formation under bimodal winds. *Proceedings of the National Academy of Sciences 106*(52), 22085–22089.

Parteli, E. J. R., V. Schwammle, H. J. Herrmann, L. H. U. Monteiro, and L. P. Maia (2006). Profile measurement and simulation of a transverse dune field in the Lençóis Maranhenses. *Geomorphology 81*, 29–42.

Pelletier, J. D. (2009). Controls on the height and spacing of eolian ripples and transverse dunes: A numerical modeling investigation. *Geomorphology 105*, 322–333.

Perkins, H. (1970). The formation of streamwise vorticity in turbulent flow. *Journal of Fluid Mechanics 44*(04), 721–740.

Piomelli, U. and E. Balaras (2002). Wall-layer models for large-eddy simulation. *Annu. Rev. Fluid Mech. 34*, 349–374.

Pope, S. (2000). *Turbulent flows*. Cambridge University Press.

Raupach, M., R. Antonia, and S. Rajagopalan (1991). Rough-wall turbulent boundary layers. *Appl. Mech. Rev. 44*, 1–25.

Raupach, M., J. Finnigan, and Y. Brunet (1996). Coherent eddies and turbulence in vegetation canopies: the mixing layer analogy. *Boundary-Layer Meteorol. 78*, 351–382.

Sauermann, G., J. Andrade Jr, L. Maia, U. Costa, A. Araújo, and H. Herrmann (2003). Wind velocity and sand transport on a barchan dune. *Geomorphology 54*(3-4), 245–255.

Shao, Y. (2008). *Physics and Modelling of Wind Erosion*. Springer Verlag.

Townsend, A. (1976). *The structure of turbulent shear flow*. Cambridge University Press, Cambridge, UK.

Tseng, Y.-H., C. Meneveau, and M. Parlange (2006). Modeling flow around bluff bodies and predicting urban dispersion using large-eddy simulation. *Environ. Sci. and Tech. 40*, 2653–2662.

Tsoar, H. (1983). Dynamic processes acting on a longitudinal (seif) dune. *Sedimentology 30*, 567–578.

Wang, C. and W. Anderson (2017). Numerical study of turbulent flow over stages of interacting barchan dunes: sediment scour and vorticity dynamics. *APS Meeting Abstracts*.

Wang, C. and W. Anderson (2018a). Large-eddy simulation of turbulent flow over spanwise-offset barchan dunes: interdune roller sustained by vortex stretching. *Bulletin of the American Physical Society 63*.

Wang, C. and W. Anderson (2018b). Large-eddy simulation of turbulent flow over spanwise-offset barchan dunes: Interdune vortex stretching drives asymmetric erosion. *Physical Review E 98*(3), 033112.

Wang, C. and W. Anderson (2019a). Turbulence coherence within canonical and realistic aeolian dune-field roughness sublayers. *Boundary-Layer Meteorology*.

Wang, C. and W. Anderson (2019b). Turbulence structure over idealized and natural barchan dune fields. *Bulletin of the American Physical Society*.

Wang, C., G. Bristow, N.and Blois, K. Christensen, and W. Anderson (2017). Large-eddy simulation & experimental research of proximal deformed barchan dunes. *Proc. 5th International Planetary Dunes Workshop, St.George, UT*.

Wang, C., Z. Tang, N. Bristow, G. Blois, K. Christensen, and W. Anderson (2016). Numerical and experimental study of flow over stages of an offset merger dune interaction. *Computers & Fluids*.

Wang, C., Z. Tang, N. Bristow, G. Blois, K. Christensen, and W. Anderson (2016, November). Numerical and experimental study of flow over stages of an offset merger dune interaction. In *APS Meeting Abstracts*.

Wu, Y. and K. T. Christensen (2010). Spatial structure of a turbulent boundary layer with irregular surface roughness. *J. Fluid Mech. 655*, 380–418.

Zhang, D., C. Narteau, and O. Rozier (2010). Morphodynamics of barchan and transverse dunes using a cellular automaton model. *Journal of Geophysical Research: Earth Surface 115*(F3).

Zhang, D., C. Narteau, O. Rozier, and S. C. Du Pont (2012). Morphology and dynamics of star dunes from numerical modelling. *Nature Geoscience 5*(7), 463.

Zhou, J., R. Adrian, and S. Balachandar (1996). Autogeneration of near-wall vortical structures in channel flow. *Phys. Fluids 8*, 288–290.

Zimbelman, J. (2010). Transverse aeolian ridges on Mars: First results from HiRISE images. *Geomorphology 121*, 22–29.

BIOGRAPHICAL SKETCH

Chao Wang was born in Xi'an, China. He completed his schoolwork in Xi'an Gaoxin No.1 High School and attended Nanjing University of Aeronautics and Astronautics in 2011 to pursue his bachelor's degree in aerospace and mechanical engineering. Upon getting his bachelor's degree in May 2015, he joined The University of Texas at Dallas to pursue his doctoral degree supported by Prof. William Anderson. After earning his master's degree in mechanical engineering in 2018, he continued his research at The University of Texas at Dallas to receive his doctorate degree in 2019.

CURRICULUM VITAE

Chao Wang

September 20, 2019

Contact Information:

Department of Mechanical Engineering
The University of Texas at Dallas
800 W. Campbell Rd.
Richardson, TX 75080-3021, U.S.A.

Email: `cxw151530@utdallas.edu`

Educational History:

B.S., Aerospace and Mechanical Engineering, Nanjing University of Aeronautics and Astronautics, 2015
M.S., Mechanical Engineering, The University of Texas at Dallas, 2018
Ph.D., Mechanical Engineering, The University of Texas at Dallas, 2019

Employment History:

Mechanical Engineer Intern, Jacobs Engineering Group, May 2019 – August 2019
Research Assistant, The University of Texas at Dallas, September 2015 – present
Teaching Assistant, The University of Texas at Dallas, September 2016 – present

Journal Publications:

Wang, Chao, et al. "Numerical and experimental study of flow over stages of an offset merger dune interaction." *Computers & Fluids, Invited Contribution to Special Edition on DNS/LES of Geophysical Flows doi.org/10.1016/j.compfluid.2016.11.005..*
Wang, Chao, & Anderson, William. "Large-eddy simulation of turbulent flow over spanwise-offset barchan dunes: Interdune vortex stretching drives asymmetric erosion." *Physical Review E 98.3 (2018): 033112.*
Wang, Chao, & Anderson, William. "Turbulence Coherence Within Canonical and Realistic Aeolian Dune-Field Roughness Sublayers." *Boundary-Layer Meteorology, 2019: 1-26.*

Professional Certificate:

Engineer In Training (EIT), 2018–present

Professional Membership:

American Physics Society (APS)
Lunar and Planetary Institude (LPI)

Professional Recognitions and Honors:

PhD Research Small Grants, Mechanical Engineering, UTD, 2018
Mechanical Engineering Department Fellowship, NUAA, 2013